

Mars Global Surveyor Thermal Emission Spectrometer experiment: Investigation description and surface science results

P. R. Christensen,¹ J. L. Bandfield,¹ V. E. Hamilton,¹ S. W. Ruff,¹ H. H. Kieffer,²
T. N. Titus,² M. C. Malin,³ R. V. Morris,⁴ M. D. Lane,⁴ R. L. Clark,⁵ B. M. Jakosky,⁶
M. T. Mellon,⁶ J. C. Pearl,⁷ B. J. Conrath,⁷ M. D. Smith,⁷ R. T. Clancy,⁸ R. O. Kuzmin,⁹
T. Roush,¹⁰ G. L. Mehall,¹ N. Gorelick,¹ K. Bender,¹ K. Murray,¹ S. Dason,⁷ E. Greene,⁷
S. Silverman,¹¹ and M. Greenfield¹¹

Abstract. The Thermal Emission Spectrometer (TES) investigation on Mars Global Surveyor (MGS) is aimed at determining (1) the composition of surface minerals, rocks, and ices; (2) the temperature and dynamics of the atmosphere; (3) the properties of the atmospheric aerosols and clouds; (4) the nature of the polar regions; and (5) the thermophysical properties of the surface materials. These objectives are met using an infrared (5.8- to 50- μm) interferometric spectrometer, along with broadband thermal (5.1- to 150- μm) and visible/near-IR (0.3- to 2.9- μm) radiometers. The MGS TES instrument weighs 14.47 kg, consumes 10.6 W when operating, and is $23.6 \times 35.5 \times 40.0$ cm in size. The TES data are calibrated to a $1\text{-}\sigma$ precision of $2.5^{-6} \times 10^{-8} \text{ W cm}^{-2} \text{ sr}^{-1}/\text{cm}^{-1}$, $1.6 \times 10^{-6} \text{ W cm}^{-2} \text{ sr}^{-1}$, and ~ 0.5 K in the spectrometer, visible/near-IR bolometer, and IR bolometer, respectively. These instrument subsections are calibrated to an absolute accuracy of $\sim 4 \times 10^{-8} \text{ W cm}^{-2} \text{ sr}^{-1}/\text{cm}^{-1}$ (0.5 K at 280 K), 1–2%, and $\sim 1\text{--}2$ K, respectively. Global mapping of surface mineralogy at a spatial resolution of 3 km has shown the following: (1) The mineralogic composition of dark regions varies from basaltic, primarily plagioclase feldspar and clinopyroxene, in the ancient, southern highlands to andesitic, dominated by plagioclase feldspar and volcanic glass, in the younger northern plains. (2) Aqueous mineralization has produced gray, crystalline hematite in limited regions under ambient or hydrothermal conditions; these deposits are interpreted to be in-place sedimentary rock formations and indicate that liquid water was stable near the surface for a long period of time. (3) There is no evidence for large-scale (tens of kilometers) occurrences of moderate-grained ($>50\text{-}\mu\text{m}$) carbonates exposed at the surface at a detection limit of $\sim 10\%$. (4) Unweathered volcanic minerals dominate the spectral properties of dark regions, and weathering products, such as clays, have not been observed anywhere above a detection limit of $\sim 10\%$; this lack of evidence for chemical weathering indicates a geologic history dominated by a cold, dry climate in which mechanical, rather than chemical, weathering was the significant form of erosion and sediment production. (5) There is no conclusive evidence for sulfate minerals at a detection limit of $\sim 15\%$. The polar region has been studied with the following major conclusions: (1) Condensed CO_2 has three distinct end-members, from fine-grained crystals to slab ice. (2) The growth and retreat of the polar caps observed by MGS is virtually the same as observed by Viking 12 Martian years ago. (3) Unique regions have been identified that appear to differ primarily in the grain size of CO_2 ; one south polar region appears to remain as black slab CO_2 ice throughout its sublimation. (4) Regional atmospheric dust is common in localized and regional dust storms around the margin and interior of the southern cap. Analysis of the thermophysical properties of the surface shows that (1) the spatial pattern of albedo has changed since Viking observations, (2) a unique cluster of surface materials with intermediate inertia and albedo occurs that is distinct from the previously identified low-inertia/bright and high-inertia/dark surfaces, and (3) localized patches of high-inertia material have been found in topographic lows and may have been formed by a unique set of aeolian, fluvial, or erosional processes or may be exposed bedrock.

¹Department of Geology, Arizona State University, Tempe, Arizona.

²U.S. Geological Survey, Flagstaff, Arizona.

³Malin Space Science Systems, San Diego, California.

⁴NASA Johnson Space Center, Houston, Texas.

⁵U.S. Geological Survey, Denver, Colorado.

⁶University of Colorado, Boulder, Colorado.

⁷Goddard Space Flight Center, Greenbelt, Maryland.

⁸Space Science Institute, Boulder, Colorado.

⁹Vernadsky Institute, Moscow, Russia.

¹⁰Ames Research Center, Moffett Field, California.

¹¹Raytheon Santa Barbara Remote Sensing, Goleta, California.

Copyright 2001 by the American Geophysical Union.

Paper number 2000JE001370.

0148-0227/01/2000JE001370\$09.00

1. Introduction

The Thermal Emission Spectrometer (TES) experiment is designed to address a wide range of science objectives, including the determination of surface mineralogy, volatile abundance and history, and atmospheric dynamics. The specific objectives of the TES experiment are (1) to determine and map the mineralogy of surface rocks, soils, and ices; (2) to study the composition, particle size, and spatial and temporal distribution of atmospheric dust; (3) to locate water-ice and CO₂ condensate clouds and determine their temperature, height, and condensate abundance; (4) to study the growth, retreat, and total energy balance of the annual polar caps; and (5) to measure the thermophysical properties of the Martian surface materials [Christensen *et al.*, 1992].

These objectives are addressed using thermal infrared spectral observations between 5.8 and 50 μm (1709–200 cm^{-1}), along with bolometric thermal radiance (5.1–150 μm) and visible/near-infrared solar reflectance (0.3–2.9 μm) measurements. The spectral range, spectral sampling (~ 5 and 10 cm^{-1}), radiometric resolution (signal-to-noise ratio >400 at 1000 cm^{-1} and 270 K), and spatial resolution (3 km) provide high-quality midinfrared spectra at sufficient ground resolution to isolate and study small-scale geologic features such as channels, sedimentary deposits, volcanic centers and flows, crater walls and ejecta, and aeolian deposits.

The TES instrument follows a progression of infrared radiometers and spectrometers carried to Mars. Mariner 6, 7, and 9 all carried thermal IR spectrometers [Hanel *et al.*, 1972a, 1972b; Conrath *et al.*, 1973; Pimentel *et al.*, 1974] that provided pioneering information on the composition and properties of the Martian surface and atmosphere. Mariner 6, 7, and 9 also carried infrared radiometer (IRR) instruments [Kieffer *et al.*, 1973; Neugebauer *et al.*, 1971]. These instruments had two broadband thermal channels and addressed the physical, rather than compositional, properties of the surface. The Mariner 9 infrared interferometer spectrometer (IRIS) instrument provided high spectral resolution infrared observations of Mars with a spectral resolution of 2.5 cm^{-1} (apodized) [Hanel *et al.*, 1972b]. However, the IRIS investigation was designed primarily for atmospheric study, and most of the observations were made during an extensive dust storm. In addition, all observations had a spatial resolution of more than 125 km. As a result, most analyses have emphasized properties associated with the composition, thermal structure, and dynamics of atmospheric gases and aerosols [Conrath *et al.*, 1973; Conrath, 1975; Hanel *et al.*, 1972a; Toon *et al.*, 1977].

The Viking infrared thermal mapper (IRTM) also investigated the thermal infrared properties of the Martian surface but emphasized spatial resolution and coverage at the expense of spectral resolution. This instrument acquired broadband spectral data centered at 7, 9, 11, 15, and 20 μm with a spatial resolution of typically >30 km [Chase *et al.*, 1978; Kieffer *et al.*, 1977]. Its primary objective was to measure the thermophysical properties of the Martian surface, along with measurements of atmospheric temperature and aerosol properties [Kieffer *et al.*, 1977; Martin *et al.*, 1979; Martin, 1986].

The TES instrument, developed by the Raytheon Santa Barbara Remote Sensing (SBRS) and Arizona State University (ASU), is a Michelson interferometer inspired by the pioneering work of R. A. Hanel and colleagues in a series of missions from Nimbus III in 1969 [Hanel *et al.*, 1970] through Voyager in 1977 [Hanel *et al.*, 1980]. By using advances in uncooled

infrared detectors and space-qualified digital signal processors, the TES instrument combines high spectral resolution and broad spectral coverage, together with high spatial resolution and complete global coverage.

The TES instrument was originally selected in April 1986 for the Mars Observer (MO) mission with an original scheduled launch date of August 1990 [Christensen *et al.*, 1992]. The MO TES instrument was built by Hughes Santa Barbara Research Center (now Raytheon Santa Barbara Remote Sensing (SBRS)) and delivered to the MO spacecraft in October 1991. The MO mission was launched on August 25, 1992, but unfortunately failed on August 21, 1993, 3 days prior to Mars orbit insertion. The follow-on Mars Global Surveyor (MGS) TES instrument was built by SBRC beginning in October 1994 and delivered to the spacecraft in May 1996. The MGS spacecraft was launched on November 7, 1996, arrived at Mars on August 11, 1997, collected aerobraking and preliminary science data between August 15, 1997, and October 29, 1998, and began mapping on April 2, 1999 [Albee *et al.*, this issue]. Originally slated for a full Martian year of mapping observations, NASA now plans to operate the MGS spacecraft and all of its instruments for as long as possible.

In this paper we present a description of the as-built instrument, calibration methods and knowledge, radiometric performance, including noise and drift, and TES standard data products. We also describe the basic instrument operational strategy, data-processing methodology, and data archive plans and data structures for archiving the data through the Planetary Data System (PDS). Finally, a summary description of the major surface-related science results to date is included. Note that the major atmospheric results are presented in a companion paper by Smith *et al.* [this issue].

2. Instrument Design

2.1. Instrument Overview

The design of the TES is intentionally conservative. The primary instrument requirement was to obtain spectra with sufficient resolution and radiometric precision to allow materials of different mineralogy to be characterized and distinguished and to allow determination of relative abundances in mineral mixtures. In addition, it was necessary to have sufficient spectral resolution to allow the quantitative retrieval of atmospheric temperature versus pressure and to derive atmospheric dust, water vapor, and cloud abundance.

The TES instrument uses a Michelson interferometer mechanism and separate thermal bolometric and visible/near-IR reflectance channels. A major design feature is the use of uncooled detectors, which substantially reduce the complexity of the fabrication, testing, and spacecraft interface of the instrument. Although uncooled thermal detectors have lower responsivity than cooled quantum detectors, they have a major advantage because they are sensitive over the full (3–100 μm) IR spectrum, whereas available quantum detectors are not sensitive at wavelengths greater than ~ 15 μm . The measured performance (Table 1) is a factor of 4 higher signal-to-noise ratio (SNR) and a factor of 40 improvement in spatial resolution over the Mariner 9 IRIS, while maintaining sufficient spectral sampling (5 and 10 cm^{-1}) to observe the diagnostic spectral features in solid materials.

The MGS TES instrument is shown in Plate 1 and Figure 1. All elements of the TES are contained in a single unit consisting of the pointing mirror, telescopes, interferometer, calibra-

Table 1. As-Built Instrument Parameters for the Thermal Emission Spectrometer^a

Description	Value
Spectral range	
Interferometer	201.6–1708.9 cm ⁻¹ (~6–50 μm)
Radiometer	5.1–150 μm and 0.3–2.9 μm
Spectral sampling of interferometer	10 and 5 cm ⁻¹
Optical field of view size (FWHM)	
Visible/near-IR bolometer	8.0–8.9 mrad
Thermal bolometer	7.6–9.2 mrad
Spectrometer	7.4–8.3 mrad
Telescope aperture	
Interferometer	15.2-cm-diameter Cassegrain
Radiometer	1.5-cm-diameter off-axis reflecting
Pointing mirror	
Range	90° forward, 90° aft
Step size	~0.25 mrad
Detectors	uncooled deuterated triglycine sulfate (DTGS) pyroelectric
Spectrometer channel	six-element array, each 1.75 mm diameter NEN = ~6 × 10 ⁻⁸ W cm ⁻² sr ⁻¹ cm ⁻¹ at 250 cm ⁻¹ ~2.5 × 10 ⁻⁸ W cm ⁻² sr ⁻¹ cm ⁻¹ from ~300 to 1400 cm ⁻¹ ~4 × 10 ⁻⁸ W cm ⁻² sr ⁻¹ cm ⁻¹ at 1650 cm ⁻¹
Visible/near-IR bolometer	six-element array, each 1 × 1 mm NEN = ~3.75 × 10 ⁻⁶ W cm ⁻² sr ⁻¹ μm ⁻¹
Thermal bolometer	six-element array, each 1 × 1 mm NEAT = <0.1 K
Michelson mirror travel	+0.25 and +0.50 mm
Mirror velocity	0.0295 cm s ⁻¹
Neon fringe reference wavelength	703.2 nm
Sample rate	839 samples s ⁻¹ detector ⁻¹
Cycle time per measurement	1.8 s plus 0.2 s retrace (10 cm ⁻¹); 3.6 s plus 0.4 s retrace (5 cm ⁻¹)
Samples per interferogram	1344
Bits per sample	16
Spectral samples	143 (10 cm ⁻¹); 286 (5 cm ⁻¹)
Bits per spectral sample	12
Spacecraft data bit rates	1664, 2485, 4992 bit s ⁻¹
Size	23.6 × 35.5 × 40.0 cm
Mass	14.47 kg
Orbital average power	10.6 W

^aFWHM, full width at half maximum; NEN, noise equivalent radiance; NEAT, noise equivalent Delta temperature.

tion, and electronic processing subsystems. A block diagram showing all functional elements of the instrument is shown in Figure 2. The TES spectrometer and broadband radiometers have separate telescopes but share a common pointing mirror. This mirror is capable of rotating 360°, providing views to space, both limbs, and to internal, full-aperture thermal and visible/near-IR calibration targets. The spectrometer telescope is a 15.2-cm-diameter reflecting afocal design which feeds a flat-plate Michelson interferometer spectrometer with a beam diameter of 1.5 cm. The telescope used for the two bolometric channels is a 1.5-cm-diameter off-axis paraboloidal design, bore sighted with the spectrometer telescope. This telescope views the pointing mirror through an off-axis hole in the spectrometer primary mirror. Energy from the bolometer telescope is chopped at 30 Hz by a resonant fork chopper which produces an AC output from the detectors in the visible/near-IR reflectance and thermal bolometer channels. The outputs of all bolometric channels are synchronously demodulated.

All three sensors use 3 × 2 arrays of deuterated triglycine sulfate (DTGS) pyroelectric detectors to provide simultaneous spatial coverage of the Martian surface in all bands. These array packages are hermetically sealed and backfilled with dry nitrogen, allowing the TES to be operated in vacuum or in ambient conditions. The instantaneous field of view (IFOV) of each detector is ~8.3 mrad square (see Appendix B; section 2),

giving an IFOV of 3.15 km at nadir from the nominal orbital altitude of 378 km. The instrument cycle time for 10 cm⁻¹ operation is 1.8 s for the collection of the interferogram plus 0.2 s for the mirror flyback and electronic reset. These times are doubled (4 s total) for 5 cm⁻¹ operation.

The output from of the interferometer receives the following processing within the instrument before transfer to the PDS: (1) fast Fourier transformation (FFT) of data from all six interferometer channels; (2) correction for gain and offsets; (3) data editing and aggregation; (4) data compression; and (5) formatting for the PDS.

2.2. Interferometer

The interferometer telescope is a reflecting Cassegrain configuration with a focal ratio of $f/4$ and an intermediate field stop which limits stray light from being admitted to the interferometer and aft optics sections of the optical system. The afocal output beam of the telescope is 1.524 cm in diameter. After passing through the Michelson interferometer, the energy is focused by an off-axis mirror onto a 3 × 2 array of field stops. The focal ratio at the field stops is also $f/4$. Behind each stop is a field lens, operating at approximately $f/1$, and a pyroelectric detector. Each IFOV is defined by a field stop placed at the entrance of a field lens/detector package. The final focal ratio at each detector is $f/0.5$, providing sufficient

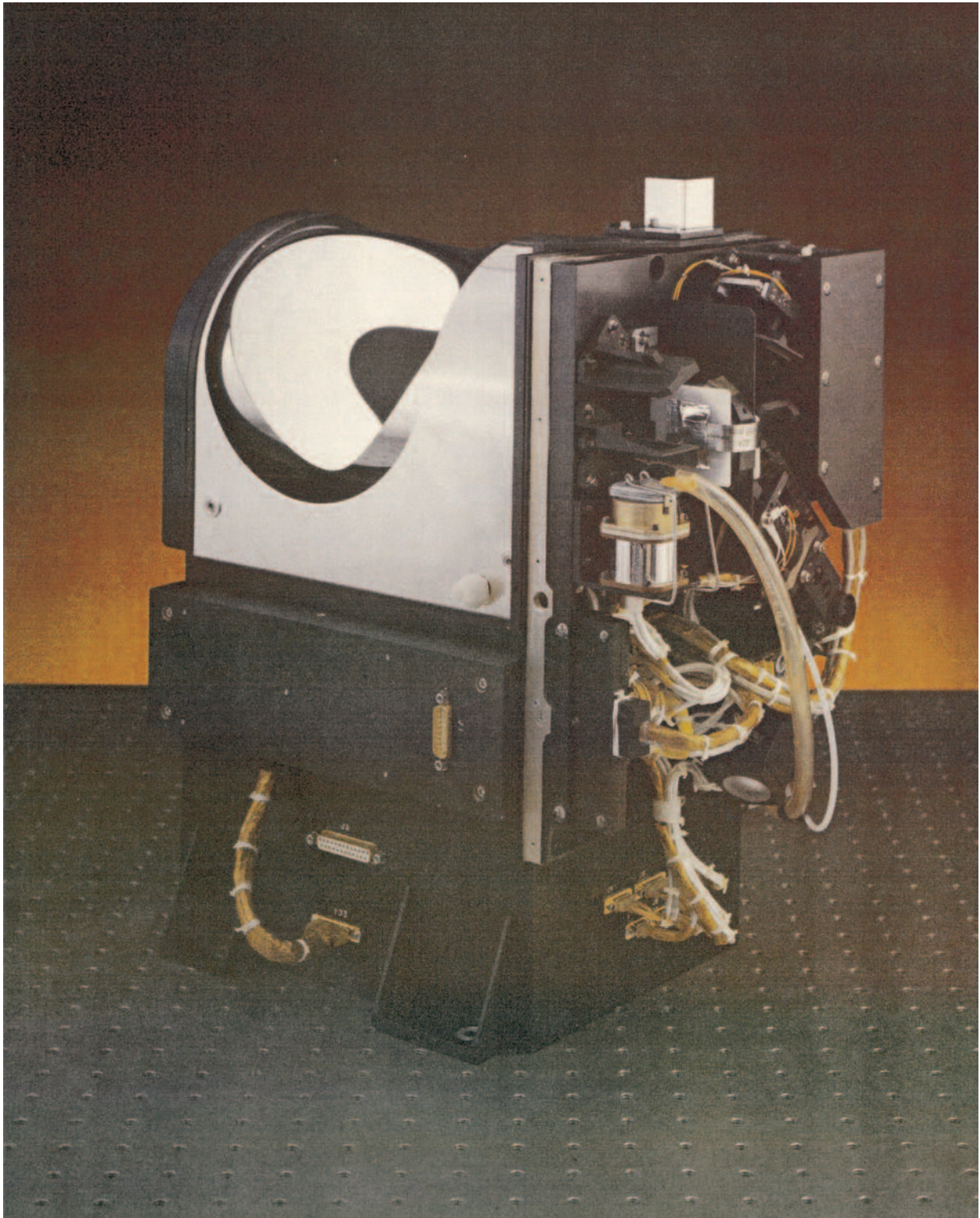


Plate 1. Mars Global Surveyor (MGS) Thermal Emission Spectrometer (TES) instrument with the electronics cover removed. Nadir view direction is toward the top. The alignment cube on top of the instrument was removed before launch.

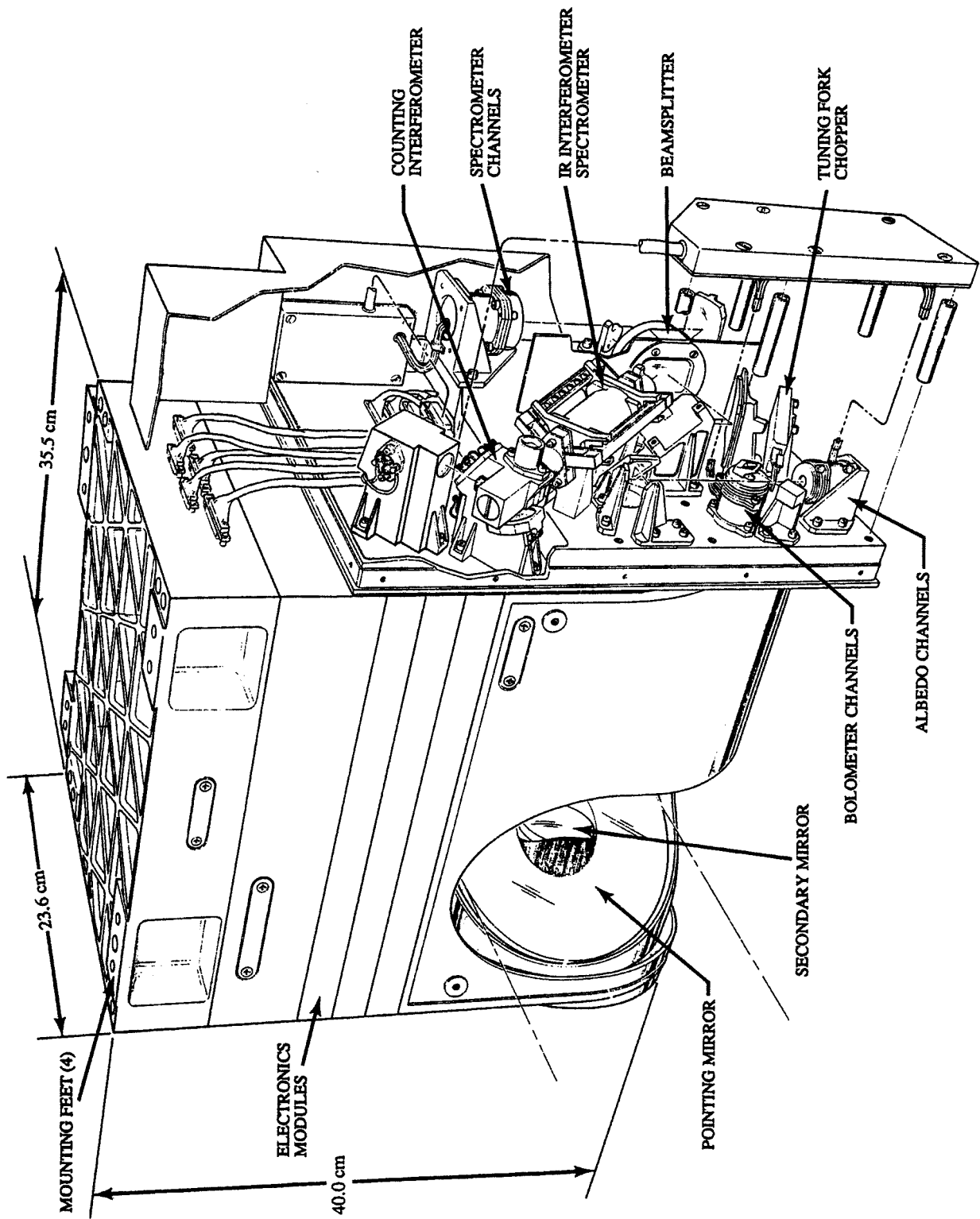


Figure 1. TES instrument drawing. Major components are indicated. Nadir direction is toward the bottom.

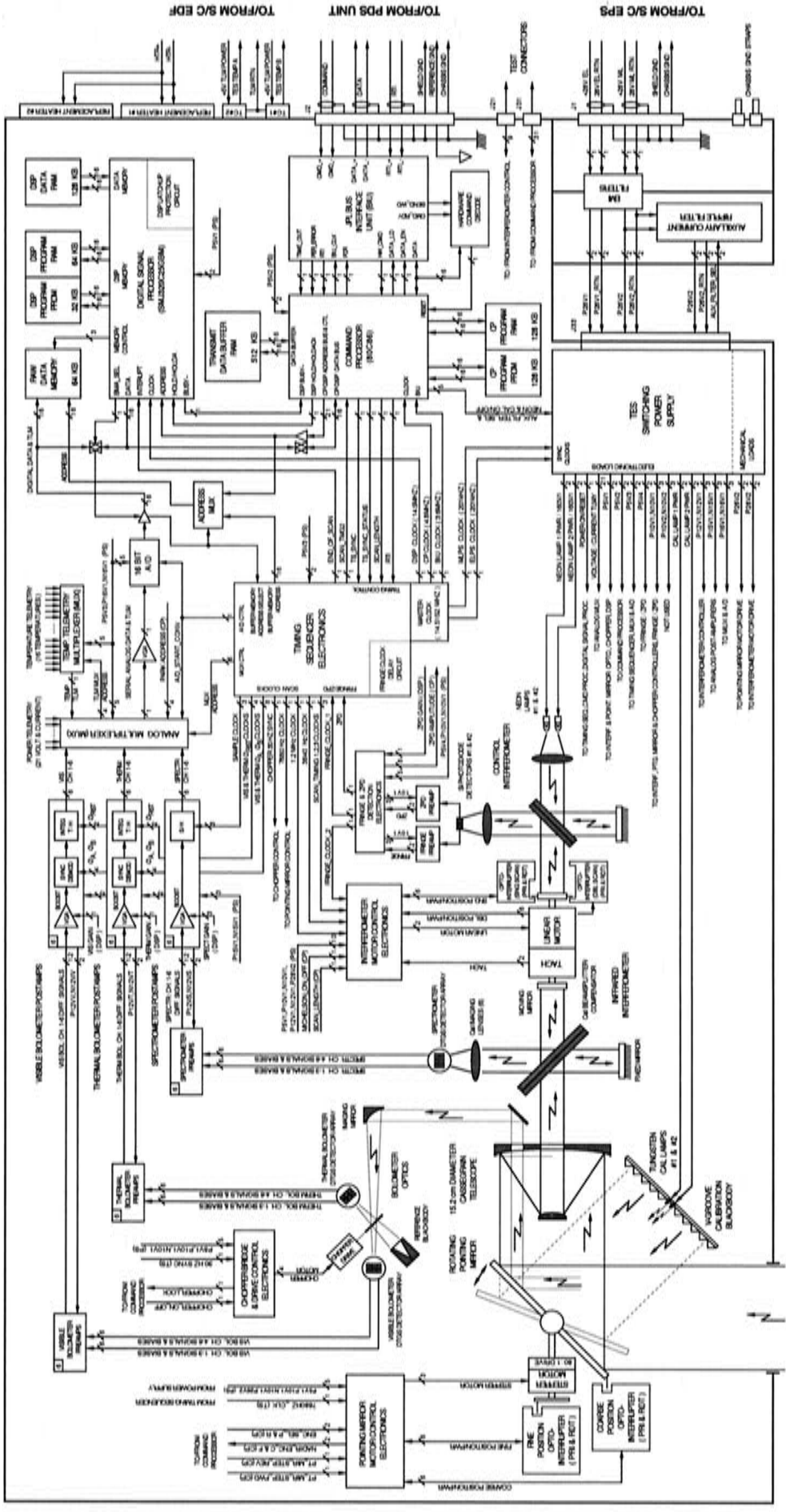


Figure 2. TES functional block diagram.

space between the detectors at the focal plane to mount individual detector and input field effect transistors (FETs).

The TES includes a flexure-mounted linear motor drive with a Michelson system at each end. An identical system was built and tested as part of the TES engineering model. The infrared spectrometer uses a plane mirror at the end of the motor drive, operated with a selectable travel distance, in order to produce double-sided interferograms at nominal spectral sampling of 5 and 10 cm^{-1} . Coated cesium iodide is used for the spectrometer beam splitter.

The visible interferometer is used to generate fringes that are used to control the linear drive servo and to determine position in the interferogram. This system uses a corner-cube mirror at the opposite end of the linear motor drive. The visible interferometer uses two redundant neon lamps as a source. A narrow band-pass filter is used to isolate the emission line at 703.2 nm for fringe generation, and the continuum is used as a quasi-white-light source for determination of zero path difference. A silicon photodiode detector is used for each of these functions.

None of the six detectors is centered on the optical axis of the interferometer. This positioning results in self-apodization and a spectral shift that is a function of both distance from the axis and optical frequency. Nominal 10 cm^{-1} operation (optical path difference of 0.05 cm) results in a full width at half maximum (FWHM) of 12.14 cm^{-1} (Appendix B). For the corner detectors and at the highest frequency (shortest wavelength) there is a significant departure from the ideal, with a worst case degradation to a FWHM of 16 cm^{-1} . Because the self-apodization is considerable, no further apodization is applied. Separate FFT algorithms are used for the center and edge detectors in order to partially correct for the different spectral shifts introduced into these detectors (Appendix B).

2.3. Thermal and Visible/Near-IR Radiometers

A separate 1.5-cm-diameter reflecting telescope, collimated with the main telescope and using the same pointing mirror, is used for the thermal and visible/near-IR radiometer channels. These channels have similar 3×2 arrays of detectors that are bore sighted with the spectrometer array. The optical system consists of a single off-axis paraboloidal mirror operating at $f/8$. A reflecting resonant fork chopper, operating at 30 Hz, is used to separate the visible/near-IR reflectance and thermal emission bands.

2.4. Electrical Design

A functional block diagram of the TES is shown in Figure 2. The TES electronics are composed of five electronic module subassemblies that form the main TES electronics module assembly, four small preamplifier subassemblies that connect to the TES detector assemblies, and an external power supply current ripple filter module. Each of the electronics module subassemblies contains one or two double-sided circuit card assemblies (CCAs). Each CCA includes two multilayered (4–8 signal and ground layers) printed wiring boards (PWBs) that are bonded back to back. These CCAs are populated with space-qualified analog and digital electronic components and then attached to the interior of each module's housing. The electronic module subassemblies include the following CCA modules: (1) Visible and Thermal Bolometer Postamplifier, (2) Spectrometer Postamplifier and Multiplexer/Analog to Digital Conversion/Fringe and ZPD Postamplifiers, (3) Timing Sequencer CCA and Digital Signal Processor, (4) Command

and Control Processor CCA and Memory CCA, and (5) Servo Control CCA and Power Supply CCA. The five electronic module subassemblies are interconnected via miniature-D connections and are stacked together to form the integrated TES electronics module assembly. The TES electronics communicates with the spacecraft via the Jet Propulsion Laboratory (JPL)-supplied Bus Interface Unit (BIU) that is integrated into the TES electronics module. A detailed discussion of the electronics design is provided in Appendix A.

2.5. Software

2.5.1. Overview. All data processing within the TES is under software control. The TES can downlink raw interferograms or raw spectra as well as spatially and/or spectrally averaged spectra. During the initial characterization period, full spectra were transmitted, with correspondingly lower spatial coverage. As knowledge of the Martian surface spectra has improved, spectral averaging has been increased, with a corresponding increase in spatial coverage.

In order to minimize the complexity of developing and managing software for the TES, a mature (in 1989) 80C86 processor design was used, with a dedicated TMS 32020 digital signal processor for the FFT. These processors allow the Fourier transform and spectral editing to be done within the instrument, which significantly reduces the volume of raw data that must be returned to Earth. The MGS mission does not experience severe radiation environments, and radiation-hardened parts were not required. ROM is used for code and constants affecting the safety of the instrument.

The TES flight processors performs the following functions: (1) command interpretation, (2) data collection, (3) Fourier transform, (4) spectral selection or averaging, (5) spatial selection and/or averaging, (6) lossless data compression, and (7) data formatting and packetization. A lossless ("Rice") data compression scheme developed by NASA [Rice, 1979] is used in the TES flight software. The spectra are preprocessed by normalizing each spectrum in a set of six acquired simultaneously and differencing five of the spectra from the sixth. This reference spectrum is transmitted along with the compressed differences. Data compression of ~ 1.7 has been achieved with this technique.

2.5.2. Data structures. The voltage output from the interferometer varies over $\pm 5\text{ V}$ and is digitized at 16-bit resolution. These data are processed on board the TES instrument using an integer, prime factors discrete Fourier transform (DFT). As a result of the cosine transforms applied to these data, the spectral data are real numbers representing the signal amplitude as a function of frequency (wave number). The spectral data from each detector are stored and transmitted in a fixed point format that consists of a single exponent for all spectral bands, together with a sign bit and 11 data bits, with an assumed decimal point in front of the first data bit, for each spectral band.

The visible/near-IR and thermal bolometer data are stored as signed 14-bit integers in 2's complement format. A maximum octal value of $0 \times 1\text{FFF}$ corresponds to $+5.0\text{ V}$ output from the visible/near-IR detector; a minimum value of 0×0 corresponds to -5.0 V .

2.6. Calibration

2.6.1. Prelaunch calibration overview. The TES instrument was calibrated and tested at SBRS prior to shipment to the spacecraft at Lockheed Martin Astronautics (LMA). The

primary objectives of these tests were to determine (1) the field-of-view definition and coalignment of all three instrument subsections; (2) the out-of-field response for all three instrument subsections; (3) the spectrometer spectral line shape and spectral sample position; (4) the visible/near-IR and thermal bolometer relative spectral response; and (5) the spectrometer, visible/near-IR bolometer, and thermal bolometer radiometric calibration. In addition to these calibrations, an extensive set of tests was performed under ambient and vacuum conditions to verify the instrument functional performance, including all actuators, the command and signal processors, and the command and data links. A detailed discussion of the calibration tests and results is given by *Christensen* [1999] and is summarized in Appendix B.

2.6.2. In-flight calibration overview. The TES instrument is calibrated in flight using periodic views of space and the internal calibration targets. The basic algorithms for these calibrations are described in the following sections.

2.6.2.1. Spectrometer: For each planet observation the TES acquires an interferogram signal, measured in voltage, that is transformed to a signal as a function of frequency. This signal is given at each wave number (ν , subscripts omitted) by

$$V_p = (R_p - R_i) f,$$

where V_p is the Fourier-transformed voltage signal generated by the TES looking at the planet, R_p is the radiance of the planet ($\text{W cm}^{-2} \text{sr}^{-1}/\text{cm}^{-1}$), R_i is the radiance of the instrument, and f is the instrument response function ($\text{V/W cm}^{-2} \text{sr}^{-1}/\text{cm}^{-1}$). Solving for the radiance of the planet gives

$$R_p = \frac{V_p}{f} + R_i.$$

The instrument radiance and the response function are determined routinely using observations of space and the internal reference surface (Appendix B). This determination requires space (S) and reference surface (R) observations acquired consecutively ("SR pairs"). The response function is slowly varying except for small variations due to changes in instrument temperature (Appendix B), whereas R_i can vary continuously throughout the orbit. Thus SR pairs are acquired only several times per orbit to determine the response function, whereas space observations are acquired approximately every 3–5 min to determine R_i .

The objectives of the in-flight calibration are (1) to develop an effective means for interpolating the instrument response function and instrument radiance between calibration observations and (2) to minimize the noise on these functions by taking advantage of their repetitive and predictable forms. At present, the response function for each planet observation is determined using a linear interpolation between the response functions for bounding SR pairs. However, the noise in the response function from a single SR pair can be reduced by combining multiple determinations over a period of time, taking into account the changes due to variations in instrument temperature. At the end of the mission the data will be recalibrated using a low-noise response function determined by fitting a function to the complete set of instrument response data over long (~30-day) periods. The effect will be to reduce the noise level by ~25%.

Once the instrument radiance is determined at each space observation, it is interpolated over time for all of the intervening planet observations and used with the response function to

determine the calibrated radiance for each planet observation. At present, a linear interpolation between bounding space values is used; with time in orbit, a more complex function will be determined to account for repetitive, periodic variations in instrument temperature.

2.6.2.2. Visible/near-infrared bolometer: The visible/near-infrared bolometer is calibrated using periodic observations of the internal calibration lamps and space (Appendix B) [*Christensen*, 1999]. Lamp observations are acquired once daily and once weekly for the primary and redundant lamps, respectively. These data are corrected for lamp and instrument temperature (Appendix B). For each planet observation the detector response is corrected for variations with temperature and the measured bolometer signal (voltage) is converted to integrated calibrated radiance ($\text{W cm}^{-2} \text{sr}^{-1}$).

The Lambert albedo A_L is computed using the calibrated radiance R , the Sun-Mars distance D , the incidence angle i , and the solar radiance integrated over the TES bolometer spectral response (S) [*Christensen*, 1999] using

$$A_L = \frac{RD^2}{S \cos(i)}.$$

2.6.2.3. Thermal bolometer: The thermal bolometer calibrated radiance is determined in an identical manner to the spectrometer radiance, but using the integrated planet and reference surface radiance that is determined using the measured bolometer spectral response (Appendix B) [*Christensen*, 1999]. The weighted integrated radiance as a function of scene temperature is computed by convolving the relative spectral response with the blackbody radiance. A lookup table is used to convert integrated radiance to brightness temperature.

2.7. In-Flight Radiance Precision and Accuracy

2.7.1. Spectrometer. The $1\text{-}\sigma$ radiance noise level of an individual spectral sample in a single TES spectrum has been determined using both prelaunch and in-flight observations to be $\sim 2.5 \times 10^{-8} \text{ W cm}^{-2} \text{sr}^{-1} \text{cm}^{-1}$ for the central wave numbers from ~ 300 to 1400 cm^{-1} , increasing to $\sim 6 \times 10^{-8}$ and $\sim 4 \times 10^{-8} \text{ W cm}^{-2} \text{sr}^{-1} \text{cm}^{-1}$ at shorter (250 cm^{-1}) and longer (1650 cm^{-1}) wave numbers, respectively (Appendix B) [*Christensen*, 1999]. Systematic errors in radiance can occur owing to the calibration process, where noise in the space and reference observations maps into the calibrated planet spectra as a function of the instrument temperature and the temperature difference between the scene and the instrument. This noise is reduced by acquiring and averaging three consecutive observations of both space and the reference surface.

The instrument temperature has varied from 275 to 290 K over the course of the mission, and the surface temperatures of the spectra generally used for compositional analyses are $>275 \text{ K}$. For this combination of temperatures the resulting systematic calibration error is $\sim 1 \times 10^{-8} \text{ W cm}^{-2} \text{sr}^{-1} \text{cm}^{-1}$ between 300 and 1400 cm^{-1} . The spectra presented in this paper are averages of at least six individual spectra, resulting in a total error due to the combined random and systematic errors of $\sim 1.2 \times 10^{-8} \text{ W cm}^{-2} \text{sr}^{-1} \text{cm}^{-1}$ between 300 and 1400 cm^{-1} .

The radiance errors can be converted to emissivity errors, which vary with wave number owing to the variation in blackbody radiance with temperature and wave number. For a surface temperature of 280 K and an average of six spectra, the total emissivity error from random and systematic sources is <0.0013 from 300 to 1100 cm^{-1} , increasing to 0.0035 at 1400 cm^{-1} .

The absolute accuracy of the TES spectra was determined prelaunch to be $\sim 4 \times 10^{-8} \text{ W cm}^{-2} \text{ sr}^{-1} \text{ cm}^{-1}$ from ~ 300 to 1400 cm^{-1} [Christensen, 1999]. This error corresponds to an absolute temperature error of $\sim 0.4 \text{ K}$ for a surface temperature of 280 K and $\sim 1.5 \text{ K}$ for a surface at 150 K . This temperature error is mapped into a smoothly varying offset in the emissivity spectrum that varies from 0.001 at 400 cm^{-1} to a maximum of 0.004 at 920 cm^{-1} to essentially 0 at 1300 cm^{-1} . This subtle curvature has a negligible effect on the derived surface composition.

A second systematic accuracy error is present owing to a minor misalignment of the optical axis with the rotational axis of the pointing mirror and secondary mirror assembly [Christensen et al., 1992]. As a result, the fraction of the instrument viewed when observing space, the reference surface, and the planet varies slightly, and the instrument energy is not perfectly removed by the calibration process. The consequence is a background radiance error of $\sim 1.0 \times 10^{-8} \text{ W cm}^{-2} \text{ sr}^{-1} \text{ cm}^{-1}$ between ~ 300 and 1400 cm^{-1} (Plate 2).

2.7.2. Visible/near-IR bolometer. The $1\text{-}\sigma$ precision of the calibrated radiance measurements was determined using observations of deep space acquired away from Mars during spacecraft rolls prior to and after periapsis. The internal lamp was not used because its temperature increases when left on for an extended period of time, which results in a change in its output level. The derived $1\text{-}\sigma$ variation in the zero-level radiance is $\sim 3.75 \times 10^{-6} \text{ W cm}^{-2} \text{ sr}^{-1}$ for all six detectors. This value is similar to the variation in the internal lamp brightness measured preflight ($1.6 \times 10^{-6} \text{ W cm}^{-2} \text{ sr}^{-1}$). A Lambertian surface reflecting all light (reflectivity of 1.0) would have a radiance of $8.718 \times 10^{-3} \text{ W cm}^{-2} \text{ sr}^{-1}$ at the Mars-Sun distance of these observations, measured at normal incidence angle. The $1\text{-}\sigma$ precision of the visible bolometer calibrated radiance corresponds to a noise-equivalent delta reflectivity (NE Δ R) of 0.00043 and is equivalent to an SNR of 2300 for a surface with unit reflectivity.

The absolute accuracy can be estimated by comparing the measured bolometer signal with the preflight measurements as a function of lamp and detector temperature. This comparison indicates a slight increase in the measured signal from the preflight data, specifically, a $<3\%$ increase in the measured signal for detector temperatures of $\sim 10^{\circ}\text{--}15^{\circ}\text{C}$ and an increase of $\sim 3\text{--}6\%$ near 0°C relative to the preflight measurements. This change can be due to a combination of (1) a change in the alignment of the lamp relative to the detectors; (2) an increase in lamp 1 brightness; (3) a change in the chopper alignment or timing; and (4) an increase in detector response [Christensen, 1999].

The change in lamp 1 relative to lamp 2, averaged for all detectors, is $\sim 0.7\%$ and is essentially constant with temperature. On the basis of experience at SBRS on the Galileo PPR instrument, the stability of these lamps is estimated to be $\pm 0.5\%$ on a long-term (years) basis and $\pm 0.15\%$ on a short-term (hours) basis. The ratio of the two TES lamps is consistent with these stability values. Because both lamps would need to have increased equally in brightness to account for changes in the lamp signal levels, it is concluded that the changes in measured signal are not due to changes in lamp output.

It is more likely either that the detector response with temperature has varied in flight, which would account for both the variations between detectors and the relatively large changes over temperature, or that the chopper alignment or timing has changed slightly. Neither of these cases will affect the absolute

calibration because the detector views both Mars and the lamps with the same chopper and detector characteristics. It is concluded that the absolute calibration is $\sim 1\text{--}2\%$ relative to the preflight calibration of the internal lamps.

3. Mission Operations

3.1. General Operations

The science objectives of the TES experiment are being addressed during the Mars Global Surveyor mission using a variety of observation types. These include (1) nadir pointing observations of the surface and atmosphere collected along the spacecraft ground track; (2) surface mosaics constructed by observing a particular region forward, nadir, and then aft along the ground track; (3) limb observations produced by scanning the pointing mirror across the limb, from atmosphere top to ground; (4) emission phase functions (EPFs) produced by viewing a particular region at a limited set of emission angles fore and aft; and (5) limb and surface observations utilizing spacecraft slews for off-ground track coverage (for instance, coverage of the geographic poles).

3.1.1. Instrument commanding. TES observations are controlled by manipulating instrument parameters and processor activities using an internal command language and control tables to select among the possible operational modes. Observation sequences command the basic instrument parameters, including detector mask, spectral mask, scan length, gain, telemetry packet length, and pointing mirror angle for each observation. The observations use a sequential numbering scheme composed of "ICKs" (Incremental Counter Keeper). This counter is based on the 2-s data collection "heartbeat" of the TES interferometer and begins at zero at the nightside equator crossing. Sequences may contain multiple related pointing mirror angles (for example, a complete limb set), or they may contain internal loops to repeat an observation one or more times. Orbital schedules contain lists of observational sequences, each tied to a specified time following the descending equator crossing event which controls timing within the TES instrument. At each descending equator crossing, TES receives an indication from the PDS and resets the internal counter to zero and prepares for the next set of observational sequences. The equator crossing command consists of two spacecraft clock times (SCLKs): the upcoming crossing and the one following. By providing two consecutive times, TES is able to autonomously calculate an orbital period and can project that period forward in time, generating new equator crossing times as needed.

3.1.2. Onboard processing. Substantial onboard data processing is necessitated by the data rate constraints of the Mars Global Surveyor mission. The maximum data rate from the interferometer is $64,512 \text{ bit/s}$ (bps); once transformed into spectra, the maximum internal data rate is 5244 bps (Table 1). The available output rates are 1664 or 2485 bps during record mode and 4992 during real-time playback mode. Thus the data rate must be further reduced by compression, editing, and judicious selection between combinations of full spectral and full spatial sampling.

The onboard data-processing modes used most often to control data volume are spectral editing, spatial averaging, and data compression. Scientific requirements, orbital position (latitude and day/night position), and Mars season control the use of spatial averaging and spectral editing. Spectral editing averages or selects spectral points as defined by internal tables

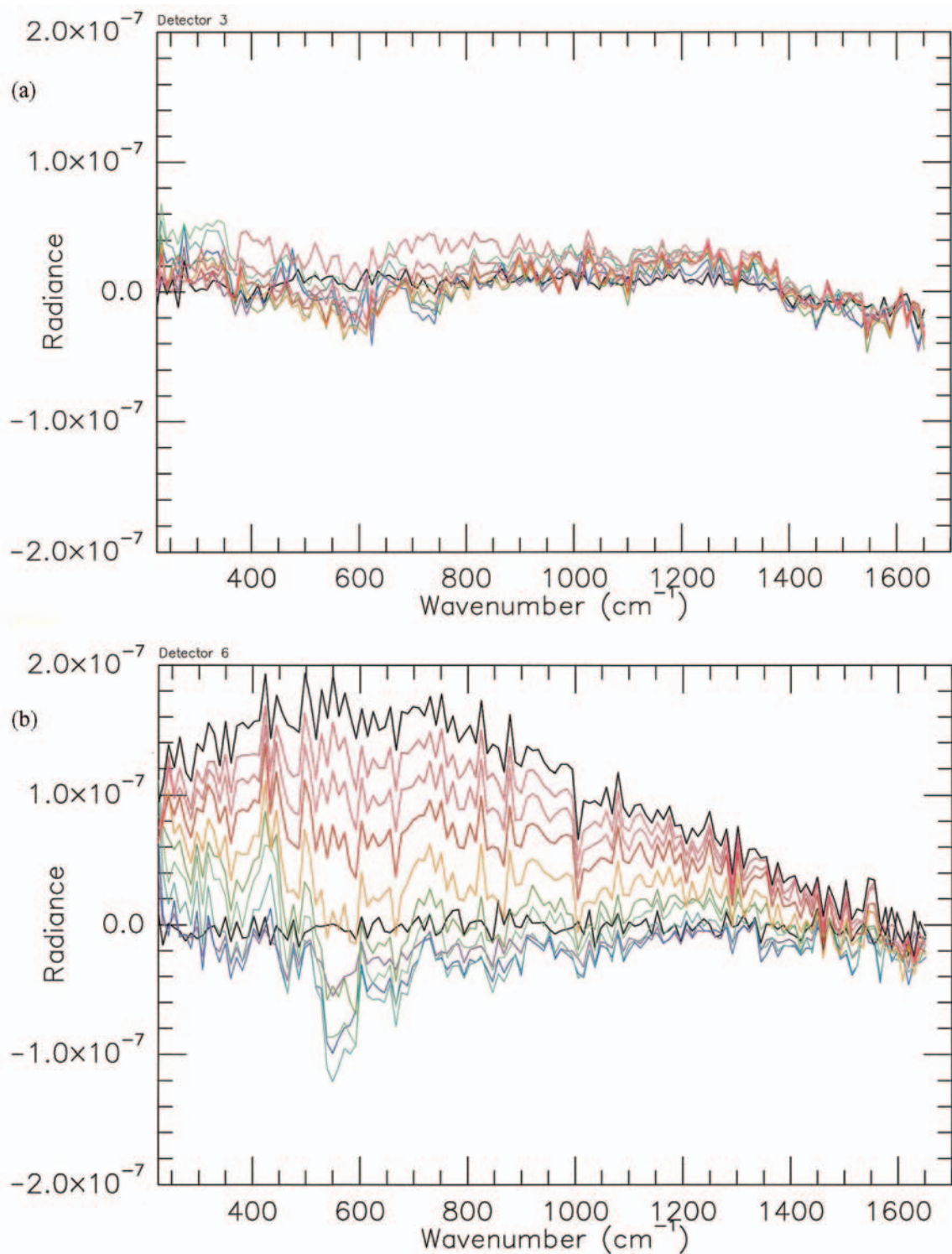


Plate 2. Absolute radiance due to the minor misalignment of the TES pointing mirror and secondary mirror assembly. As a result of this misalignment, the instrument energy is not perfectly removed by the calibration process. This error varies with pointing mirror angle and detector: (a) detector 3 (best case) and (b) detector 6 (worst case).

and retains only a limited number of spectral bands; it is used on both high-latitude and nightside data. Spatial averaging combines the raw data from selected combinations of detectors and is used mainly on high-latitude ($>60^\circ$) data.

3.2. Orbit Insertion Operations

3.2.1. Overview. The orbit insertion period is divided into four sections in TES data collection (see Table 2): (1) aerobraking phase 1, (2) science phasing 1, (3) science phasing 2,

Table 2. Mission Phase Divisions in TES Data

Mission Phase	Mission Subphase	TES Orbit		Date ^a		L_s	
		Start	End	Start	End	Start	End
Orbit insertion	aerobrake 1	3	137	9/15/97	2/18/98	181	277
	science phasing 1	214	268	4/2/98	4/28/98	303	318
	science phasing 2	383	551	6/23/98	9/12/98	349	28
	aerobrake 2	580	661	9/26/98	10/29/98	35	49
	MOC ^b	1583	1683	2/28/99	3/9/99	103	107
Mapping	calibration						
	fixed high gain	1684	1911	3/9/99	3/27/99	107	115
	nominal mapping	1987	5757	4/2/99	2/4/00	118	295
	beta supplement	5758	present	2/4/00	present	295	present

^aRead 9/15/97 as September 15, 1997.

^bMOC, Mars Orbiter Camera.

and (4) aerobraking phase 2. For aerobraking phases 1 and 2 the spacecraft utilized an aerobrake configuration ($\pm x$ axis to Mars) while skimming through the atmosphere and then began array normal spin (ANS) for the remainder of each orbit. During the science phasing 1 and 2 periods, the spacecraft assumed a mapping configuration ($+z$ axis to Mars) during each periapsis pass and ANS for the remainder of each orbit [Albee *et al.*, this issue]. Spectrometer and bolometer data were collected for aerobraking phase 1 and for both science-phasing periods. Failure of the primary neon lamp during aerobraking phase 2 limited data collection to the bolometers only for that period. The secondary neon lamp was reserved for the mapping portion of the mission.

During the insertion phase of the mission the equator-crossing information was commanded from the ground using navigation predictions. During this phase the equator-crossing event was not tied to surface latitude, but rather was set to the time of the spacecraft maneuver into aerobrake configuration prior to each periapsis pass. Ground-commanded equator-crossing information was radiated to TES from Earth for every

orbit during aerobraking 1 and once every few days during the remainder of the insertion period.

3.2.2. Data collection. The variety of spacecraft orientations during aerobrake and science-phasing orbits, the elliptical nature of the orbit itself, and record/playback rates were the main constraints in data collection during the orbit insertion period. Data collection was limited to periapsis plus 15 min and multiple 15-min periods during ANS. The majority of each orbit was spent in ANS mode and provided a view mainly of the south polar region. Apoapsis altitudes decreased dramatically as the orbit evolved into the circular mapping configuration.

During periapsis passes, TES observations included limb, limited EPFs (see Figure 3), surface, Mars Orbiter Camera (MOC) coincident observations, and reference data. The rationale for each observation type is given by Christensen *et al.* [1992]. Limb sequences started at 100-km altitude and stepped down in half-degree steps until reaching the surface. The EPF angles were designed to sample 1, 2, and 3 air masses during aerobraking passes and 2, 2.5, and 3 air masses during science-

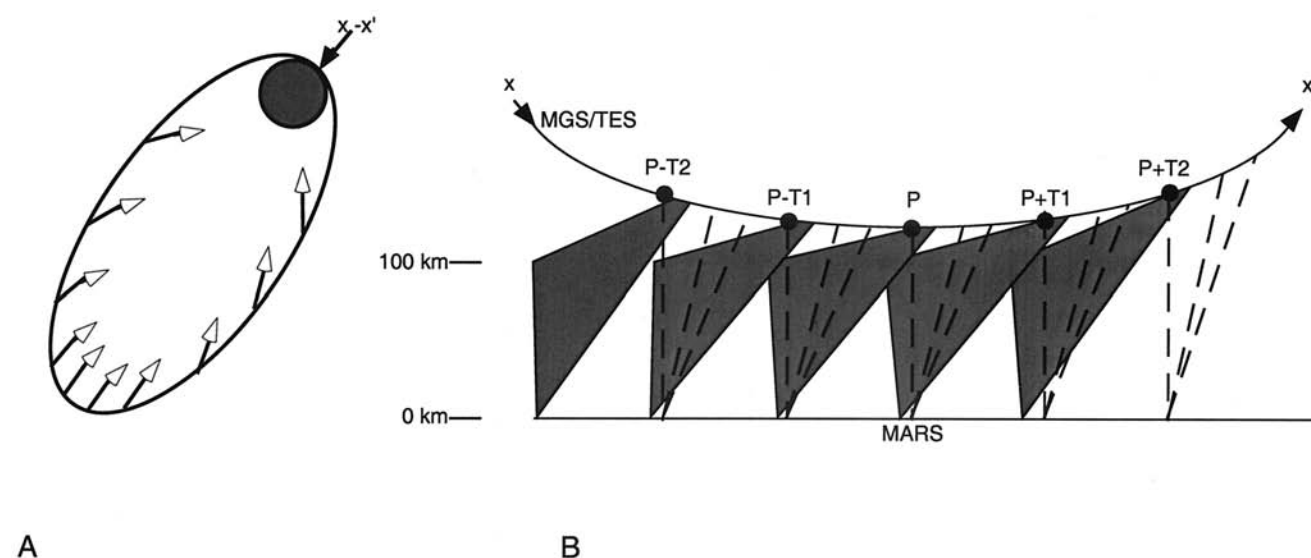


Figure 3. Typical TES aerobraking orbit observations. (a) Sketch of orbit ellipse (~ 11 -hour orbit shown) with available Mars viewing opportunities indicated by arrows. Open arrows indicate ANS observations; the closed arrow represents the periapsis pass location. (b) Details of the periapsis pass observations. Observations are uniformly spaced relative to the periapsis point. Dashed lines indicate the individual observations that comprise an emission phase function (EPF). Shaded polygons represent limb sets.

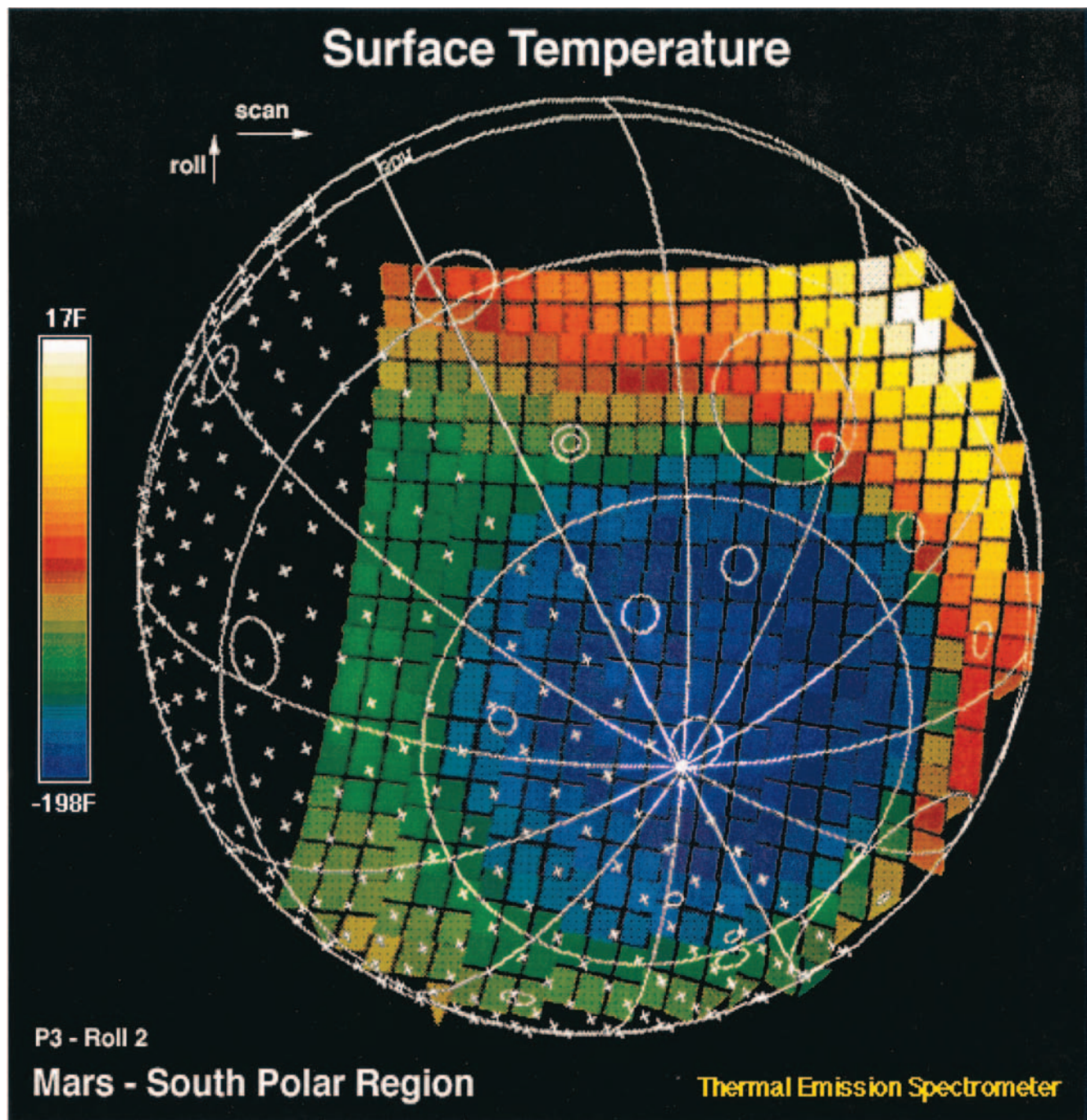


Plate 3. Array normal spin (ANS) mosaic example. Data are from the first TES ANS roll that was acquired and processed (orbit 3, ~4 hours after periapsis). Data shown are the $25\text{-}\mu\text{m}$ TES spectral data converted to brightness temperature.

phasing passes. Limb and EPF observations were collected only in the aft direction during aerobraking passes but in both the fore and aft direction during science-phasing orbit passes. All periapsis pass observations were timed relative to the periapsis point. Surface data were collected between the limb and EPF observations. Space and blackbody reference observations were collected prior to and following each periapsis pass. After each aerobraking periapsis pass the spacecraft was transitioned into ANS using a slew that swept the $+z$ axis (and therefore the MOC boresight) across the Martian surface. This

“rollout” to ANS was used for imaging by the MOC and for surface data collection by the TES.

By stepping the pointing mirror during ANS mode, mosaics of high southern latitudes were made (Plate 3). The number of mosaics per orbit varied with the number of ANS spacecraft rolls made during each orbit, with the number decreasing as the orbit apoapsis decreased. While the ANS roll rate was held constant, the decreased spacecraft velocity near apoapsis caused more rolls to occur at and around apoapsis when only the south pole of Mars was in view. Two modes of ANS mo-

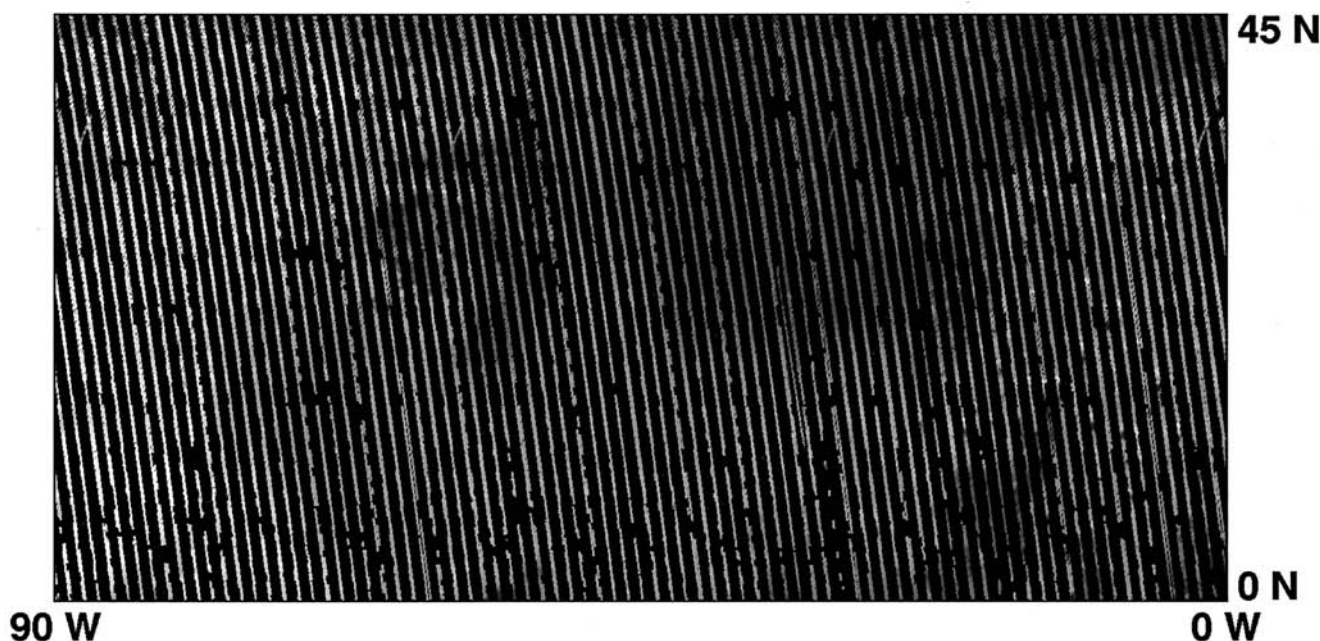


Figure 4. TES coverage example. TES daytime visible/near-IR albedo data, binned at 8 bins/degree over the L_s period from 270° to 330° , latitude 0° – 45° N, longitude 0° – 90° W. Each track represents a single dayside orbit pass, with the three individual cross-track TES instantaneous fields of view (IFOVs) also visible.

saics were used. “ANS sample” mode used uniform spacing across the available disk to provide complete coverage of the disk with gores. “ANS map” mode used contiguous spacing to eliminate gores, providing complete coverage of a limited portion of the available disk. ANS map mode was used only between periapsis -3 hours and periapsis $+3$ hours; further out from periapsis, ANS map mode produced the same result as ANS sample.

The observations for both the periapsis pass and the ANS portion of each orbit followed a consistent pattern during the entire orbit insertion period. Special observations during the orbit insertion period included instrument response studies, noise studies, and limited duration scientific targets such as the north polar haze, southern hemisphere dust storm, and four Phobos encounters (orbits 476, 501, 526, and 551).

3.3. Mapping Operations

3.3.1. Overview. Mapping operations have included four periods to date (Table 2): (1) MOC calibration; (2) fixed high-gain antenna mode; (3) normal mapping; and (4) “beta supplement” high-gain antenna mode [Albee *et al.*, this issue]. TES data can be collected throughout the entire orbit. The average spacecraft altitude is 400 km, resulting in a 9-km cross-track \times 6 km along-track coverage for the TES detector arrays. Figure 4 shows an example of the coverage obtained during dayside passes for the L_s period of L_s 270° – 330° .

During mapping operations the equator-crossing event occurs at the descending (nightside) equator. During MOC calibration and fixed high-gain operations, the equator-crossing information was commanded from the ground. In normal mapping and beta supplement modes, the spacecraft uses on-orbit positional knowledge and onboard autonomous algorithms to calculate the SCLK of each equator-crossing event. Several minutes prior to each equator-crossing event, the spacecraft broadcasts an equator-crossing command to the TES. The onboard generation of equator-crossing times has proven to be

very accurate, within ± 2 s of the equator-crossing time calculated in geometric reconstructions by the MGS navigation team.

The orbit numbering system employed by the MGS Project causes problems when searching TES records which are time sequential in nature; thus TES records are labeled with both MGS Project orbit numbers and TES Team orbit numbers, also known as Orbit Counter Keeper (OCK). During the orbit insertion phases, TES OCK and MGS Project orbit numbers were identical, except that the Project counted orbits from one periapsis to the next, while TES considered an orbit to begin at the spacecraft maneuver preceding periapsis, usually a difference of no more than 20 min. When the MGS Project reset its orbit count to 1 at the beginning of the mapping phase, TES OCK numbers were not reset, resulting in a difference of 1683 between the two systems. During mapping, both the TES and the MGS projects consider the beginning of an orbit to occur at the descending equator crossing.

3.3.2. Special spacecraft constraints. Several unexpected events have led to changes in MGS spacecraft operations during mapping. The high-gain antenna (HGA) has experienced a hardware problem inhibiting motion on one gimbal. Early in mapping a fixed HGA position was used such that 4 out of every 12 orbits were Earth pointed, rather than Mars pointed. After the fixed high-gain portion of the mission the antenna was placed in an auto-Earth-track mode. This allowed for full-day coverage of Mars. Eventually, the Earth-Mars angle increased until the stick point on the bad gimbal was reached. At this time the spacecraft was transitioned into a beta supplement mode that necessitated a three-part antenna rewind in the middle of the dayside pass. See Albee *et al.* [this issue] for a more detailed discussion of spacecraft operations during mapping.

Early in normal mapping operations, spacecraft microphonics induced by solar panel and high-gain antenna motions

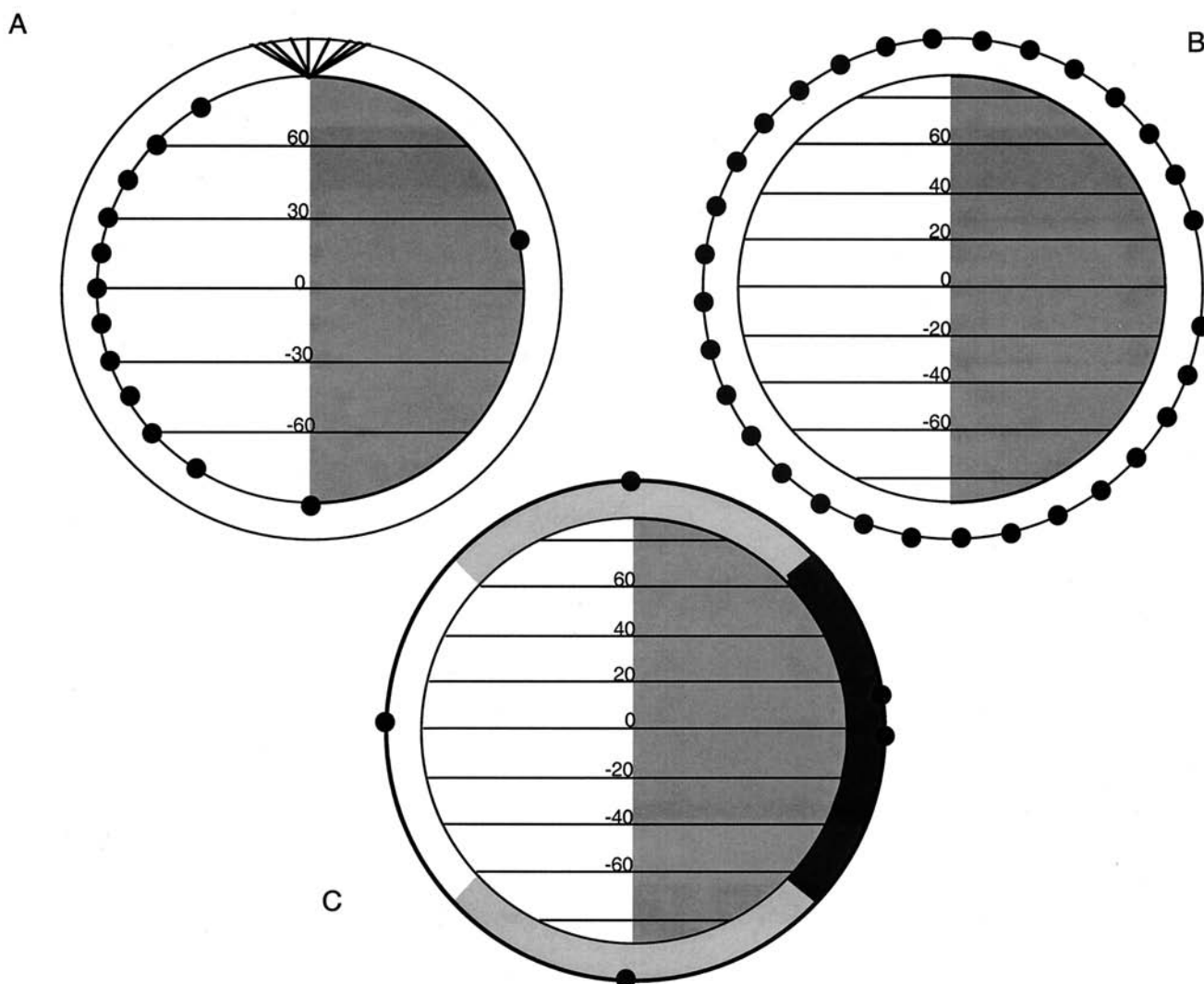


Figure 5. Diagrams of typical mapping phase TES observations. The outer circle represents the MGS orbital path (not shown to scale). (a) Sketch of emission phase function (EPF) placement during the 2-hour mapping orbit. EPFs cycle from -75° to $+75^\circ$ latitude over the course of 11 orbits (1 EPF/orbit). The twelfth orbit contains three EPFs at $+90^\circ$, -90° , and $+20^\circ$ (nightside). A sample EPF is shown at $+90^\circ$; dots mark the ground targets of the other 13 EPFs. (b) Sketch of limb set placement during the mapping mission phase. Limb sets are spaced $\sim 10^\circ$ apart around each orbit. Nightside gap is due to the equator-crossing event. (c) Generalized sketch of the surface and reference data collection. Dots represent locations of space/blackbody reference sets. Shaded bands between the MGS orbit and Mars' surface represent use of spatial and spectral editing. The white band indicates full spatial/full spectral data; dark gray indicates full spatial/edited spectral data; light gray indicates edited spatial/edited spectral data.

were found to cause noise in the TES data. The spacecraft team devised a three-step move-and-hold strategy for the solar panel array that optimized the rates and locations of solar array movements. This strategy took effect on TES orbit 3601. In addition, the HGA motion was stopped whenever the spacecraft was not in Earth contact or in rewind mode. These changes reduce the TES noise level by a factor of 5–10.

Image motion compensation (IMC) was a designed capability of the TES instrument; however, the stepper motor used for IMC was designed for an orbital profile with the $+x$ axis in the direction of motion. Owing to the additional time required to achieve aerobraking, the spacecraft has been flown in the opposite direction [Albee *et al.*, this issue], and the preprogrammed IMC cannot be used. An attempt was made to reverse IMC using a flight software patch. Unfortunately, testing

of the reversed IMC showed high noise levels in the reversed direction, and image motion compensation has not been used.

3.3.3. Data collection. TES observations during the mapping phase include observations of surface, the limbs, EPFs, and targeted mosaics (Figure 5). Special observations during this period included noise characterization studies, IMC studies, south polar observations in support of the Mars Polar Lander (MPL), 87°S coordinated views with MOC, and views of the geographic poles. Both the 10 and 5 cm^{-1} modes of the spectrometer have been utilized, and spatial and spectral editing have been used for data volume management.

Surface/nadir observations account for the majority of data collected on any single orbit. Because of this, spatial editing and spectral editing are most often applied to this type of data. TES collects ~ 3530 individual 2-s observations per orbit. As

telecommunication rates to Earth change, the amount of data that can be collected at full spatial, full spectral resolutions changes. Full spatial, full spectral data are collected for a latitude strip $\sim 50^{\circ}$ – 90° long that is centered on the subsolar latitude throughout the mission. Nightside spectrometer data are collected at full spectral resolution, but spatially averaged. High-latitude data are collected using both spatial and spectral editing. During the initial phase of mapping the surface data have been collected primarily in 10-cm^{-1} mode, with one orbit per week devoted to 5-cm^{-1} observations. Surface observations in the MGS extended mission will focus on 5-cm^{-1} observations.

Reference observations of both space and the internal blackbody surface are routinely collected five times per orbit (Figure 5). Space/reference sets contain three consecutive observations at each target. In addition, a set of three consecutive space observations is collected every ~ 18 min. Once per day, five consecutive observations of the visible/near-IR calibration lamp are collected.

Limb sets collected during mapping are similar to the insertion phase limb sets in that they start at 100 km above the surface and step down in half-degree steps. However, the mapping limb observations have all been in the forward direction and include two additional angles at the top of the limb set. The extra angles are a single observation of space and an observation at 75° pointing mirror angle to confirm the space observation. Limb sets are spaced evenly around the orbit (Figure 5). A two-orbit pattern is utilized, with the locations of the limb observations offset by 5° of latitude to reduce gores in nadir coverage. After ~ 400 days of mapping, both limb orbit locations were advanced $\sim 3^{\circ}$. Once per week one orbit has been dedicated to limb observations, collecting as many consecutive limb sets as possible given the data rate. During this orbit each limb set contains an additional three observations at 50° pointing mirror angle to view the surface beneath each limb. Limb data are typically collected in full spatial, full spectral 10-cm^{-1} mode, with three consecutive days per month dedicated to 5-cm^{-1} mode.

Two types of emission phase functions (EPFs) have been used during mapping. The first type views the target latitude using a limited set of seven to nine angles looking forward, nadir, and aft as the spacecraft orbits Mars. Five 2-s observations are collected at each angle. The second type of EPF uses a continual tracking mode, stepping the mirror 2° or 3° at a time to maintain a view of the target latitude for ~ 340 consecutive 2-s observations. Owing to the rotation of Mars during the MGS orbit, the EPFs do not view exactly the same longitude for the complete observation. Of the 12 daily MGS orbits, 11 contain a single dayside EPF that moves by 15° of latitude between each orbit from 75°S to 75°N (Figure 5). The twelfth orbit typically contains three EPFs, at 90°S , 90°N , and 20°N (nightside). The limited-angle type of EPF has been used on a daily basis, so that the entire latitude range is collected every day. The continual-tracking mode EPF observations are used every third day and cycle from 75°S to 75°N in 15° steps: for example, 75°S on the first day, 60°S on the fourth day, 45°S on the seventh day, etc.

Targeted mosaics are similar to EPFs but utilize the rotation of Mars to provide contiguous ground coverage (Plate 4), as described by Christensen *et al.* [1992]. A variety of targets have been selected, and a number of different instrument parameters have been applied in constructing mosaics. The typical mosaic covers an area of $\sim 1^{\circ}$ of longitude and 1.5° of latitude,

using five separate data collection periods each ~ 28 s in duration. Mosaics have been collected in both 10 and 5-cm^{-1} modes on both the dayside and nightside of Mars. Special cloud mosaics have targeted the summits of the major volcanoes, providing coverage of 1° of longitude and $\sim 4^{\circ}$ of latitude under uniform viewing conditions. Several times during the mapping mission, cloud mosaics with 12-hour spacing (i.e., day and night on the same day) have been collected.

4. Data Processing and Archiving

4.1. Overview

TES data-processing steps, from uplink to scientific analysis, are outlined in Figure 6, and significant details are discussed here. The key to successfully decoding the information downlinked from TES is a file of table addresses generated by the uplink software when the commands are originally built and compiled. Flight software allows TES to internalize the table and execute all commands: changing mirror angles, observation sequences, and orbit schedules. After data are collected, onboard data processing is performed to reduce the volume of data transmitted to Earth. During downlink the data must first be depacketized, a process which requires the use of the table address file to “decode” the pointing angles and observation details.

Following depacketization, the data are reformatted into the table-based ground database. At this point the spectral data and both thermal and visible/near-IR bolometers undergo calibration as described in section 2.7. Using navigation and ancillary spacecraft files, geometry information is merged into the data set. The five navigation files as a group are termed SPICE kernels, where the S kernel reports planet and spacecraft position, the P kernel contains constants and matrixes of planets and satellites, the I kernel contains instrument parameters, the C kernel reports the attitude of the spacecraft and instrument platform, and the E kernel is an event file generated by the experimenter. Initial validation of data takes place within ~ 1 week of data receipt on the ground, and recalibration is done as necessary. The addition of derived fields to the data set follows the processing of the raw data as the products are available.

4.2. Data Products Description

All TES Standard Data Products are in compliance with the guidelines set forth in the MGS Archive Generation, Validation, and Transfer Plan [Planetary Data System, 1995a; Arvidson *et al.*, 1998]. Data volumes are released at 3-month intervals, beginning in October 1999, and contain the data collected 6 months prior to the release date. This time lapse is used for Level 1 data and software generation and validation, data product documentation and assembly, and validation by the Planetary Data System (PDS). Volumes released throughout the duration of the primary mission include the raw data and initial calibration products; volumes released at end of mission are expected to include the rerelease of observation data, with associated derived products (new), and the initial release of TES Global Derived Surface Property Maps. CD-ROM volumes of TES Standard Data Products are available for distribution through the NASA Planetary Data System and the National Space Science Data Center. The TES standard data products are contained in PDS data set MGS-M-TES-3-TSDR-V1.0. This data set is available on PDS CD volumes MGST-Vxxx, where xxx is the volume number and is 001-080

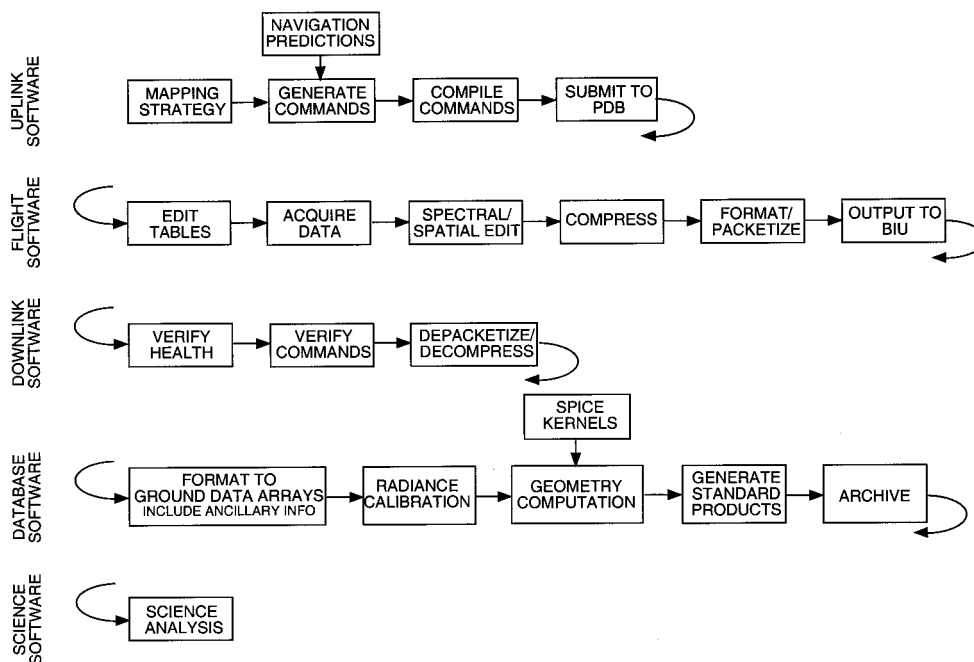


Figure 6. TES data flow diagram. The top line represents command generation, the second line contains actions in the instrument (TES observations occur in the second box), the third line is initial processing of telemetry received on Earth and engineering assessment, and the fourth line represents preparation of the database and standard products. The fifth line is where the fun starts.

for the orbit insertion phase (Table 2) and 100-999 for the mapping phase of the mission.

4.3. Standard Data Products

The TES Standard Data Products include the following elements: raw and calibrated thermal IR radiance spectra; raw and calibrated visual/near-IR and thermal bolometric radiance measurements; observation parameters; selected downlinked diagnostic information; TES pointing and positional information (calculated from MGS SPICE kernels); and derived atmospheric and surface properties. The products are sorted by general data type and stored within the 10 tables listed in Table 3. Each table comprises a separate file with the data products in a PDS table structure [*Planetary Data System*, 1995b] of fixed-length binary records (table_name.DAT) with internal pointers to handle the variable-length spectra (table_name.VAR). The PDS HEADERS are stored in an associated, readable text file (table_name.FMT) in the same directory as the data files.

Available individual fields are listed by processing level in

Table 3. TES Data Tables

Table Name	Standard Abbreviation
Observation Parameters	OBS
Raw and Calibrated Radiance Data	RAD
Bolometer Data	BOL
Derived Positional and Geometric Values	GEO
Raw Positional and Geometric Data	POS
Auxiliary Observation Parameters	TLM
Raw Interferogram Data	IFG
Raw Complex Data	CMF
Surface Observations (Derived Properties)	SRF
Atmospheric Limb Observations (Derived Properties)	LMB

Appendix C: raw fields, MGS SPICE kernel fields, calibrated fields, and derived fields. Every record within the field is keyed to spacecraft time; for tables with radiance values, up to six detectors can be associated with a given time. Software available on each TES CD-ROM can be used to retrieve fields of records using time, and detector if necessary, as a common key.

For all TES Standard Data Products, the following standards for time, coordinates, and orbit numbering have been employed. The time value stored with each TES data record is the value of the spacecraft clock at the start of the observation, truncated to an integer value; this number is equal to the number of seconds since 0000 UT, January 1, 1980. The Mars latitude and longitude coordinates associated with each TES data record are computed using an areocentric coordinate system with west longitudes.

5. Surface Mineralogy

5.1. Key Questions

Some of the key questions regarding surface composition of Mars concern (1) the temporal and spatial variation in the composition of volcanic materials, (2) the existence of aqueous or hydrothermal deposits, (3) the existence and location of carbonates and other salts, (4) the composition and abundance of weathering products, (5) the mineral phase of sulfur, (6) the relationship of SNC meteorites to regional composition, (7) the composition of unique surfaces such as “White Rock,” (8) the composition and origin of Martian dust, (9) the composition and distribution of channel sedimentary deposits, and (10) the composition of the polar layered deposits.

5.2. Vibrational Spectroscopy Overview

The remote sensing of Mars using TES is based on vibrational spectroscopy, which in turn is based on the principle that

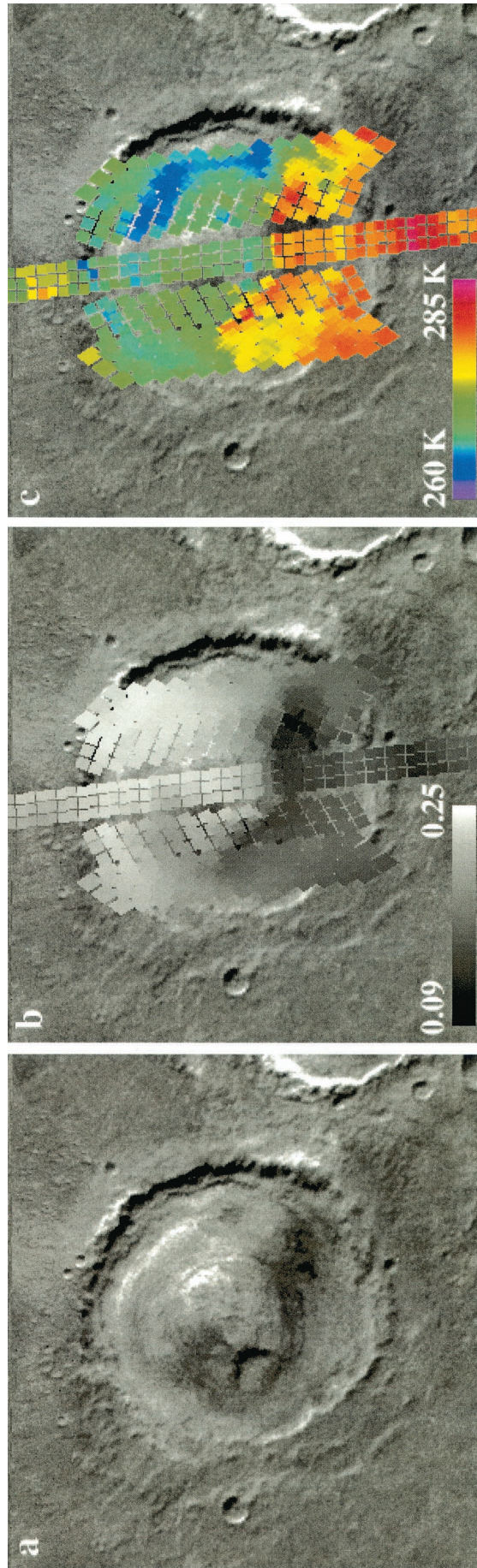


Plate 4. Mosaic design. Temperature and albedo data from a single TES mosaic (orbit 6168, ICKs 1711–1835) are shown superimposed on a Mars Viking image base map. The outline of each individual TES detector is shown for the thermal and albedo data. The image is centered at 2.5°N, 9.6°W. (a) Viking base map. (b) TES albedo mosaic. (c) TES daytime temperature mosaic.

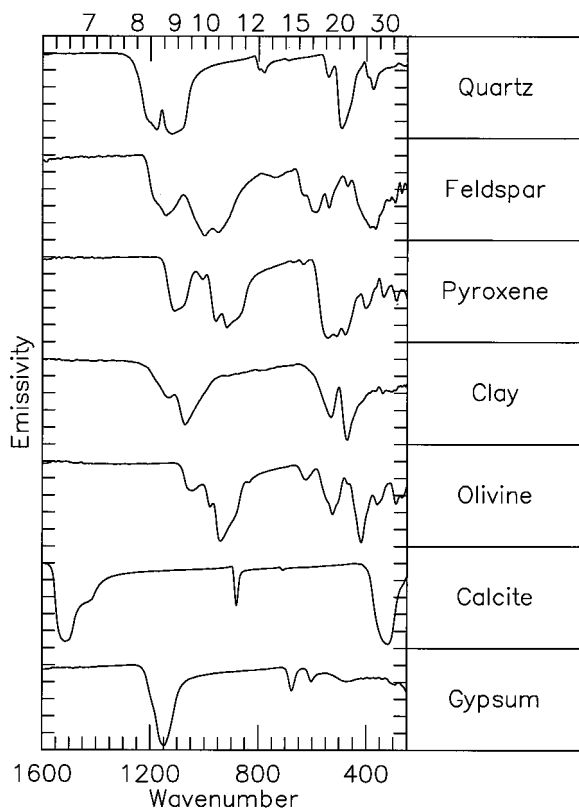


Figure 7. Thermal infrared spectra of representative silicate, carbonate, and sulfate minerals. Laboratory data are from the Arizona State University (ASU) spectral library [Christensen *et al.*, 2000a].

vibrational motions occur within a crystal lattice at fundamental frequencies that are directly related to the crystal structure and elemental composition (i.e., mineralogy) [Wilson *et al.*, 1955; Farmer, 1974]. The fundamental vibrational frequencies of these motions occur within the thermal infrared ($\sim 5\text{--}100\ \mu\text{m}$) for geologic materials, and the TES was specifically designed to observe these fundamental bands. The fundamental vibrations vary significantly with different anion groups, such as CO_3 , SO_4 , PO_4 , and SiO_4 , to produce unique, well-separated bands that allow carbonates, sulfates, phosphates, silicates, oxides, and hydroxides to be readily identified (Figure 7).

The stretching and bending vibrational modes that typically occur at wavelengths greater than $\sim 15\ \mu\text{m}$ involve major cations (e.g., Mg, Fe, Ca, and Na) and provide additional discriminability of minerals within mineral groups (e.g., silicates) [e.g., Salisbury *et al.*, 1991; Salisbury, 1993; Lane and Christensen, 1997; Christensen *et al.*, 2000a]. Additional overtones and combination tones occur in the 1- to $5\text{-}\mu\text{m}$ region for many minerals, but these are typically weaker than the fundamental frequencies.

Extensive work over the past 40 years has demonstrated the utility of vibrational spectroscopy for the quantitative determination of mineralogy and petrology [e.g., Lyon, 1962; Lazerev, 1972; Farmer, 1974; Hunt and Salisbury, 1976; Salisbury *et al.*, 1987, 1991; Salisbury, 1993; Christensen and Harrison, 1993; Lane and Christensen, 1997; Hamilton, 2000; Christensen *et al.*, 2000a]. Individual mineral components can be identified and rock types can be distinguished, allowing both the mineralogy

and petrology to be determined [Walter and Salisbury, 1989; Feely and Christensen, 1999; Hamilton and Christensen, 2000]. Significant work has also been done in the development of quantitative models to predict and interpret vibrational spectra produced by emission from natural particulate surfaces [Conel, 1969; Salisbury and Eastes, 1985; Salisbury and Wald, 1992; Moersch and Christensen, 1995; Mustard and Hays, 1997; Ramsey and Christensen, 1998]. Surface and atmospheric dust/volatile components can be discriminated using limb, emission phase function, and day-night observations [Smith *et al.*, 2000a; Bandfield *et al.*, 2000b]. These advances have led directly to the ability to successfully interpret and analyze the extensive set of spectra acquired of the Martian surface by the TES instrument.

5.3. TES Results

5.3.1. Surface-atmosphere separation. Two models have been developed for separating the surface and atmospheric components of TES spectra [Smith *et al.*, 2000a]. These models use radiative transfer and linear deconvolution algorithms, together with atmospheric dust and water-ice cloud spectral properties, to isolate the surface and atmospheric spectra. The atmospheric dust spectrum was isolated using factor analysis and target transformation techniques on TES spectra from a wide range of surfaces and atmospheric dust loading [Bandfield *et al.*, 2000b]. This dust spectrum is interpreted to contain little, if any, surface spectral character primarily on the basis of (1) the close similarity between the derived dust spectrum and spectra acquired with high dust opacity and on the limb and (2) the consistency of surface spectra derived for atmospheric dust opacities that varied by a factor of 5–10 [Smith *et al.*, 2000a; Christensen *et al.*, 2000b].

The radiative transfer method uses a successive least squares fitting to simultaneously model the spectral properties of atmospheric dust, atmospheric water ice, and surface emissivity and the derived atmospheric temperature gradient in each TES spectrum [Smith *et al.*, 2000a]. The deconvolution algorithm assumes that the TES spectra are linear combinations of atmosphere and surface spectral shapes and performs a linear least squares fit to a library of dust, ice, and mineral spectra to determine the abundances of all components [Adams *et al.*, 1986; Ramsey and Christensen, 1998; Bandfield *et al.*, 2000b]. The atmospheric components are then removed in accordance with their derived abundances to give a surface-only spectrum [Smith *et al.*, 2000a].

Smith *et al.* [2000a] derived atmosphere-removed, surface-only spectra for the dark region in Cimmeria Terra at 24.8°S , 213.3°W using both the radiative transfer and deconvolution algorithms. Data were collected of this region with an infrared atmospheric dust opacity, measured by TES at $9\ \mu\text{m}$, of 0.11 and 0.33 and with different water-ice abundance and atmospheric temperatures. Both atmosphere-removal models were applied to the two different atmospheric conditions, yielding four independent derivations of the surface-only spectrum [Smith *et al.*, 2000a]. An estimate of the errors in the surface spectra due to the combined instrumental and atmospheric modeling effects was obtained by comparing the four surface spectra derived from the two atmosphere-removal models and is indicated by the $1\text{-}\sigma$ error bars in the derived surface spectra for Cimmeria in Plate 5 [Christensen *et al.*, 2000b]. All of the random and systematic instrumental uncertainties in the original spectra, as well as the uncertainties produced by the dif-

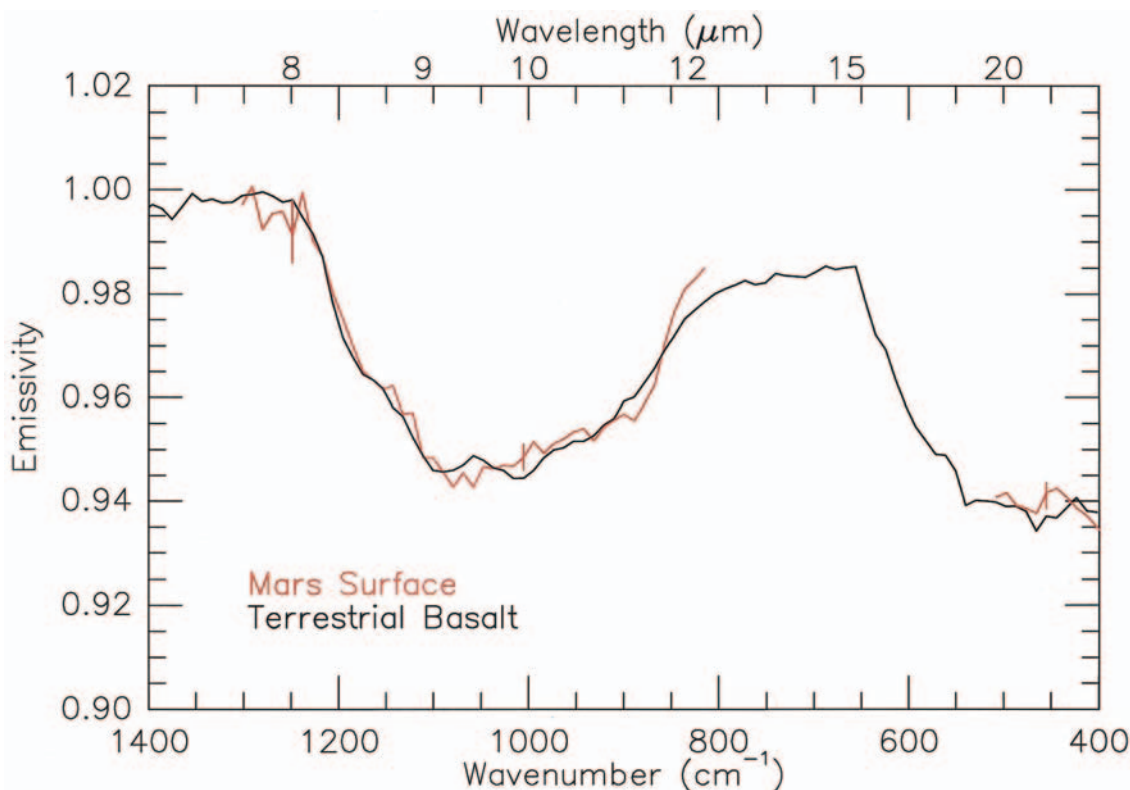


Plate 5. Comparison of a particulate Deccan flood basalt sample and Mars Cimmeria Terra spectra. No scaling, contrast enhancement, or continuum removal has been applied to either spectrum. Both the spectral shape and contrast of the TES and Deccan basalt match well. Data are from *Christensen et al.* [2000b].

ferent atmosphere-removal models, are included in this uncertainty estimate.

5.3.2. Volcanic composition. A major question in Martian evolution is the composition of the erupted lavas and the degree of change in composition that has occurred in both time and space. These compositions provide constraints on the composition and the depth and degree of partial melting within the crust and upper mantle. Variations observed for terrestrial, lunar, and meteoritic basalts show major differences in source composition, degree of partial melting, and melt fractionation [e.g., *Basaltic Volcanism Study Project*, 1981]. The distribution and geologic ages of primary igneous materials provide important clues to the degree of heterogeneity of the Martian upper mantle and the evolution of the crust and mantle composition with time. Any evidence of a variation in the mineralogy and petrology of these lavas with time provides a measure of the evolution of Martian magmas, both on a global basis and for individual eruptive centers.

5.3.2.1. Identification: Detailed spectral analyses have been performed for typical low-albedo surface units across the planet [*Christensen et al.*, 2000b; *Bandfield et al.*, 2000a]. The mineralogy of low-albedo materials falls into two categories: (1) basalt to low-silica basaltic andesite and (2) basaltic andesite to andesite [*Bandfield et al.*, 2000a; *Christensen et al.*, 2000b] (Plates 5 and 6). The Mars surface spectra do not match terrestrial high-silica igneous rocks (granite and rhyolite), ultramafic igneous rocks, limestone, or quartz- and clay-rich sandstone and siltstone.

Plate 7 shows a typical TES spectrum of the basaltic surface compared with the best fit spectrum determined by a least squares fit with the ASU spectral library [*Christensen et al.*,

2000a; *Ramsey and Christensen*, 1998]. The primary mineral identified is intermediate plagioclase feldspar with an abundance of 50%. The second most abundant mineral is clinopyroxene (25%), with a combination of augite and minor diopside providing the best fit in the deconvolution model [*Bandfield et al.*, 2000a; *Christensen et al.*, 2000b]. The best fit includes only Ca-rich clinopyroxenes (augite and diopside), even though a full suite of pyroxene compositions was included in the deconvolution model [*Bandfield et al.*, 2000a; *Christensen et al.*, 2000b]. No orthopyroxene compositions are required to match the basaltic spectra. The primary mineral identified in the andesitic surface is plagioclase, but at a lower (35%) abundance than in the basalt, along with high-silica glass with an abundance of 25% and minor pyroxene [*Bandfield et al.*, 2000a].

Olivine (12%) [*Christensen et al.*, 2000b] and sheet silicates (11–15%) [*Bandfield et al.*, 2000a; *Christensen et al.*, 2000b] were also selected in the best fit match to the TES spectra but are near the current TES detection limit for these minerals [*Christensen et al.*, 2000b]. Feldspars and high-silica glass alone provide an acceptable match to the andesite unit. Olivine has been reliably identified in higher abundances in the region of northeast Syrtis Major [*Clark and Hoefen*, 2000; *Hoefen et al.*, 2000]. Carbonates, quartz, and sulfates have not been identified at detection limits of ~5, 5, and 10%, respectively [*Christensen et al.*, 2000b].

The TES data provide the first observation of feldspar and high-silica glass on Mars. The abundance of plagioclase feldspar derived from the TES data using the full mineral library varies from 35 to 53%, depending on surface type and, to a lesser extent, on the exact atmospheric model used, while the

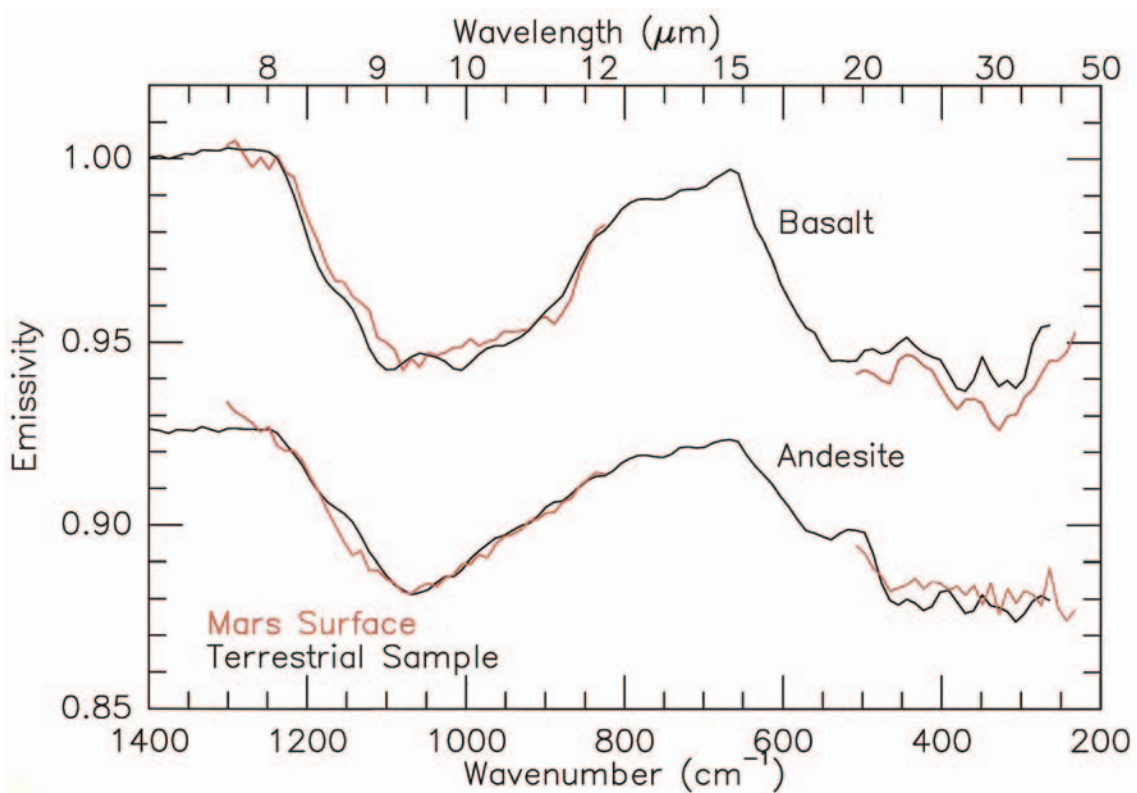


Plate 6. Average basalt and andesite spectra. These spectra are typical examples of the spectral classes identified by *Bandfield et al.* [2000a] as basalt and andesite on the basis of their derived mineralogy. Also shown are terrestrial examples of typical basalt and andesite rocks. Data are from *Bandfield et al.* [2000a].

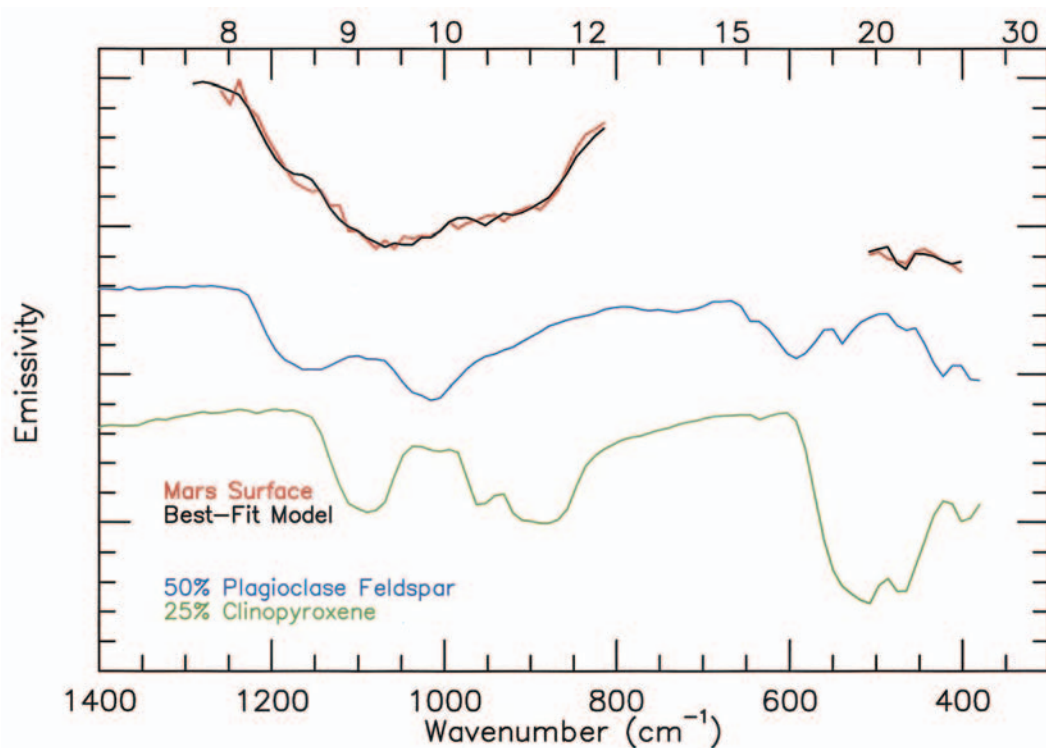


Plate 7. Atmosphere-removed Martian surface spectrum compared with a best fit deconvolution model spectrum. The two major individual mineral components (plagioclase feldspar and clinopyroxene) that make up the best fit model are also shown.

abundance of pyroxene varies from 10 to 26%. The plagioclase feldspar/pyroxene ratio in the basaltic unit varies from 2.8 to 1.8 between the atmospheric models that include the secondary components and from 1.9 to 1.2 for models with plagioclase feldspar and pyroxene alone [Christensen *et al.*, 2000b]. In all models, plagioclase feldspar is the dominant mineral present in Martian low-albedo regions.

The qualitative match of these TES surface spectra to the spectra of basalt and andesite (Plates 5 and 6), without any further modeling, provides excellent evidence for basaltic materials exposed on the surface of Mars [Bandfield *et al.*, 2000a; Christensen *et al.*, 2000b]. It is important to note that the spectral contrast of the Martian surface spectra closely matches the contrast observed in laboratory samples of basaltic and andesitic sands. No scaling, contrast enhancement, or continuum removal was applied to the spectrum shown in Plate 5. The dark region spectra observed by the TES instrument are consistent with what is expected for particulate basaltic materials on the surface; no unusual particle size or other environmental effects are observed in these data. This match in band depth, as well as shape, provides strong evidence that all of the major surface components have been identified.

The match to sand-sized particles is also consistent with the thermal inertia and albedo values derived for dark regions, which are typically composed of coarse-grained (100- to 500- μm) particles [Palluconi and Kieffer, 1981; Edgett and Christensen, 1991; Mellon *et al.*, 2000]. The spectral contrast observed in dark regions matches that found in terrestrial remote-sensing observations [Gillespie *et al.*, 1984; Hook *et al.*, 1994; Ramsey *et al.*, 1999] and confirms the expectations of spectral contrasts in Martian surface materials that were used in the TES instrument design [Christensen *et al.*, 1992].

5.3.2.2. Global basalt/andesite mapping: Detailed analysis of the global atmospherically corrected TES data set has shown that dark region spectra can be separated into two units (Plate 6) that are geographically distinct (Plate 8) [Bandfield *et al.*, 2000a]. The distribution of the two observed units is split roughly along the planetary dichotomy. The basaltic composition is confined to older surfaces, and the more silicic surface type has the highest concentrations in the younger northern plains (Plate 8) [Bandfield *et al.*, 2000a]. These results indicate that Mars is dominated by volcanic compositions that are similar to the major volcanic classes present on the Earth. However, the explanations for the apparent age relationships and the mechanisms for producing vast quantities of andesite remain under investigation.

5.3.2.3. Comparison with SNC meteorite spectra: An initial search of the TES data has been performed to detect potential source regions for the SNC meteorites. Neither the spectral shapes nor the derived mineralogies match well with the spectral shapes and mineralogies of the SNC meteorites [Hamilton *et al.*, 1997].

5.3.3. Aqueous mineralization. Crystalline gray hematite ($\alpha\text{-Fe}_2\text{O}_3$) has been identified from TES data, and its occurrence has been mapped globally (Plate 9) [Christensen *et al.*, 2001]. This mapping has revealed the presence of three remarkable accumulations of crystalline hematite in the equatorial region [Christensen *et al.*, 2000c, 2001]. One, centered near 2°S latitude between 0° and 5°W longitude in Sinus Meridiani, covers an area with sharp boundaries approximately 350 \times 750 km in size (Plate 10). The second occurs within Aram Chaos (Plate 10), a 300-km-diameter ancient crater basin that has been filled with sediments and disrupted by subsequent chaos

and outflow channel formation [Christensen *et al.*, 2001]. The third occurs in scattered locations throughout the Ophir/Candor region of Valles Marineris [Christensen *et al.*, 2001].

Crystalline hematite is uniquely identified by the presence of fundamental vibrational absorption features centered near 300, 450, and $>525\text{ cm}^{-1}$ and by the absence of silicate fundamentals in the 1000-cm^{-1} region [Christensen *et al.*, 2000c]. The depth and shape of the hematite fundamental bands show that the hematite is crystalline and relatively coarse grained ($>10\ \mu\text{m}$) [Christensen *et al.*, 2000c] and is distinct from the fine-grained (diameter $<5\text{--}10\ \mu\text{m}$), red, crystalline hematite considered to be a minor spectral component in Martian bright regions [Morris *et al.*, 1997; Bell and Morris, 1999; Morris *et al.*, 2000].

The Sinus Meridiani material is interpreted to be an in-place sedimentary unit characterized by smooth, friable layers [Edgett and Parker, 1997; Christensen *et al.*, 2000c] that are composed primarily of basaltic sediments with $\sim 10\text{--}15\%$ crystalline gray hematite [Christensen *et al.*, 2000c, 2001]. The hematite in Aram Chaos appears to occur in a sedimentary layer that formed within this closed basin during basin infilling and predates the formation of the chaos and outflow terrains [Christensen *et al.*, 2001]. The Ophir/Candor materials occur in small deposits (typically $<50\text{ km}$) that appear to be associated with the interior layered deposits [Christensen *et al.*, 2001].

Formation modes for gray hematite detected by TES can be grouped into two classes: (1) chemical precipitation and (2) thermal oxidation of magnetite-rich lavas. Chemical precipitation includes (1) precipitation of Fe oxides/oxyhydroxides at ambient temperatures from standing, oxygenated, Fe-rich water, followed by subsequent alteration to gray hematite (e.g., oxide iron formations), (2) precipitation from Fe-rich circulating fluids of hydrothermal or other origin, (3) low-temperature aqueous dissolution and leaching of iron-bearing silicates to form a residual precipitate rich in hematite (e.g., similar to a laterite), and (4) formation of hematitic surface coatings during weathering [Christensen *et al.*, 2000c, 2001].

We conclude that these deposits of gray hematite most likely formed by chemical precipitation from aqueous fluids under either ambient or hydrothermal conditions [Christensen *et al.*, 2000c, 2001]. Weathering and alteration processes, which produce nanophase and red hematite, are not consistent with the coarse, crystalline hematite observed in Sinus Meridiani. In addition to the mineralogic evidence of coarse-grained, aqueous hematite, the geologic context suggests that all three sites are sedimentary environments. Hematite-bearing units in Aram and Valles Marineris occur in closed sedimentary basins consistent with deposition in water. Subsurface water has been present in Aram Chaos, and the hematite-bearing unit in Ophir/Candor is associated with layered, friable deposits that may be of aqueous origin [McCauley, 1978; Lucchitta, 1982; Nedell *et al.*, 1987].

The TES evidence for aqueous mineralization, under either ambient or hydrothermal conditions, indicates that liquid water was stable at or near the surface, possibly for millions of years by analogy with terrestrial iron formations, in limited locations on early Mars. Overall, crystalline gray hematite is extremely uncommon at the surface, yet, where exposed, it is closely associated with sedimentary units [Christensen *et al.*, 2000c, 2001]. These sites may be ideal candidates for future landed missions searching for biotic and prebiotic environments; they provide evidence for sustained liquid water, and

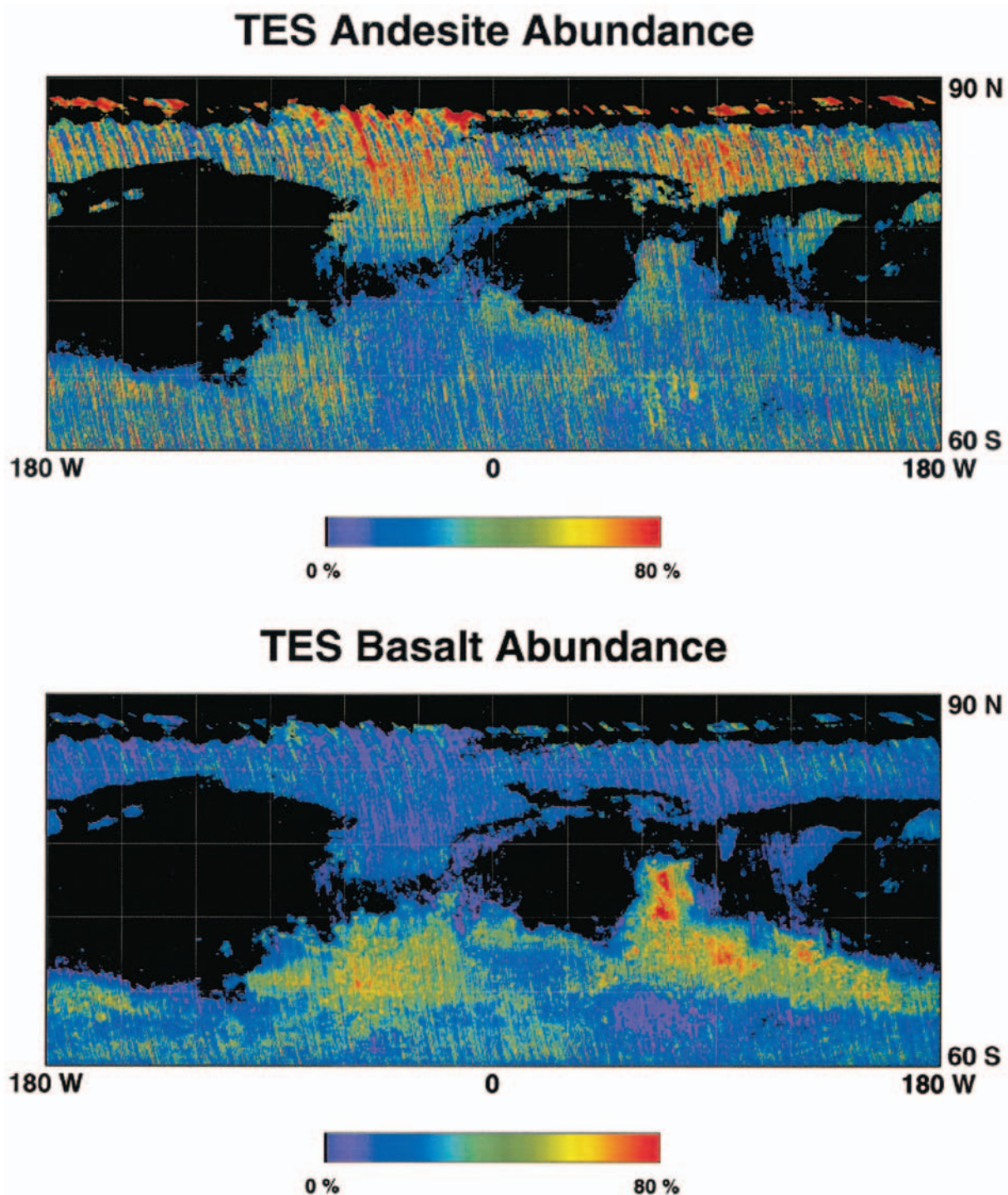


Plate 8. Global map of andesite and basalt abundance. Regions of high dust content (albedo >0.23) where the surface compositions are obscured have been masked. The basaltic unit occurs predominately in the southern hemisphere; the andesite unit is predominately in the northern lowlands. Data are from *Bandfield et al.* [2000a].

their physical characteristics satisfy the engineering requirements for the missions currently planned.

5.3.4. Carbonates and sulfates. Carbonates in the regolith have long been proposed to play an important role in the CO_2 exchange cycle, acting as a reservoir for sequestering large amounts of CO_2 from the ancient Martian atmosphere and allowing long-term exchange between the surface and atmosphere [e.g., *Booth and Kieffer*, 1978; *Fanale and Jakosky*, 1982;

Kahn, 1985; *Fanale et al.*, 1992]. More recently, arguments have been made for CO_2 loss to space [e.g., *Melosh and Vickery*, 1989; *Kass and Yung*, 1995; *Brain and Jakosky*, 1998], which would suggest that large carbonate deposits may not exist. Thus the presence, or absence, of carbonates has important implications for the evolution of the Martian atmosphere, placing constraints on the abundances, reaction chemistry, and history of H_2O and CO_2 .

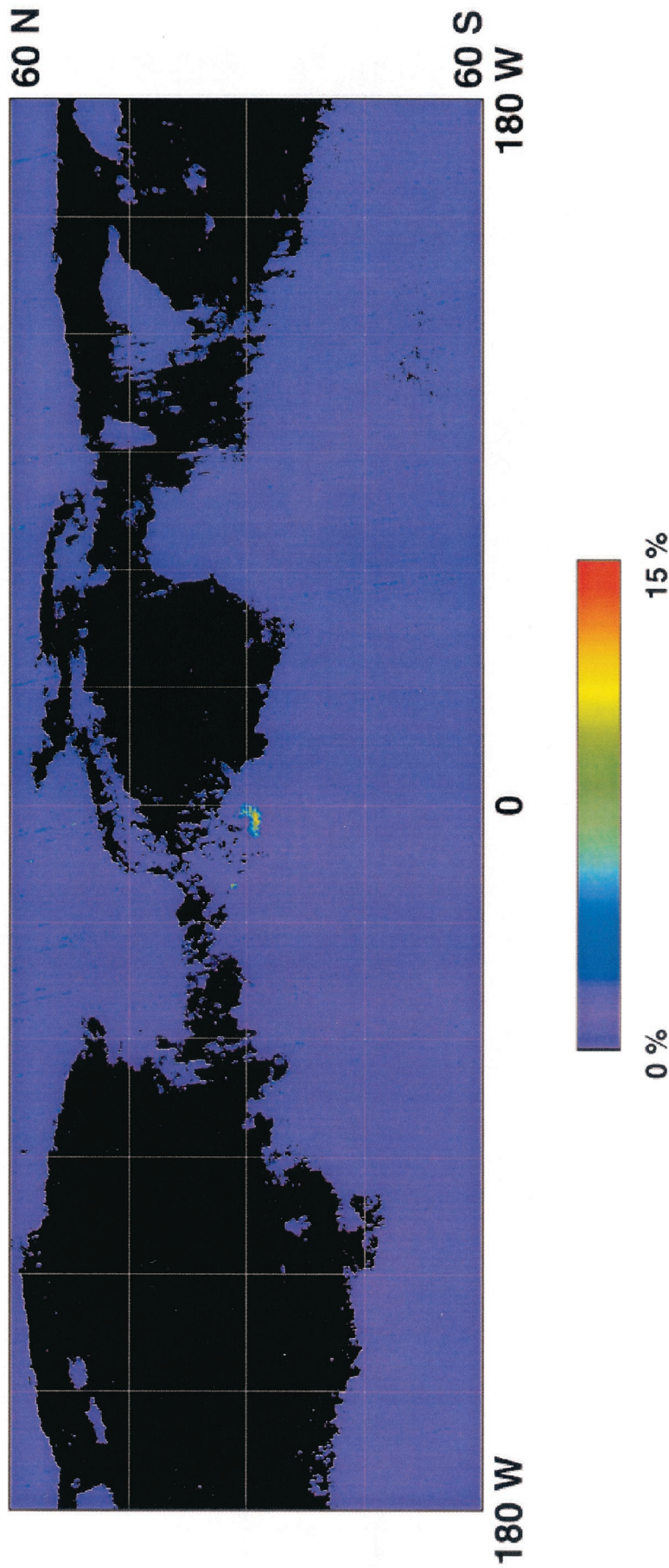


Plate 9. Equatorial hematite abundance map in cylindrical projection. Hematite abundance is shown as the relative band depth of the 300- and 450-cm⁻¹ absorption bands [Christensen *et al.*, 2000c], with purple representing no hematite abundance and red representing the maximum hematite abundance. Regions of high dust content (albedo > 0.23) where the surface compositions are obscured have been masked. Note the remarkable lack of hematite except in localized regions such as Sinus Meridiani. Data are from Christensen *et al.* [2001].

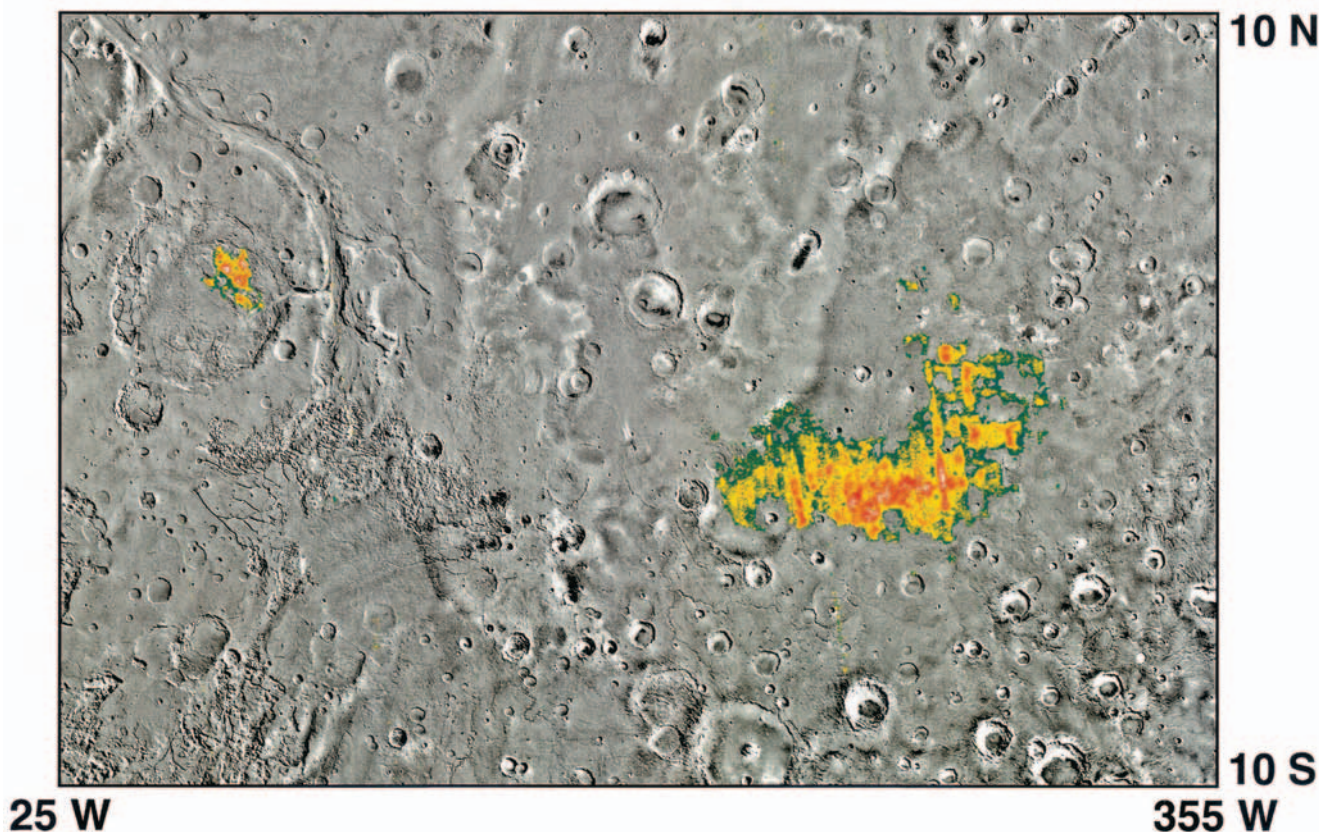


Plate 10. TES-derived hematite abundance is shown overlaid on a Viking base digital photomosaic image. The two major occurrences in Sinus Meridiani and Aram Chaos are illustrated. Hematite index values of <1.019 , corresponding to hematite abundances below the TES detection limit ($\sim 2\%$), have been made transparent to allow the underlying morphology to be visible. Data are from *Christensen et al.* [2001].

The TES wavelength range includes two fundamental carbonate spectral features centered near 1500 cm^{-1} ($6.67\text{ }\mu\text{m}$) and 400 cm^{-1} ($25\text{ }\mu\text{m}$), as well as a minor band near 890 cm^{-1} ($11.25\text{ }\mu\text{m}$) (Figure 7). These features are separate and easily distinguishable from features in silicate and other mineral groups. Of these, only the minor $11.25\text{ }\mu\text{m}$ band is detectable in terrestrial remote sensing applications due to the opacity of the Earth's atmosphere [*Kahle et al.*, 1993]. As seen in Figure 7, however, the 6.7- and $25\text{-}\mu\text{m}$ C-O bands are significantly deeper and broader than the $11.25\text{-}\mu\text{m}$ band, making carbonates far more readily detected and identified on Mars than on Earth.

The search for carbonates is somewhat complicated by the presence of water vapor and CO_2 absorptions in the 1200- to $>1700\text{-cm}^{-1}$ and 250- to 450-cm^{-1} regions [*Maguire*, 1977] and by water-ice absorptions in the 180- to 280-cm^{-1} region (Plate 11) [*Curran et al.*, 1973; *Warren*, 1984]. However, there are sufficient differences between carbonates and water to allow these two components to be uniquely identified. Plate 11 shows representative averaged spectra from bright (Arabia: $6.6\text{-}10.7\text{N}$, 322.7W) and dark (Syrtis Major: $0\text{-}1.7\text{N}$, 293W) regions. There is significant spectral structure in the 1200- to 1650-cm^{-1} region, but as shown in Plate 11, this structure is due primarily to atmospheric CO_2 and H_2O . Additional surface spectral features due to particle size effects are present in the bright, fine-grained material [*Ruff and Christensen*, 1999; S. W. Ruff, manuscript in preparation, 2001]. Plate 11 also shows a scaled laboratory spectrum of calcite, corresponding to

a surface abundance of $\sim 10\%$ [*Lane*, 1999]. The strong carbonate bands in the 300- to 400- and 1450- to 1550-cm^{-1} regions are not observed in the TES spectra (P. R. Christensen et al., manuscript in preparation, 2001).

To date, TES has not detected any evidence for carbonates on Mars, and it is possible to conclude that large-scale (greater than tens of kilometers sized) carbonate deposits are not currently exposed at the surface of Mars (P. R. Christensen et al., manuscript in preparation, 2001). Dark regions, because of their larger particle size and lack of surficial dust [*Palluconi and Kieffer*, 1981; *Christensen*, 1989], provide the best opportunity to view the spectral properties of in-place geologic materials (see above) [*Christensen et al.*, 2000c; *Bandfield et al.*, 2000a]. The fact that TES spectra have shown abundant basalt, andesite, hematite-rich, and olivine-rich units demonstrates that the TES spectra can successfully identify mineral components if they are exposed at the surface at greater than $\sim 10\%$ abundance. Global searches for carbonate signatures, however, have thus far failed to provide any positive identification of carbonate in either dark or bright regions (e.g., Plate 11).

We cannot preclude burial of carbonates by younger rock units or surficial deposits, and UV dissociation of carbonate to calcium oxide has been proposed as a means of destroying the uppermost surface of exposed carbonates [*Mukhin et al.*, 1996]. It is also possible to argue that carbonates are disseminated as fine grains ($<50\text{ }\mu\text{m}$) at low abundances ($<10\%$) throughout the surface materials. The detection of aqueous mineralized hematite units, however, demonstrates that unusual, and pre-

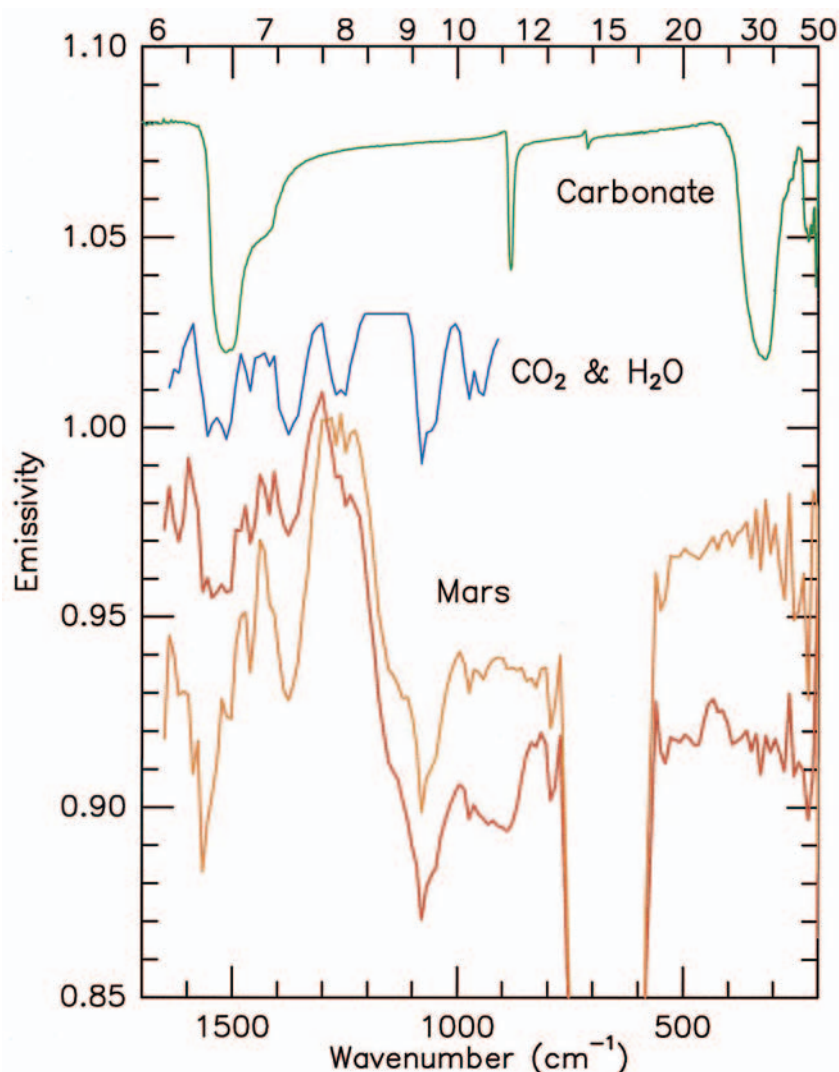


Plate 11. Two characteristic TES spectra compared with laboratory spectrum of calcite. Syrtis Major region is shown in orange; Arabia is shown in red. Carbonate and atmospheric component curves have been offset for clarity. Once the effects of atmospheric water vapor and water ice are removed, there is no positive evidence for a carbonate component in the TES spectra.

sumably rare, units can be detected somewhere on the planet. Thus either carbonates are less common than aqueous hematite or the processes by which they remain “hidden” are more efficient.

The lack of a detectable carbonate component does not preclude the existence of carbonate in minor (<5–10%) occurrences or in localized, favorable environments. Detailed examination of the ~75 million TES spectra, or data from future high spatial resolution IR [Christensen *et al.*, 1999] and near-IR instruments, may reveal small occurrences not observed at TES resolution.

Sulfates have a fundamental vibrational feature near 1150 cm^{-1} (e.g., 1145 cm^{-1} for gypsum; Figure 7). This feature is not observed in dark region, atmosphere-removed surface spectra, and sulfates have not been detected with any confidence in deconvolution modeling [Christensen *et al.*, 2000b; Bandfield *et al.*, 2000a]. A spectral inflection is present in the derived atmospheric dust spectrum [Bandfield *et al.*, 2000b; Smith *et al.*, 2000a] whose position is consistent with sulfate. This observation is consistent with previous indications of sulfate from

Earth-based telescopic near-IR spectra [Blaney and McCord, 1995]. However, the relative depth of this feature does not vary with location, leading to the assumption that it is an atmospheric component [Bandfield *et al.*, 2000b; Smith *et al.*, 2000a]. If this is the case, then this feature does not pertain directly to the question of the nature of sulfur identified in lander observations [Clark and Baird, 1979; Reider *et al.*, 1997; McSween *et al.*, 1999; Morris *et al.*, 2000; Bell *et al.*, 2000]. If this feature is present in the surface materials, then the lack of spatial variation in its depth implies that the abundance of sulfate is uniform everywhere on the planet. This implication does not appear to be plausible on the basis of the geologic evidence for widespread variation in surface processes. We therefore conclude, on the basis of the current TES evidence, that sulfates have not been positively detected in the surface materials above a detection limit of ~10–15%.

The “White Rock” feature on Mars (at ~8°S, 335°W) has long been viewed as a type example for a Martian playa largely owing to its apparent high albedo along with its location in a closed impact crater basin. A playa deposit has been postulated

to host abundant sulfates and some carbonates, so White Rock was an important target for the TES investigation. A thorough analysis of this feature has been performed using albedo, thermal inertia, and spectral data from TES as well as high-resolution images from the Mars Orbiter Camera [Ruff *et al.*, 2001]. These data demonstrate that White Rock is not anomalously bright relative to other Martian bright regions, reducing the significance of its albedo and weakening the analogy to terrestrial playas. Its thermal inertia value indicates that it is not mantled by a layer of loose dust, nor is it bedrock. The thermal infrared spectrum of White Rock shows no obvious features of carbonates or sulfates and is, in fact, spectrally flat. Halite, a major evaporite playa mineral, has a flat spectrum and so cannot be ruled out as a constituent of White Rock, nor can small amounts (less than ~10%) of carbonates and sulfates. One explanation for the origin of White Rock consistent with the observations is that it is an eroded accumulation of compacted or weakly cemented aeolian sediment.

5.3.5. Surface weathering. The TES data have shown that unweathered minerals, pyroxene and plagioclase feldspar, make up 85–100% of the surface materials in the dark regions that cover approximately half the planet [Christensen *et al.*, 2000b; Bandfield *et al.*, 2000a]. Relatively minor (0–15%) abundances of sheet silicates or other chemical weathering products could be present near the current detection limits in the TES data. Visible/near-IR data also indicate the occurrence of unweathered pyroxene minerals on the surface [e.g., McCord *et al.*, 1978; Singer *et al.*, 1979; Singer, 1980, 1982; Erard *et al.*, 1990; Mustard *et al.*, 1990, 1993, 1997; Mustard and Sunshine, 1995]. The surfaces of dark regions on Mars clearly show a red color, indicating the presence of alteration products [Bell, 1996]. However, these coatings must be thin (less than ~50–100 μm [e.g., Christensen and Harrison, 1993; J. R. Johnson *et al.*, Dust coatings on basalt and implications for thermal infrared spectroscopy of Mars, submitted to *Journal of Geophysical Research*, 2001]) to permit the TES IR spectra to see through them and sample the mineral grains underneath. Analysis of Viking multispectral data has shown that the darkest rocks are consistent with unoxidized basaltic andesite with minor (<30-nm) coatings of palagonite, although this match is not unique [Adams *et al.*, 1986; Guinness *et al.*, 1987, 1997]. McSween *et al.* [1999] favor a model in which the observed trends in visible/near-IR spectra of the rocks at the Pathfinder site are produced by varying amounts of relatively thin surface coatings.

We therefore conclude that while weathering and coating of rocks has occurred, it has produced relatively minor amounts of weathering products and that unweathered materials are present at the surface in significant (>85%) abundance in dark, dust-free regions.

It is important to note that all of the three Mars landings have occurred in relatively bright regions. The albedos of the Viking 1, Viking 2, and Pathfinder sites are 0.27, 0.25, and 0.22, respectively [Pleskot and Miner, 1981], whereas the albedo of typical dark regions is <0.15 [Pleskot and Miner, 1981]. Therefore it is likely that the surface rocks and sands in the dark regions are less coated by bright dust than those seen at any site visited to date. It has been suggested that Mars dark regions are likely areas of active removal of bright dust by sand saltation or other means [Thomas, 1984; Christensen, 1988]. Landing sites in dark regions might provide an opportunity to directly sample exposed, dust-free rocks [Edgett *et al.*, 1994].

In summary, the Viking, Pathfinder, visible/near-IR, and

TES IR results show that unweathered materials dominate the dark regions on Mars. The large extent of dark regions, together with the occurrence of unweathered rocks in the bright, dust-mantled region sampled by Pathfinder, argues against extensive, globally pervasive chemical weathering of materials now exposed at the surface of Mars. These results argue for a geologic history dominated by a cold, dry climate in which mechanical weathering was the dominant form of erosion. It appears likely that mechanical, rather than chemical, weathering has produced the bulk of Martian sediments.

6. Surface Physical Properties

6.1. Thermal Inertia

In addition to emissivity variations, the emitted energy is also a function of the temperature and physical properties of the surface. Thus such properties as particle size, rock abundance, subsurface layering, albedo, and packing affect the spectral and diurnal character of the outgoing energy. One of the objectives of the MGS TES instrument is the derivation of thermal inertia of the surface at ~3-km spatial resolution. Thermal inertia is the primary factor controlling the amplitude of the diurnal variation of surface temperature and is most closely related to the thermal conductivity of the surface materials. It depends primarily on the average particle size of the grains comprising the surface, the size and abundance of rocks on and near the surface, and the degree of induration of duricrust. As such, it provides remote information on the physical properties of the surface, especially at the decimeter to meter scales that are affected by geological and geochemical processes.

TES nighttime temperature measurements (Plate 12), together with TES daytime albedo measurements (section 6.2; Plate 14), provide the basis for determining thermal inertia [Kieffer *et al.*, 1977]. The thermal inertia observations obtained by TES provide a factor of 40 improvement in spatial resolution (and thus a factor of 1600 improvement in areal resolution) over the global Viking IRTM measurements [Palluconi and Kieffer, 1981; Haberle and Jakosky, 1991]. Preliminary results for data obtained from the science-phasing orbit at coarse resolution and their comparison with Viking results were presented by Jakosky *et al.* [2000]. Initial global results from the mapping orbit, including a global map and selected examples of high-resolution analysis, were discussed by Mellon *et al.* [2000], and more detailed analysis of regions of exobiological relevance are described by Jakosky and Mellon [this issue]. Major results and selected examples are summarized here.

The global map discussed by Mellon *et al.* [2000] was obtained by binning thermal inertia values derived from the first 6 months of the mapping mission to a spatial resolution of $1/4^\circ$ in latitude and longitude, roughly 15 km at the equator. The map shows the same large, continent-like regions of low thermal inertia as were seen by Viking, most likely corresponding to deposits of loose, unconsolidated air fall dust. In addition, regions having the highest thermal inertia values are seen to correspond to the floors of low-lying topographic features such as the catastrophic outflow channels, Valles Marineris, and large impact craters in the southern hemisphere [Zimbelman and Kieffer, 1979; Christensen and Kieffer, 1979; Edgett and Christensen, 1991].

The different surface types can be seen in Figure 8, which shows a cross plot of the TES-derived bolometric albedo versus the thermal inertia. The major modes of low inertia/high al-

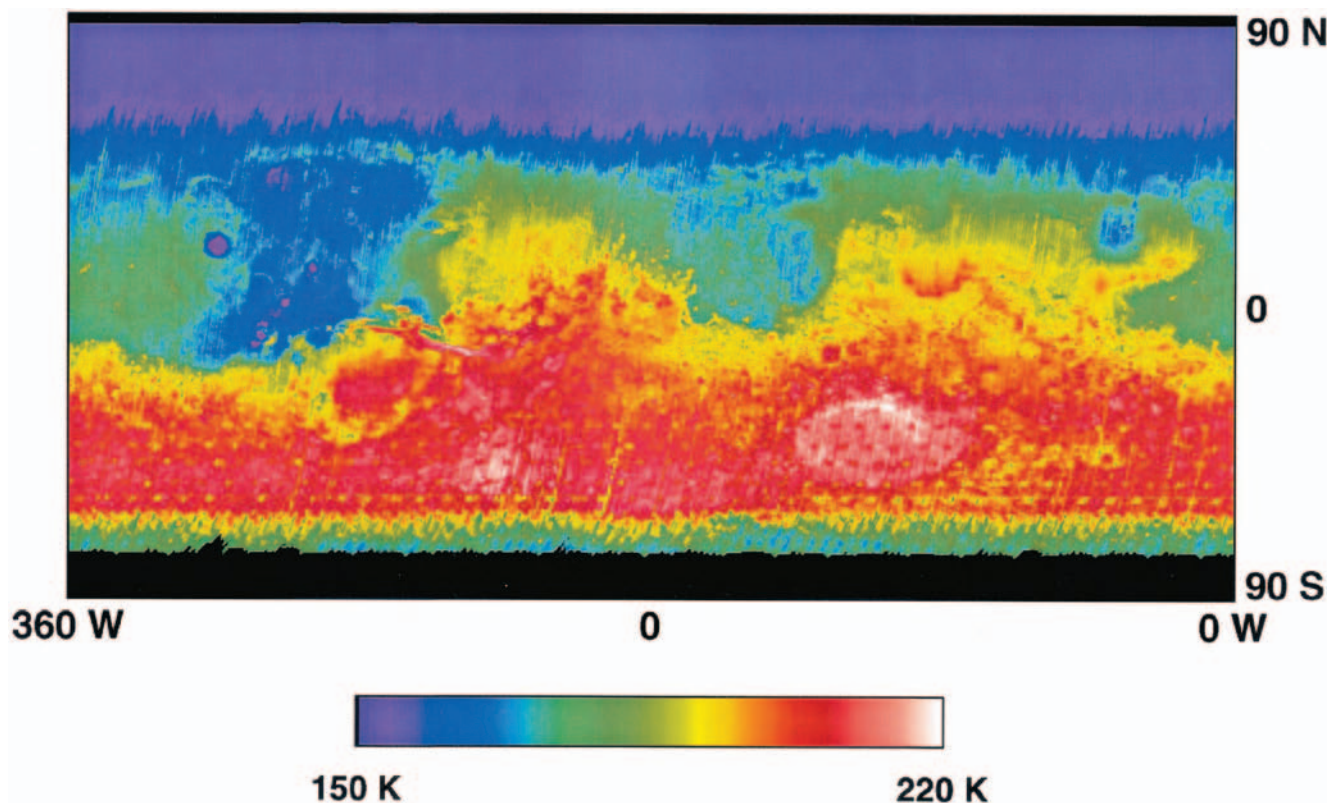


Plate 12. Global nighttime temperature map in cylindrical projection. Higher temperatures represent larger soil grains or higher abundance of rocks on the surface. There is a small effect of increasing atmospheric pressure toward low elevations.

bedo (dusty areas) and high inertia/low albedo are clearly apparent. In addition, there is a third mode, corresponding to intermediate values of both thermal inertia and albedo. This third mode surrounds the low-inertia regions geographically yet does not appear to be transitional between the other two modes. One possibility is that it is a region consisting of well-indurated duricrust [Jakosky and Christensen, 1986; Presley and Arvidson, 1988; Christensen and Moore, 1992].

Substantially higher thermal inertias are seen in Figure 8 at values up to twice that of the high-inertia modal values (note that values $>800 \text{ J m}^{-2} \text{ K}^{-1} \text{ s}^{-1/2}$ are not well determined by our current algorithms). These materials do not appear to be just the high-inertia tail of the mode, as they cluster together geographically in low-lying areas. Rather, they appear to represent a different mechanism of evolution of the surface, possibly involving a combination of aeolian and aqueous processes or possibly exposed outcrops of bedrock.

Plate 13 shows several examples of the high-resolution maps that have been obtained from TES data [Mellon *et al.*, 2000]. The coverage is that from the first 6 months of mapping; data obtained later in the mission will fill in the gores in the maps substantially.

Plate 13a shows the Pettit wind streak (located near latitude 12°N , longitude 174°W). The dark intracrater deposit has a peak thermal inertia of 375, and the streak extending to the southwest for 250 km has values between about 240 and 170. These values show up as distinct from the surrounding terrain, which has thermal inertia of 30–80. These values are most consistent with a particle size of windblown material within the

crater of $\sim 800 \mu\text{m}$ [Presley and Christensen, 1997], possibly decreasing in size downwind in the streak [Mellon *et al.*, 2000].

Plate 13b is the eastern section of Coprates Chasma in Valles Marineris (14°S , 59°W). Thermal inertia within the canyon is in the range of 500–800, while that of the surrounding terrain is about 200–300. These values are among the highest measured on Mars and are consistent with a very rocky, blocky, or crusty surface, basically devoid of substantial deposits of wind-deposited dust [Mellon *et al.*, 2000].

Plate 13c is a large section of Kasei Valles (near 25°N , 66°W), one of the largest of the catastrophic flood channels that emanate from Valles Marineris region. The correlation between the thermal inertia and the channels, channel cut walls and islands, and other flow features is striking. In addition, a clear gradation of thermal inertia is observed, increasing in the downstream direction. This pattern could be explained by the original channel-forming events, involving stripping of the fine material by the water leaving the rocks behind; it also could be the result of subsequent aeolian reworking, with wind-blown dust being carried and deposited preferentially within the confines of the channel [Mellon *et al.*, 2000].

We anticipate that the detailed analysis of maps such as those presented in Plate 13, especially in conjunction with the regional context provided by the global coverage, will help us to understand the processes that have affected the surface. In particular, they provide the best global information on the deposition, removal, and reworking of materials in the top meter of the surface. Importantly, they also provide information at a spatial scale that is important for the successful op-

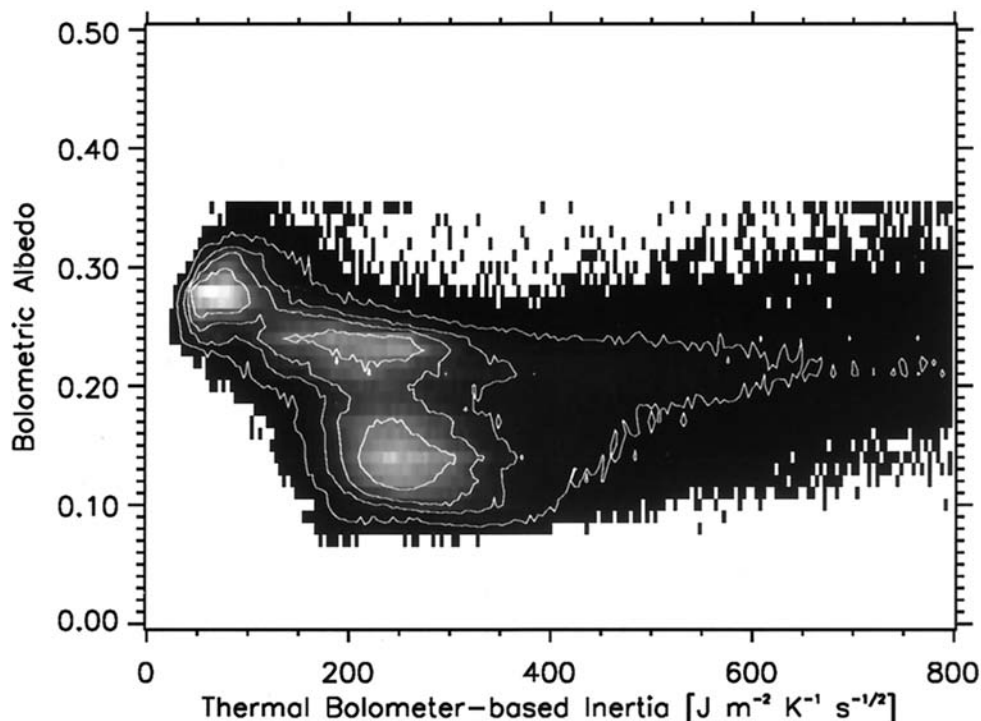


Figure 8. TES-derived thermal inertia versus albedo. Note the major modes of low inertia/high albedo and high inertia/low albedo. A third mode, corresponding to intermediate values of both thermal inertia and albedo, is also apparent. Some regions on Mars exceed the current model limits of albedo of 0.35 and inertia of $800 \text{ J m}^{-2} \text{ K}^{-1} \text{ s}^{-1/2}$. Data are from *Mellon et al.* [2000].

eration of lander and rover vehicles and for selection of sites where sampling of both weathered and unweathered materials can take place.

6.2. Visible/Near-Infrared Albedo

The TES has obtained global bolometric visible/near-IR albedo observations of the surface, suspended dust, and polar materials [Kieffer *et al.*, 2000; P. R. Christensen, manuscript in preparation, 2001]. These measurements are used to investigate the nature of the surface materials, to investigate changes in the upper surface due to the redistribution of mobile fines, as inputs to the derivation of thermal inertia, and in making an internally consistent determination of the total polar energy balance. In addition, they have been used to investigate the surface phase function using variable emission angle measurements, atmospheric dust scattering properties [Smith *et al.*, 2000b], and polar cap dust contaminants [Kieffer *et al.*, 2000].

TES albedo measurements have shown that significant changes in surface markings have occurred since the measurements obtained by the IRTM over 20 years ago. These changes are consistent with those observed by the Hubble Space Telescope [e.g., Bell *et al.*, 1997]. Plate 14 shows the visible/near-infrared (0.3- to $2.9\text{-}\mu\text{m}$) reflectance determined by the TES for the period from L_s 100°–150° in the north (90°N to 10°S) and 270° to 330° in the south. These periods were selected to minimize the effect of atmospheric clouds and dust [Smith *et al.*, this issue; P. R. Christensen, manuscript in preparation, 2001] and provide the best available estimate of the broadband reflectance of the Martian surface. Future work will address the complete separation of atmospheric contributions.

7. Polar Properties

The two volatiles that play important roles in Mars climate and evolution are CO_2 , as the major agent for transport and storage of energy, and H_2O , as a major geomorphic agent. Models of the physical properties, surface-atmosphere exchange, and seasonal behavior of these volatiles have been developed that agree with the general features of existing observations and allow some extrapolation into the past [e.g., Davies *et al.*, 1977; Kieffer, 1979; James and North, 1982; Haberle and Jakosky, 1990; Kieffer, 1990; Kieffer and Zent, 1992]. However, there are significant deviations of these models from observations localized in time and space. Several geophysical processes of potential importance have been ignored in most existing models, e.g., the incorporation of dust and water ice into the seasonal polar caps, the influence of suspended aerosols on the radiation balance over the winter cap [see Paige and Ingersoll, 1985], and the processes which cause the major polar outliers.

The TES has addressed these and a variety of other polar cap processes using moderate spectral and spatial resolution observations. Specific studies have addressed the following key questions: (1) What are the composition, physical properties, and spatial and seasonal variation of polar condensates? (2) What is the energy balance in the cap-atmosphere system? (3) What is the role of dust in influencing the surface frost albedo? (4) What is the abundance and variability of atmospheric dust over the polar caps?

Because periapsis of the aerobraking elliptical orbit was far north, observations made during the Orbit Insertion period

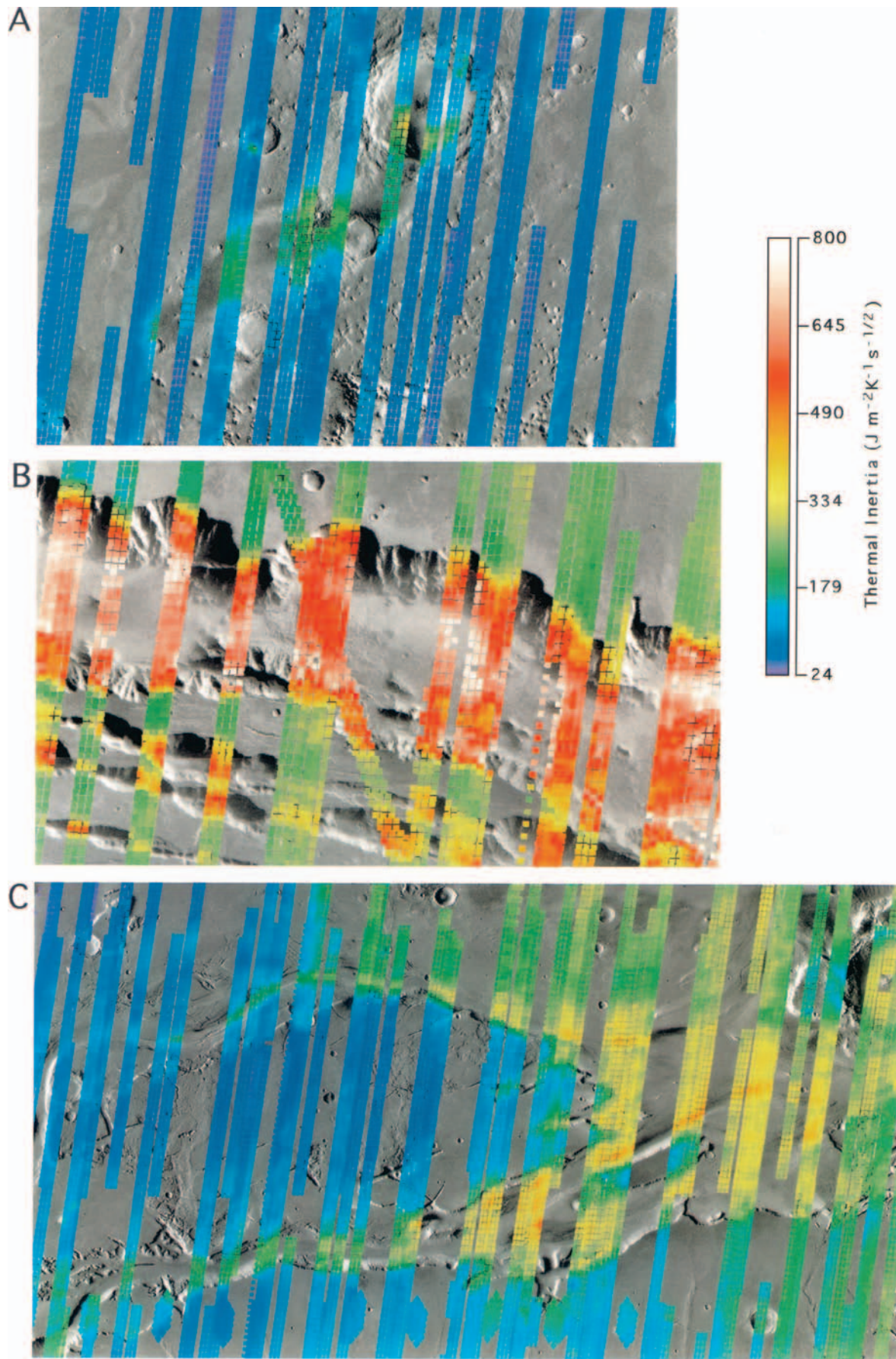


Plate 13. High-resolution maps of thermal inertia for selected regions: (a) Pettit wind streak, (b) eastern Coprates Canyon, and (c) Kasei Valles. Each rectangle corresponds to the intrinsic 3-km resolution of the TES. North is toward the top in all cases. Data are from *Mellon et al.* [2000].

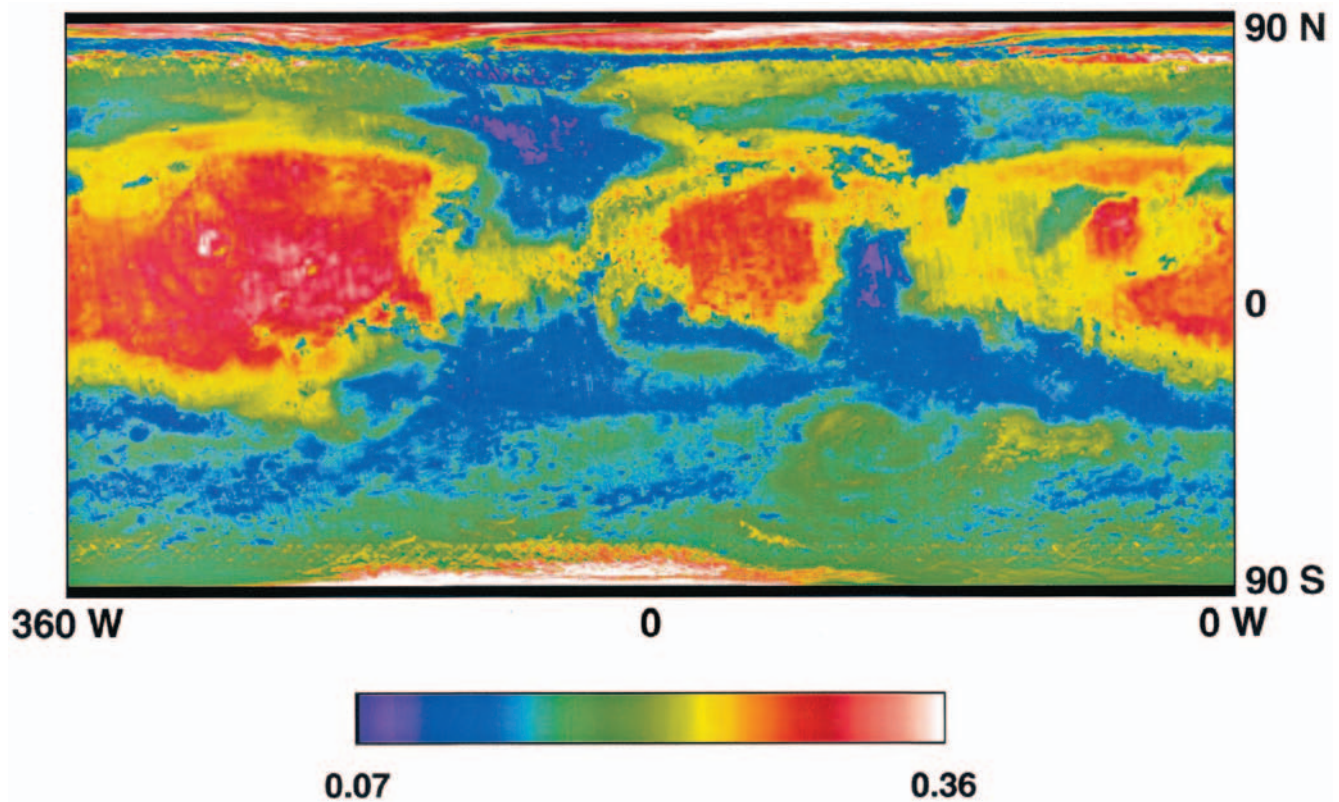


Plate 14. Global visible/near-infrared reflectance map in cylindrical projection. The TES bolometer measures the fraction of solar energy that is reflected from 0.3 to 2.9 μm .

provided quite different styles of coverage for the two polar regions at opposing seasons. The north polar region was observed during fall and winter with high-resolution nadir track “noodles,” while the south polar cap was observed in the spring and summer with regional mapping coverage as described in section 3.2 (Plate 3).

7.1. Condensation Season in the North

Thermal spectra of the winter polar cap exhibit dramatic variation in the 25- μm region associated with the “transparency” band of solid CO_2 . Principal component analysis of representative data indicates that there are three primary forms of condensing CO_2 : fine-grained crystals with a broad low spectral emissivity at 25 μm (the “U” member), coarser-grained crystals with a somewhat weaker and sharper emissivity depression (the “V” member), and slab ice with a spectrum close to a blackbody (the “B” member) [Titus *et al.*, 2001].

The U member is responsible for the common winter “cold spots” with 25- μm brightness temperatures far below the expected saturation temperature of CO_2 that had proved puzzling since their first discovery [Kieffer *et al.*, 1976, 1977]. Although 25- μm brightness temperatures as low as 110 K have been observed by TES, the kinetic temperatures implied by measurements at 18 μm , where CO_2 -solid emissivity is close to unity, and in the 15- μm gas band imply that most of the cold spots result from fine-grained CO_2 on the surface and a small proportion from CO_2 clouds. The cold spots are commonly associated with local topography, with some locations matching those observed 25 years earlier. Repeat coverage provided by crossing nadir tracks has shown that cold spots can form and disappear with a timescale of a few days. In at least one case,

simultaneous observations by TES and MOLA indicate that a cold spot was due to high-altitude CO_2 precipitation, a “snow-storm” in progress [Titus *et al.*, 2001].

The initial form of CO_2 at the expanding edge of the seasonal cap is slab ice, and this form dominates the outer portion of the cap all winter and persists until the Sun has risen several degrees in the spring [Titus *et al.*, 2001].

7.2. Sublimation Season in the South

Monitoring the growth and retreat over 1.5 Mars years (e.g., Plate 15) shows that the edge of the seasonal cap appears at different locations in emitted versus reflected radiation; early in the retreat the thermal cap is the larger; in late phases the visual cap is larger [Kieffer *et al.*, 2000]. While the radiometric properties of the receding cap are neither uniform nor constant, the major distribution of radiometric behavior is similar to that observed 25 years ago by Viking; the southern cap retreat mapped by MGS lagged that observed by Viking in 1977 by less than $\sim 2^\circ$ of L_s .

No definite evidence of H_2O has been found in the south seasonal cap, and little evidence of H_2O was found in the atmosphere above the receding cap [Kieffer *et al.*, 2000]. One particularly interesting section of the seasonal cap (termed the “Cryptic region”) remains cold with low albedo for an extended period; the region is probably covered with a slab of solid CO_2 ice [Kieffer *et al.*, 2000]. The surface of the Cryptic region absorbs up to 50 W m^{-2} more than at the perennial cap or the frost-covered Mountains of Mitchel. The visual cap retreat “halts” at the poleward edge of the Cryptic region for nearly 20° of L_s . The transition from complete to negligible frost coverage at a 60-km scale takes place over ~ 20 sols.

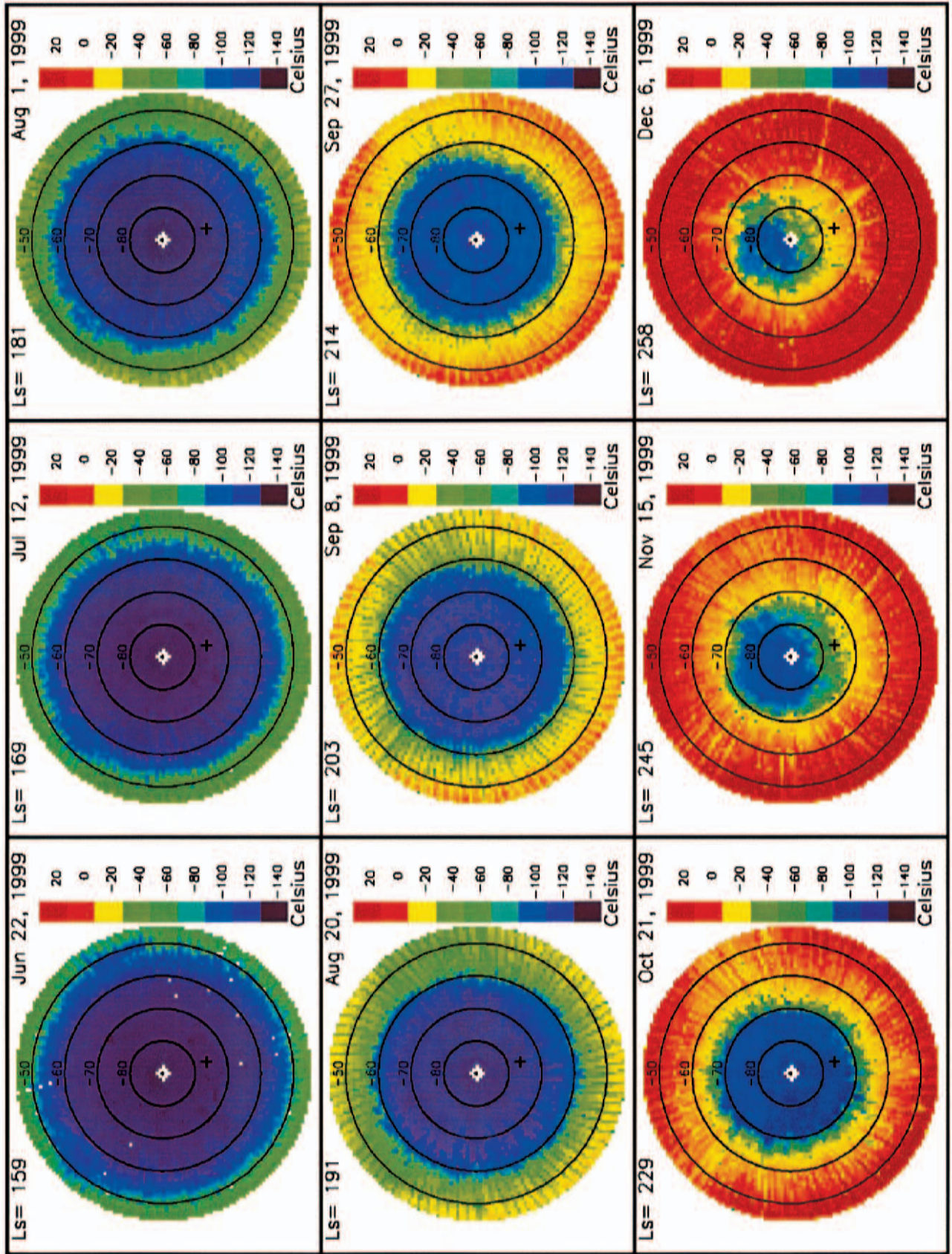


Plate 15. South polar cap regression. Measurements of surface temperature derived from TES spectra.

At low Sun angles (less than $\sim 10^\circ$ above the horizon) the seasonal cap has low reflectivity; as spring progresses the cap brightens in most locations, and three regions reached albedos >0.6 [Kieffer *et al.*, 2000]. Simultaneous observations of bolometric albedo and infrared spectra indicate that the primary cause of the variable albedo is variation of grain size of solid CO_2 . At some times and places the effective scattering length in solid CO_2 is indeterminately large, certainly centimeters and possibly of the order of 1 m, with the soil surface sensed through up to 1000 kg m^{-2} of solid CO_2 at both solar and $25\text{-}\mu\text{m}$ wavelengths [Kieffer *et al.*, 2000]. The CO_2 forming in the early cap condensation phase appears not to be fine grained and may be a slab. Although CO_2 grain size may be the major difference between these regions, incorporated dust is also required to match the observations. It appears that the lofting of dust grains by the net sublimation wind partially controls the seasonal cap albedo during sublimation.

There are no regional geologic correlations with the Cryptic region. Its origin may involve consistent wind patterns driven by topography that influence the microphysics of the CO_2 condensation process and affect the frost grain size, causing larger grain sizes to occur in the Cryptic region [Kieffer *et al.*, 2000]. The CO_2 grain size, in turn, controls the albedo of the deposit and its ability to persist in the spring. Because of the greater heat flux into the surface in the Cryptic region in the spring/summer, more CO_2 must have accumulated there, implying a greater effective emissivity during the winter. All of this is consistent with slab CO_2 formation in the Cryptic region in the southern winter.

There is some correlation of seasonal cap behavior with topography but no universal rule: chasmata interrupt the Cryptic region, and some generally bright parts of the cap (perennial and the Mountains of Mitchel) are at high elevation, but another commonly bright area has a lower elevation than the Cryptic region [Kieffer *et al.*, 2000].

Regional atmospheric dust is common in the polar region. Localized dust clouds, with an extent of a few hundred kilometers, are observed near the edge of the cap prior to the onset of a regional dust storm and interior to the cap during the storm [Kieffer *et al.*, 2000].

8. Summary and Conclusions

Returning to our set of key composition questions (section 5.1), the TES contributions to date can be summarized as follows:

1. The mineralogy of volcanic materials varies from basaltic, composed of plagioclase feldspar, clinopyroxene, \pm olivine, and \pm sheet silicates, to andesitic, dominated by plagioclase feldspar and high-silica volcanic glass. The basalts occur primarily in the ancient, southern hemisphere highlands, and the andesites occur primarily in the younger northern plains. The spectra from dark regions closely match both the spectral shape and contrast of particulate samples of terrestrial rocks. No unusual particle size or other environmental effects are observed, nor are required, to account for the spectra observed for Mars.

2. Aqueous mineralization has occurred in limited regions under ambient or hydrothermal conditions. Gray, crystalline hematite is found in three unique locations that are interpreted to be in-place sedimentary rock formations. These units provide evidence for the long-term stability of liquid water near the surface of Mars.

3. No evidence for carbonates has been found. Arguments can be made for the failure to detect these materials, but we can conclude that large-scale (tens of kilometers), coarse-grained ($>50\text{-}\mu\text{m}$) deposits of greater than $\sim 10\%$ carbonates are not currently exposed at the Martian surface. This lack of detection is consistent with models for early Mars in which large volumes of carbonates never formed.

4. Unweathered volcanic minerals (pyroxene, feldspar, and minor olivine) dominate the spectral properties of Martian dark regions. Conversely, no evidence has been found for weathering products above the TES detection limit. This lack of evidence for chemical weathering of the Martian surface indicates a geologic history dominated by a cold, dry climate in which mechanical weathering was the dominant form of erosion.

5. No conclusive evidence for sulfate minerals has been found at a detection limit of $\sim 15\%$.

6. SNC meteorites cannot be directly matched to the spectral properties of any regional volcanic unit.

7. The composition of "White Rock" appears to match that of typical Martian dust. Many other unique surfaces remain to be investigated.

- 8–10. The composition and origin of Martian dust has not yet been addressed in detail and remains an open question, as does the composition of sedimentary materials in channels and deposits and the composition of the polar layered deposits.

The key polar conclusions reached to date include:

1. CO_2 condensation occurs in three forms, fine-grained, coarse-grained, and slab ice; the form can change in a few days. Most condensation occurs at the surface, not in the atmosphere. Slab ice is the prevalent form in the outer regions of the forming cap and persists until shortly after seasonal sunrise.

2. The interiors of the seasonal caps are characterized by spatially nonuniform behavior, with several small, unique regions. Comparisons with Viking observations indicate little difference in the seasonal cycle 12 Martian years later. The observed radiation balance indicates CO_2 sublimation budgets of up to 1250 kg m^{-2} .

3. For most of the seasonal cap, while kinetic temperatures remain near the CO_2 frost point, albedos increase slowly with the rise of the Sun, then drop rapidly as the frost becomes patchy and disappears over a period of ~ 20 days.

4. A "Cryptic" region in the south cap remains dark and mottled throughout its cold period. TES spectra indicate that the Cryptic region has much larger grained solid CO_2 than the rest of the cap and that the solid CO_2 here may be in the form of a slab. Although CO_2 grain size may be the major difference between different regions, incorporated dust is also required to match the observations.

5. The Mountains of Mitchel remain cold and bright well after other areas at comparable latitude, apparently as a result of unusually small size of the CO_2 frost grains.

6. There is little evidence for a significant presence of H_2O in the south.

7. Regional atmospheric dust is common; localized dust clouds are seen near the edge of the cap prior to the onset of a regional dust storm and interior to the cap during the storm.

The key surface physical property results include the following:

1. A third inertia-albedo mode, corresponding to intermediate inertia and albedo values, has been identified using high-resolution albedo and temperature TES data. This distinct unit

is separate from the low-inertia/bright regions and high-inertia/dark regions discovered previously. It may consist of a bonded, duricrust unit.

2. Localized regions of high inertia ($\geq 800 \text{ J m}^{-2} \text{ K}^{-1} \text{ s}^{-1/2}$) are identified in TES data. These low-lying surfaces, e.g., channel and crater floors, may have formed by a combination of aeolian, fluvial, and erosional processes or may be exposed bedrock.

Appendix A: Electronics Design

A1. Analog Signal Processing

The TES includes discrete analog signal processing chains for each of the three TES detector arrays; the analog signal chains include both preamplifier and postamplifier electronics. These three signal chains are multiplexed along with the internal instrument telemetry and then converted to the TES digital signal on the Multiplexer and Analog to Digital Converter (MUX & A/D) electronic circuit card assembly. This circuit card also includes the preamplifier and postamplifier electronics for the TES counting interferometer's Fringe and Zero Path Difference (ZPD) photodiode detectors.

A1.1. Spectrometer channels. The TES analog electronics for the spectrometer channels include independent analog signal chains for each of the six spectrometer detector signals. The gains for each channel are adjusted to match the varying performance of each DTGS detector in the array. The signal chain consists of a preamplifier, postamplifiers, track and hold, and filtering for each detector. The track and hold electronics sample the input signal interferogram at $\sim 1 \text{ kHz}$ and are synchronized to the collection of the interferograms which are generated every 2 s.

The preamplifiers include a low-noise fixed-gain preamplifier (OP-421) and the current sources and biases for each detector signal. The spectrometer preamplifiers are hard wired to the spectrometer detector array and are enclosed in their own housing that is located near the detector array in the TES aft optics compartment.

The spectrometer postamplifiers include a differential front-end amplifier (LM108A), a fixed-gain detector frequency response "boost" amplifier (HA2700), three-pole Bessel filtering, four-level switchable analog gain (DG302A), two fixed-gain signal amplifiers (HA2700), synchronous track and hold (2N4393), and a "follower" amplifier buffer (LM108A) for each detector signal. The spectrometer postamplifier circuit card also includes power supply regulation from ± 15 to $\pm 12 \text{ V}$ to ensure adequate noise immunity.

A1.2. Visible and thermal bolometer channels. The visible and thermal bolometer analog electronics are identical except for gain values, with independent analog signal chains for each of the bolometer detector chopped signals. The gains for each channel are adjusted to match the varying performance of each DTGS detector in the array. The signal chain consists of a preamplifier, postamplifiers, demodulator, integrator, and filtering for each detector. The demodulation is synchronized to the 30-Hz chopped input signal, while the integration is performed on the demodulated signal for 1.7 s every 2 s.

The preamplifiers include a low-noise fixed-gain preamplifier (OP-421) and the current sources and biases for each detector signal. The visible bolometer preamplifiers are hard wired to the visible bolometer detector array and are enclosed in a housing (also housing the thermal bolometer preamplifi-

ers) that is located near the detector array in the TES aft optics compartment.

All bolometer postamplifiers include a differential front-end amplifier (LM108A), a fixed-gain detector frequency response boost amplifier (HA2700), single-pole filtering, two-level switchable analog gain (DG302A), fixed-gain signal amplifier (HA2700), synchronous demodulator (LM108A and 2N4393), synchronous integrator (2N4393), and a follower amplifier buffer (LM108A) for each detector signal. The visible bolometer postamplifier circuit card also includes power supply regulation from ± 15 to $\pm 12 \text{ V}$ to ensure adequate noise immunity.

A1.3. Analog multiplexing and analog to digital conversion. The TES analog multiplexing and analog to digital conversion electronics handle the flow of all analog data from the analog processing electronics and internal analog instrument telemetry to the digital processing electronics. These electronics multiplex and digitize the 18 analog signals from the three detector arrays, the 16 analog temperature telemetry channels from the discrete temperature sensors located throughout the TES, and the 20 analog voltage and current telemetry channels from the TES power supply. The six signals from the spectrometer postamplifier channels are read and processed continuously during the 1.8-s scan of each 2-s scan/retrace period. The 12 signals from the visible and thermal bolometer postamplifier channels and 36 analog telemetry channels are read once and processed during the 0.2-s retrace of each 2-s scan/retrace period.

These electronics consist of a series (5) of complementary metal-oxide semiconductor (CMOS) monolithic 8/1 analog multiplexers (HS1840RH), multiplexer address decoding logic (CD4xxx), low-noise low-offset follower amplifier (OP27), and a 16-bit hybrid analog to digital (A/D) converter (MN5290H/B). The analog multiplexing and analog to digital conversion circuit card also includes power supply regulation from ± 16 to $\pm 15 \text{ V}$ to ensure adequate noise immunity.

A1.4. Counting interferometer fringe and zero path difference detection. The TES counting interferometer fringe and zero path difference (ZPD) detection electronics are used to monitor the signals from the Fringe and ZPD silicon photodiode/preamplifier hybrids (EG&G HUV1100 and TL071) that are mounted on the TES counting interferometer assembly. These photodiodes measure the narrow-band (fringe) and pseudobroadband (ZPD) optical signals from the counting interferometer's neon lamp sources. The "zero crossings" from the resulting interference pattern return the fringe period timing, which is used to determine the position of the interferometer moving mirror assembly to better than $1/2$ wavelength of the neon lamp source (703.2 nm). The "peak" from the "broadband" interference pattern returns the ZPD timing, which indicates the center of the interferometer moving mirror's travel relative to the start of scan.

The detection electronics are colocated on the analog multiplexing and analog to digital conversion electronics circuit card. These electronics postamplify the signals from the photodiodes, generate the fringe digital timing signals, determine the position of the interferometer's ZPD relative to the start of scan, and pass this information to the TES timing sequencer and control electronics.

The fringe detection electronics include a differential front-end amplifier (LM108A), a fixed-gain low-pass filter and amplifier (HA2700), Zener limiter stage and fixed-gain amplifier

(1N4150, 1N4618, HA2700), output clamping diode, comparator (LM139), and a digital inverter (CD4049).

The ZPD detection electronics include a differential front-end amplifier (LM108A), two-level switchable analog gain (DG302A), a fixed-gain amplifier (HA2700), A/D reference level source (LM113, LM108A, 2N2222A), signal and reference level diode clamping (1N5711), 8-bit analog to digital converter (MP7683XTD), and digital ZPD decoding logic (CD4xxx and 54HC).

A2. Timing Sequencing

The TES timing sequencing electronics generate the timing waveforms necessary to control and synchronize instrument operation. The electronics generate pulses that control and synchronize the amplification, track/hold, demodulation, integration, multiplexing, analog to digital conversion, and data buffering of all of the analog signals. They also control and synchronize the chopper, interferometer, and pointing mirror servo electronics with the data acquisitions.

All pulses in the timing sequencer are generated from the master clock crystal oscillator, which operates at a frequency of 14.5152 MHz. The 7256-kHz digital signal processor clock, 4838-kHz divider clock, 3628-kHz bus interface unit clock, 1209-kHz interferometer, and 201-kHz power supply switcher clocks are generated by master clock divider logic (HC54). The divider clock is used by additional divider logic (HC54) to generate various system clocks (7680, 3840, 1920, and 30 Hz) that are required for other timing sequencer functions. The control signals that control and synchronize the TES data acquisitions, data processing, and data flow are stored in the timing microprogram sequencer. This microprogram is stored in four program PROMs (HM9_6617), and the timing signals are accessed using system clocks and some additional counter and address logic (HC54). The timing sequencer electronics use the spacecraft's Payload Data Subsystem (PDS) generated Real Time Interrupt (RTI) clock to synchronize all TES data transfers and commanding with the PDS.

The timing sequencing electronics also include a fringe clock delay circuit that is attached to the main circuit card via a daughterboard. This board uses variable delay logic (HC54) to adjust for the timing propagation delay between the analog signal chain and the digital fringe signal chain.

A3. Digital Signal Processing

The TES digital signal processing electronics and the digital signal processor flight software take the raw interferogram data from each of the six spectrometer channels and transform them into spectra, which are then transferred to the command and control processor for further processing and formatting. The digital processing electronics and flight software perform the following tasks: gain setting, data collection, ZPD correction, offset adjustment, peak detection, interferogram folding, fast Fourier transformation, magnitude computation, temporal integration, gain correction, and equalization during each 2-s spectrometer data acquisition.

The digital signal processing electronics utilize a space-qualified Texas Instruments TMS320C25 digital signal processor clocked at 7256 kHz. This microprocessor is an implementation of the Harvard architecture and uses separate program and data memory spaces. The DSP program memory consists of 32 kb of PROM (HM_6617) and 64 kb of static CMOS RAM (HC6364) which are resident on the circuit card and

accessed using address logic (HC54). The DSP data memory consists of two banks of 64 kb of static CMOS RAM.

The digital signal processing electronics also include a DSP latch-up protection circuit that is attached to the main circuit card via a daughterboard. This circuit protects the digital signal processing electronics from overcurrent damage that could result from a DSP latch-up event.

A4. Command and Control Processor

The TES command and control processor electronics and the command processor flight software oversee and control all tasks in the TES instrument. The command and control electronics and flight software control the following tasks: task supervision, sequencing, data acquisition, data editing, data compression, DSP control, command interpreter, servo control, error checking, and BIU control when the TES is powered on. All TES data acquisition sequencing and data downlink are controlled by the command and control processor electronics and are initiated by default PROM sequences or ground commands.

The command and control processor electronics utilize a space-qualified Harris CMOS 80C86 microprocessor clocked at 4838 kHz. This microprocessor uses separate program and data memory spaces. The command and control program memory consists of 64 kb of PROM (HM_6617) which are resident on the command and control circuit card assembly and accessed using address logic (HC54). The command and control processor PROM contains all of the programs necessary to run the TES from a cold start reboot in its default data acquisition mode. After power-up all code and control tables are copied from PROM into the write-protected RAM and then executed out of RAM. The command and control program and data RAM are located in the same electronic module subassembly but on the command and control processor program and data memory circuit card assembly.

The TES command and control processing electronics communicate with the spacecraft via the JPL-supplied Bus Interface Unit (BIU), which in turn communicates with the spacecraft Payload Data Subsystem (PDS).

A5. Command and Control Processor Program and Data Memory

The TES command and control processor program and data memory is used to hold code copied from PROM, code uploaded from the ground, flight software stacks, and TES data. The bulk of the RAM is used for the output data buffer holding formatted packets that are ready to be sent to the BIU. The digital signal processor RAM areas are also mapped into the command and control processor memory space and may be accessed when the DSP is in hold mode.

The command and control processor program and data memory consist of 640 kb of static CMOS RAM (HC6364) which are resident on the circuit card and accessed using address logic (HC54). The static CMOS technology allows a large memory bank that consumes only the power required for the device that is being accessed.

A6. Servo Controllers

The TES servo controller electronics include the pointing mirror servo control electronics, the chopper servo control electronics, and the interferometer servo control electronics. These servo electronics are located on the servo controller circuit card assembly located in the TES electronic module

assembly. Each control circuit is wired to its associated actuator located outside the electronics module. All controllers receive timing signals from the timing sequencer electronics and control from the command and control processor electronics.

A6.1. Pointing mirror servo. The TES pointing mirror servo electronics control the movement of the TES rotary pointing mirror actuator. This mirror is driven by a direct drive Schaeffer Type I stepping motor with an 80/1 harmonic drive. The motor can be operated in a “microstepping” mode to allow smooth image motion compensation during the 1.8-s IFOV dwell time. The motor drive electronics receive “forward” and “reverse” pulses from the command and control processor electronics to move the mirror during data acquisitions. The position of the mirror is monitored using primary and redundant fine and coarse optical interrupters that are connected to the actuator shaft and the rotating mirror assembly. The pointing mirror servo electronics pass the information from these sensors to the command and control processor electronics to give feedback control to the flight software.

The drive electronics consist of an analog drive circuit that takes the command processor’s forward and reverse digital pulses and generates the pulses to move the actuator. This circuit uses various analog components (2N2222A) and directional pulse logic (CD4xxx) to generate the three phase analog drive signals.

The position-encoding electronics consist of various analog components (2N2222A) and pulse detection logic (CD4xxx) to generate the digital pulses that are relayed to the command and control processor electronics.

A6.2. Chopper servo. The TES chopper servo electronics control the movement of the TES bolometer channel chopper actuator. The actuator is a low-power 30-Hz resonant single-blade tuning fork chopper. The chopper servo electronics control the amplitude of the chopper’s motion to within 0.325 inches when it is operating.

The control electronics consist of various analog components (2N2222A, 2N2907A, LM108A, LM139A) and drive logic (CD4xxx) that takes the 30-Hz clock from the timing sequencer and generates the signals that control the drive circuit. The circuit uses a chopper sense line from the actuator to perform feedback control. The servo electronics also return chopper lock telemetry to the command and control processor electronics.

The drive electronics consist of an analog bridge drive circuit that uses the signals from the chopper servo control electronics to control the actuator movement. This bridge circuit uses various analog components (2N2222A, 2N2907A) to generate the positive and negative analog drive signals.

A6.3. Interferometer servo. The TES interferometer servo electronics control the movement of the TES interferometer moving mirror actuator. This mirror is driven by a direct drive Schaeffer linear motor with tachometer feedback. The motor can be operated in either single- (10-cm^{-1}) or double- (5-cm^{-1}) scan mode, selectable by the command and control processor electronics. The interferometer drive electronics receive scan timing clocks from the timing sequencer electronics and the fringe clock from the fringe detection electronics. These clocks are used to synchronize the mirror movement with the spectrometer data acquisitions. The moving mirror tachometer signal is returned to the interferometer control electronics to allow active feedback control of the actuator. The start of scan is monitored using primary and redundant

single- and double-scan optical interrupters that are connected to the moving mirror assembly.

The interferometer servo electronics consist of the servo control and drive electronics. The control electronics consist of the drive logic (54HC, DAC08) that uses the timing sequencer and fringe clocks from the timing sequencer and the signals from the start of scan interrupters along with the analog feedback circuitry (2N2222A, LM108A, LM124A, DG302A) that takes the signal from the actuator tachometer. These electronics generate the signals that control the servo drive circuit.

The drive electronics consist of an analog bridge drive circuit that uses the signals from the servo control electronics to control the actuator movement. This bridge circuit uses various analog components (2N2222A, 2N6849, 2N6796) to generate the positive and negative analog drive signals.

The interferometer servo control electronics also include power supply regulation from ± 12 to ± 10 V to ensure adequate noise immunity.

A7. Power Supply

The TES power supply electronics are a high efficiency power supply that generates and regulates the voltages for all TES analog and digital circuit card assemblies. These electronics consist of two switching power supplies running at 201 kHz: one for the TES electrical loads and one for the TES mechanical loads. The TES current ripple filter electronics module is connected directly to the spacecraft’s unregulated +28 VDC power bus. The current ripple filter electronics reduce the ripple that the TES actuators may put on the spacecraft power bus. It also filters the spacecraft power into the TES power supply electronics. The TES power supply primaries use the +26 and +28 VDC from the current ripple filter. The transformer secondary windings generate all of the output voltages needed to power the TES analog and digital circuit card assemblies.

Appendix B: Instrument Calibration

The TES instrument was calibrated and tested at SBRS prior to launch. The primary objectives of these tests were to determine (1) the field-of-view definition and coalignment of all three instrument subsections; (2) the out-of-field response for all three instrument subsections; (3) the spectrometer spectral line shape and spectral sample position; (4) the visible/near-IR and thermal bolometer relative spectral response; and (5) the spectrometer, visible/near-IR bolometer, and thermal bolometer radiometric calibration. In Appendix B we describe the details of (1) the TES calibration instrumentation and test overview; (2) the field-of-view results; (3) the spectrometer radiometric calibration, noise performance, and spectral line shape; and (4) the visible/near-IR and thermal bolometer radiometric calibration.

B1. Instrument and Test Fixture Overview

B1.1. Internal instrument temperature instrumentation. Sixteen internal temperature telemetry points are instrumented in the TES and can be transmitted upon ground command. The digitization of these telemetry points is typically $0.1\text{--}0.2^\circ\text{C}$ at an instrument temperature of 5°C [Christensen, 1999]. The sigmas for these telemetry points, determined for thermal vacuum conditions with the instrument at its nominal operating temperature ($\sim 9^\circ\text{C}$), are $<0.05^\circ\text{C}$ and are within the digitization levels.

Table B1. TES Thermal Vacuum Cycles

	Cycle 1	Cycle 2	Cycle 3	Cycle 4
Start date	3/2/96	3/19/96	5/6/96	5/14/96
Start time, LT	1620	1720	2146	1900
End date	3/9/96	3/23/96	5/11/96	5/26/96
End time	0036	1700	0930	0118
Mars simulation tests	marssim1–18 marssimb1–b13 marssim19–34	marssimd1–37	marssime3–47	marssime48–122
Actuator tests	acte10–35	acte39–75	acte81–108	acte111–117
Data tests	data1b4–12	data1b19		data1b26–data1f6

B1.2. Internal reference surface properties and instrumentation. The TES internal reference surface was formed with parallel groves machined with 45° inclined surfaces with a height of 1.52 mm and a spacing of 3.05 mm. The reference surface was machined from aluminum alloy 6061-T651 with a protective coating of black anodize. The surface was coated with “CAD-A-LAC black” paint to a thickness of 2.5 mil (0.0025 inch) and cured for 4 hours at 70°C. The internal reference surface was instrumented with three YSI thermistors (telemetry points TS5, TS6, and TS7) that were delivered from the manufacturer with a stated absolute accuracy of 2% in resistance corresponding to $\pm 0.2^\circ\text{C}$ for temperatures from 0° to +40°C and $\pm 0.4^\circ\text{C}$ from –40° to 0°C. These thermistors were imbedded in the underside of the reference surface at three locations [Christensen, 1999]. During the final stages of thermal vacuum testing at SBRS, two of these thermistors gave erroneous readings that deteriorated with time. Two replacement thermistors were installed on the top of the reference surface and rewired into the instrument telemetry.

Resistances from the reference surface thermistors are digitized through the TES telemetry and converted to temperature. The digitization of the resultant temperatures is 0.167°C at –16.6°C, 0.109°C at 1.1°C, and 0.097°C at 25°C [Christensen, 1999]. The temperature differences between the three reference surface temperature readings were determined during SBRS thermal vacuum tests to be $< 0.5^\circ\text{C}$ over the full range of operating temperatures. The in-flight calibration algorithm uses the average of these three temperatures.

B1.3. External target properties and instrumentation. The two calibration blackbodies used within the SBRS thermal vacuum chamber (BCU-1 and BCU-2) were identical: 7.25-inch diameter and 15° half-angle cones machined at ASU and assembled and painted with “CAD-A-LAC black” paint at SBRS. Each blackbody was instrumented with two pairs of platinum thermistors, with one pair placed near the apex of the cone and the second pair placed approximately halfway between the apex and the opening of the cone [Christensen, 1999]. These thermistors were calibrated prior to shipment from the manufacturer to an absolute accuracy of 0.1°C ($\pm 0.5\%$ resistance).

The digitization of the blackbody telemetry points varies from $\sim 0.01^\circ\text{C}$ at –190°C to 0.02° at 35°C [Christensen, 1999]. The means and sigmas of the front and back thermistors in the cold, “space” blackbody (BCU-1) and the hot, “planet” blackbody (BCU-2) were determined in vacuum for the seven target temperatures with the instrument temperature at 9°C. The temperature stability was within the digitization level over > 1

min time periods. The front and back temperatures agree to within 0.7°C for the space blackbody. The planet blackbody thermistors agree to within $\sim 0.25^\circ\text{C}$ for cold temperatures, increasing to 1.5°C for hot temperatures.

B1.4. Bench-level test overview. Bench-level testing of the TES instrument was performed in two phases. One phase consisted of piece-part and system-level testing of the spectral performance of each subsection. These tests were performed under ambient conditions. The second phase consisted of field-of-view and out-of-field tests conducted before and after vibration and thermal vacuum testing to determine and confirm the field of view and coalignment of the three instrument subsections.

B1.5. Thermal vacuum test overview. The TES was placed in thermal vacuum (TV) at SBRS on four occasions between March and May 1996. The first TV cycle from March 2 to 13 discovered a serious drop in the instrument response with decreasing temperature and experienced a failure of neon lamp 1 used in the visible counting interferometer. A second TV cycle was done from March 19 to 23 to troubleshoot possible causes. During this test and subsequent ambient testing it was confirmed that the beam splitter lost alignment at low temperatures ($< 10^\circ\text{C}$). Testing of a flight spare beam splitter determined that the problem was caused by the presence of a small bead of uralane between the beam splitter and the compensator. This bead contracted with decreasing temperature, causing a 2- to 5- μm tilt in the beam splitter. The beam splitter housing was redesigned to replace the uralane injection process with solid uralane tabs that were screwed into position, and a new housing was designed and fabricated. TV cycle 3 began on May 6 and was ended on May 11 when it was observed that two of the reference surface thermistors were failing. These thermistors were replaced, and the final TV cycle 4 occurred from May 14 to May 26, 1996. Table B1 gives a summary of the start and end time as well as the temperature transition tests and key functionality tests used in the four TV cycles.

Calibration data were collected at instrument set point temperatures of –20°, –10°, 0°, +10°, +20°, +30°, and +40°C. At each instrument temperature the target blackbody (BCU-2; planet view) was set to target temperatures of 130, 160, 200, 240, 270, 310, and 325 K, while the second blackbody (BCU-1; space view) was held at a temperature near 83 K [Christensen, 1999]. For each instrument-planet target state (a calibration test set) a series of observations was made to provide instrument calibration, performance, and operational baseline data. Visible bolometer calibrations were performed at each instru-

ment temperature viewing a calibrated external lamp through a chamber window. Data were also collected during all target and instrument temperature transitions to provide baseline data on the effects of changing instrument and scene temperature.

B2. Field of View

B2.1. Prelaunch measurements. Field-of-view characterization data were acquired using a precision collimator at SBRS. Thermal and visual sources were projected through a 1-mrad-wide, 40-mrad-long slit into the TES aperture [Christensen, 1999]. The TES was manually rotated to move the slit at 1-mrad spacing across the focal plane; 33 points were measured from -16 to $+16$ mrad in elevation, and 41 points were measured from -20 to $+20$ mrad in azimuth. The results from the final preshipment bench alignment tests (May 4, 1996) are shown in Figures B1 (azimuth) and B2 (elevation). The location of the half-power points are listed in Tables B2 and B3, and the field-of-view size is summarized in Table B4. Note that scanning the TES pointing mirror in the positive direction rotates the detector array in a clockwise direction projected against the limb as viewed from the TES.

After the TES was delivered to LMA, it was aligned on the spacecraft using the TES alignment cube for reference. The measured values for the prelaunch rotational offsets of the TES alignment cube relative to the spacecraft axes are given in Table B5 as rotations about the specified axis in a right-handed coordinate system.

B2.2. Two-dimensional spatial response. Knowledge of the two-dimensional spatial response within each field of view of the instrument is required for certain types of TES data analysis. Measurements taken near the limb of the planet are especially sensitive to the spatial response because of the rapid change of the spectral radiance as a function of the vertical distance of the tangent point of the ray path above the horizon. Two types of measurements have possible applications in the field-of-view response analysis; one set of measurements was taken prior to launch at SBRS, and the other consists of measurements from the spacecraft with Earth subfilling the fields of view. In this analysis the laboratory measurements are used as the primary data set; the Earth-viewing data are used for verification.

On November 24, 1996, the spacecraft was rotated to point the TES instrument at the Earth to acquire field-of-view measurements from a distance of 4.7 million km. The angular size of the Earth was 2.67 mrad, and it provided an excellent source for further characterization of the TES field of view. Unfortunately, only detectors 4, 5, and 6 observed the Earth. These data verify the shape of the field of view and confirm that there is no large out-of-field response. The normalized two-dimensional spatial responses for the TES detectors are given by Christensen [1999].

B2.3. Out-of-field response. Near-field out-of-field response was measured at the bench level using a 2.4-mrad square slit that was stepped in 2.4-mrad increments from -14.7 to $+14.7$ mrad in azimuth and -19.6 to $+19.6$ mrad in elevation [Christensen, 1999]. At each grid point, 5 ICKs were collected with the aperture open and 5 ICKs with the aperture blocked to correct for the background. No measurable out-of-field energy was observed. The far-out-of-field response was determined over an extended area using a 40×32 mrad slit that was stepped in increments of 32.7 mrad in azimuth and 40 mrad in elevation from -196 to $+196$ mrad in azimuth and

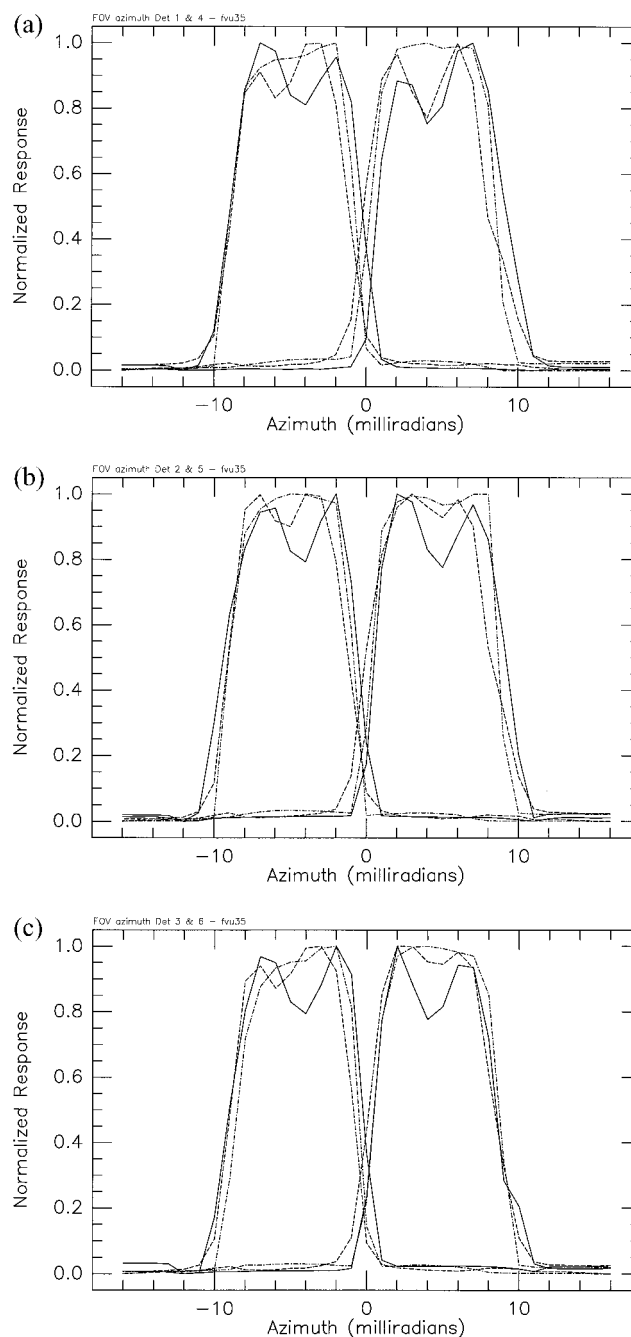


Figure B1. Prelaunch field-of-view definition and alignment in the azimuth direction. Detector response normalized to a 1 by 40 mrad slit. Visible/near-IR bolometer detectors, solid line; thermal bolometers, dashed line; spectrometer detectors, dot-dashed line. Central dip in all bolometer channels is due to obscuration by the detector electrode. (a) Detectors 1 and 4. (b) Detectors 2 and 5. (c) Detectors 3 and 6.

from -200 mrad to $+200$ mrad in elevation. At each grid point, 5 ICKs were collected with the aperture open and 5 ICKs with the aperture blocked to correct for the background. Again, no measurable out-of-field energy was detected.

B3. Spectrometer Radiometric Calibration

B3.1. Derivations. The TES instrument was radiometrically calibrated using thermal vacuum data acquired at SBRS

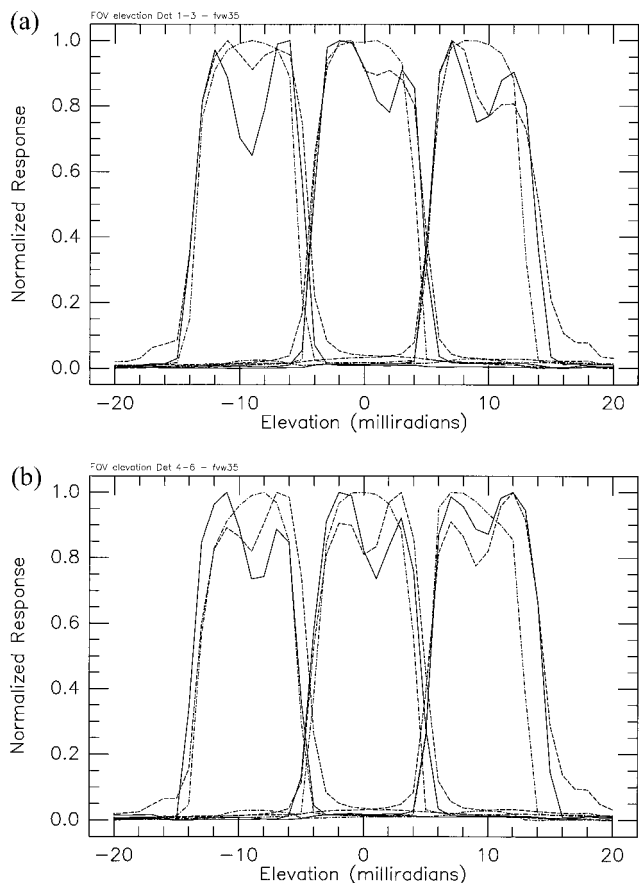


Figure B2. Prelaunch field-of-view definition and alignment in elevation direction. Detector response normalized to a 1 by 40 mrad slit. Visible/near-IR bolometer detectors, solid line; thermal bolometers, dashed line; spectrometer detectors, dot-dashed line. (a) Detectors 1–3. (b) Detectors 4–6.

between May 14, 1996, and May 26, 1996. These tests determined (1) the emissivity and effective temperature of the internal reference surface; (2) the emissivity of the instrument; (3) the instrument response function and its variation with instrument temperature; (4) the absolute radiometric accuracy; (5) the spectrometer noise characteristics; and (6) the spectrometer gain values.

The measured transformed interferometer voltage V_{measured} from the TES spectrometer as a function of wave number is given by

$$V_{\text{measured}} = [(R_{\text{emitted}} + R_{\text{reflected}}) - R_{\text{instrument}}]f, \quad (\text{B1})$$

where R_{emitted} is the radiance emitted by the target, $R_{\text{reflected}}$ is the radiance emitted by the environment and reflected off of the target, $R_{\text{instrument}}$ is the radiance emitted by the instrument, and f is the instrument response function. High emissivity targets (>0.99) were used for all of the calibration tests, and the $R_{\text{reflected}}$ term can be ignored.

During the stable thermal vacuum tests, observations were acquired of two external blackbody targets, one cold (space) and one hot (planet), and the internal reference surface (“reference”) over a period of 360 s. The relationships between the measured instrument signal V and the instrument and target radiance for the space, planet, and reference views are given by

$$V_s = (R_s - R_i)f, \quad (\text{B2a})$$

$$V_r = (R_r - R_i)f, \quad (\text{B2b})$$

$$V_p = (R_p - R_i)f, \quad (\text{B2c})$$

where R is the radiance of the space (s), planet (p), and reference (r) targets and the instrument (i). The radiance of each target is given by ϵB , where ϵ is the emissivity of each target and B is the Planck function radiance at the target temperature, giving

$$V_s = (\epsilon_s B_s - R_i)f, \quad (\text{B3a})$$

$$V_r = (\epsilon_r B_r - R_i)f, \quad (\text{B3b})$$

$$V_p = (\epsilon_p B_p - R_i)f. \quad (\text{B3c})$$

All of the values are determined at each spectral wave number (subscript omitted).

The instrument response function f is independent of signal magnitude [Christensen, 1999] but is a function of instrument temperature. However, the spectra from each target were acquired over a relatively short period of time under stable conditions, so it is assumed that the instrument temperature was the same for all three observation sets. Thus R_i and f are assumed to be constant in all three equations. The temperature of the external targets and reference surface was determined to be constant to within 0.1°C using the thermistors located in or on each target surface, and the average temperature of each target over the time interval of data collection was used in the calibration.

Equations (B3a)–(B3c) give three equations and five unknowns (ϵ_s , ϵ_p , ϵ_r , R_i , and f). Typically, it is assumed that the external reference blackbodies have an emissivity of 1. However, this assumption may not be valid because the reference cones were only several inches larger than the TES aperture, so that the TES viewed the outer extent of the cone. In this case the geometric advantage of the cone is lost, and the emissivity

Table B2. Elevation Half-Power Points Relative to TES Alignment Cube

Detector	Visible/Near-IR Bolometer		Thermal Bolometer		Spectrometer	
	Left, mrad	Right, mrad	Left, mrad	Right, mrad	Left, mrad	Right, mrad
1	13.68	5.25	14.03	5.27	12.69	5.32
2	4.64	−4.08	4.75	−4.31	4.13	−4.20
3	−4.86	−13.66	−4.53	−13.68	−5.42	−13.43
4	14.31	5.39	14.43	5.26	12.75	5.35
5	4.53	−4.18	4.87	−4.07	4.11	−3.74
6	−5.28	13.68	−4.49	−13.22	−5.36	−13.12

Table B3. Azimuth Half-Power Points Relative to TES Alignment Cube

Detector	Visible/Near-IR Bolometer		Thermal Bolometer		Spectrometer	
	Low, mrad	High, mrad	Low, mrad	High, mrad	Low, mrad	High, mrad
1	0.74	9.14	-0.17	7.92	0.27	8.51
2	0.54	9.16	-0.06	8.16	0.36	8.67
3	0.49	8.50	0.15	8.39	0.50	8.69
4	-8.91	-0.29	-8.80	-1.16	-8.91	-0.76
5	-9.39	-0.52	-9.08	-1.18	-9.05	-0.84
6	-9.03	-0.24	-8.96	-0.85	-8.50	-0.53

of the cone is given only by the emissivity of the paint. It is, however, reasonable to assume that $\varepsilon_s = \varepsilon_p$ and set these to “ $\varepsilon_{\text{cone}}$ ” (ε_c), giving three equations and four unknowns. As a result, it is possible to determine ratios only of the remaining emissivity terms.

Using (B2a) and (B2c) to determine f and R_i gives

$$f = \frac{V_s - V_r}{R_s - R_r} \quad (\text{B4a})$$

and

$$R_i = \frac{R_p V_s - R_s V_p}{V_s - V_p}. \quad (\text{B4b})$$

Solving for R_r using (B2b) gives

$$R_r = \frac{R_s(V_r - V_p) + R_p(V_s - V_r)}{V_s - V_p}. \quad (\text{B4c})$$

Replacing R_r , R_p , and R_s with their equivalent εB term gives

$$\varepsilon_r B_r = \frac{\varepsilon_s B_s(V_r - V_p) + \varepsilon_p B_p(V_s - V_r)}{V_s - V_p}. \quad (\text{B4d})$$

Finally, replacing ε_p and ε_s with ε_c and rearranging gives

$$\frac{\varepsilon_c}{\varepsilon_r} = \frac{B_r(V_s - V_p)}{B_s(V_r - V_p) + B_p(V_s - V_r)}. \quad (\text{B5})$$

B3.2. Reference surface emissivity. The ratio $\varepsilon_c/\varepsilon_r$ from (B5) is shown in Figure B3 for the average of all detectors using the stable thermal vacuum tests. The results of the $\varepsilon_c/\varepsilon_r$ emissivity ratio can be explained by assuming that the reference surface emissivity is unity and the emissivity of the external target is less than unity, with minor absorptions ($\varepsilon > 0.998$) near 450 and 1000 cm^{-1} . The fact that the internal reference surface is a better blackbody than the external targets can be explained by two effects. First, the internal target is viewed with the aperture cover closed, producing an excellent blackbody cavity. With the cover closed, the reference surface is

illuminated by energy emitted by the aft optics and detectors that is reflected off of the pointing mirror and onto the reference surface. Thermistors within the aft optics section indicate that the temperatures in this region are typically only $\sim 2^\circ\text{C}$ warmer than the reference surface. Second, as discussed previously, the geometrical advantage of the cone design for the external blackbodies is not fully utilized because the cones are only several inches larger in diameter than the TES aperture.

As a result of this analysis, it is assumed in all TES calibration that the emissivity of the internal reference surface is unity in all TES calibration calculations.

B3.3. Instrument response function versus instrument temperature. There is a significant variation in instrument response with instrument temperature due to changes in detector response and interferometer alignment with temperature. Figure B4 illustrates the variation of instrument response with temperature for detector 2 for three representative wave number samples (sample 20 = 349 cm^{-1} ; sample 80 = 984 cm^{-1} ; sample 120 = 1407 cm^{-1}). The actual instrument response is determined in flight using the two-temperature space/reference calibration process throughout each orbit.

B3.4. Noise performance. The noise equivalent spectral radiance (NESR) of the TES was determined in thermal vacuum testing by converting standard deviation in signal to radiance using the instrument response function. This approach produces an upper limit to the noise levels (a lower limit to the SNR) because other sources of variance may be present that are unrelated to the instrument itself. The most likely of these are variations in the target signal due to minor variations in target temperature.

Plate 16 gives a representative NESR for detector 1 at an instrument temperature of 9°C observing the internal reference surface. As shown in Figure B4, the instrument response function decreases with decreasing temperature. However, the noise also decreases with temperature, so that there is only an approximately 25–50% increase in the noise level at the lowest temperature measured (-16°C) [Christensen, 1999].

Table B4. Field-of-View Size: Full Width at Half Maximum

Detector	Visible/Near-IR Bolometer		Thermal Bolometer		Spectrometer	
	Elevation, mrad	Azimuth, mrad	Elevation, mrad	Azimuth, mrad	Elevation, mrad	Azimuth, mrad
1	8.42	8.40	8.75	8.09	7.37	8.23
2	8.73	8.62	9.06	8.22	8.33	8.31
3	8.81	8.01	9.14	8.24	8.01	8.18
4	8.92	8.62	9.17	7.63	7.40	8.15
5	8.72	8.87	8.94	7.90	7.86	8.21
6	8.40	8.79	8.72	8.10	7.76	7.97

Table B5. TES Alignment Cube Relative to the Spacecraft Axes

Axis	Measured Preflight Position, mrad
θX	+0.279
θY	+0.244
θZ	-0.070

B3.5. Absolute radiometric calibration. The absolute calibration of the TES was checked in vacuum at SBRS in the following manner:

1. The instrument response and instrument radiance were determined using observations of the cold external blackbody and the internal reference surface. The reference surface radiance was determined using the average of the three reference surface temperatures and assuming unity emissivity.

2. Measurements of the external planet blackbody were converted to calibrated radiance using the instrument response function and instrument radiance determined from the cold external and internal reference observations.

3. This calibrated radiance was converted to the brightness temperature of the planet blackbody at each wave number and averaged from wave number 300 to 1100 to determine the “best fit” planet temperature.

Plate 17a shows the difference between the calibrated radiance and the blackbody radiance computed using the measured planet temperature for detector 2 for all blackbody temperatures for a representative instrument temperature of +9°C. Plate 17b shows the difference between the calibrated radiance and a best fit blackbody for the same tests. As seen in Plates 17a and 17b, there are errors of up to $2 \times 10^{-7} \text{ W cm}^{-2} \text{ sr}^{-1} \text{ cm}^{-1}$ when comparing the derived calibrated radiance to the measured planet blackbody temperature. However, the errors are $<0.4 \times 10^{-7} \text{ W cm}^{-2} \text{ sr}^{-1} \text{ cm}^{-1}$ when compared to the best fit derived planet blackbody temperature. Figure B5 shows how the worst case radiance error, assuming the measured rather than best fit target temperature, maps into the absolute temperature error for the different target temperatures. As can be seen from Figure B5, the absolute temperature error is a maximum of 3.5°C for the coldest temperatures

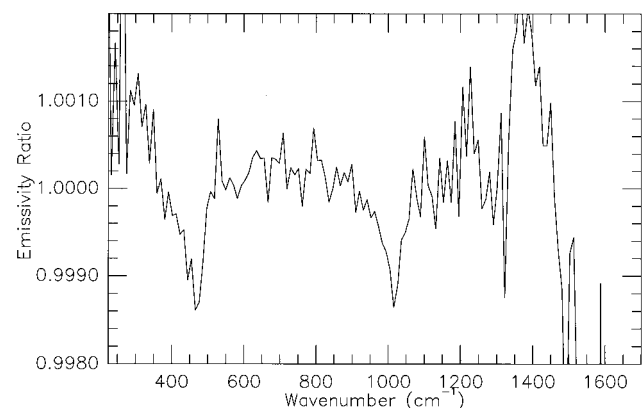


Figure B3. The ratio of the emissivity of the external cone blackbody targets (ϵ_c) to the internal reference surface (ϵ_r). Single-scan data; average of all detectors. Typical errors in this ratio are ± 0.0002 , and the spectral structure observed near 450 and 1000 cm^{-1} is reproducible.

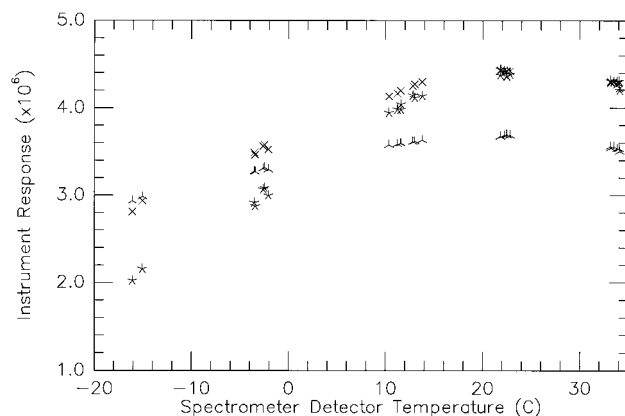


Figure B4. Instrument response versus instrument temperature. Data shown are for single-scan data at wave number sample 20 (inverted Y), 80 (cross), and 120 (star), detector 2. Response units are $\text{V/W cm}^{-2} \text{ sr}^{-1} \text{ cm}^{-1}$.

and is $<1.5^\circ\text{C}$ for typical daytime Mars temperatures. On the basis of the quality of the best fit Planck curves, we estimate that the primary error is in the calibration of the blackbody thermistors at low temperatures [Christensen, 1999]. We conclude that the absolute radiance error of the TES instrument is $0.4 \times 10^{-7} \text{ W cm}^{-2} \text{ sr}^{-1} \text{ cm}^{-1}$, with a worst case error of $2 \times 10^{-7} \text{ W cm}^{-2} \text{ sr}^{-1} \text{ cm}^{-1}$.

The instrument temperature can be determined from the derived instrument radiance. The instrument temperature is essentially the detector temperature, which is typically warmer than the temperature of the thermistor mounted on the spectrometer housing (TS3) owing to the direct absorption of Martian radiance. The differences between the derived and measured temperature range from $0.5^\circ\text{--}1^\circ\text{C}$ at low instrument temperatures to $2.5^\circ\text{--}3.5^\circ\text{C}$ at high instrument temperatures.

B3.6. Gain. The TES spectrometer has four internal gain settings that nominally are 1, 2.5, 4, and 8. A concerted attempt was made to achieve these values using 1% precision resistors. The actual value of the gain is stored in the Instrument Parameter Tuning Table on board the instrument. The values in this table are used in the flight software to divide the measured signal prior to transmission to Earth. The parameters in this table are adjustable on ground command.

The actual instrument gain settings were evaluated by cycling through all four gain settings viewing both the internal reference surface and the external targets. The results show that the actual gain states are 1.00, 2.54, 4.00, and 8.05 [Christensen, 1999].

B3.7. Sample position and spectral line shape. In an ideal interferometer with an on-axis point detector, the spectral samples are uniformly distributed in wave number, and the full width at half maximum (FWHM) of each sample is simply determined by the optical displacement of the Michelson mirror. The TES uses a neon bulb with a line at $0.7032 \mu\text{m}$ in the visible interferometer to sample the IR interferometer. The ideal sample spacing of the interferometer is given by

$$S_{\text{spacing}} = \frac{1}{(0.7032 \times 10^{-4} \text{ cm}) N_{\text{pts}}},$$

where N_{pts} is the number of points in the FFT.

For a large detector the two beams of the interferometer are not in phase over the entire areal extent of the detector, pro-

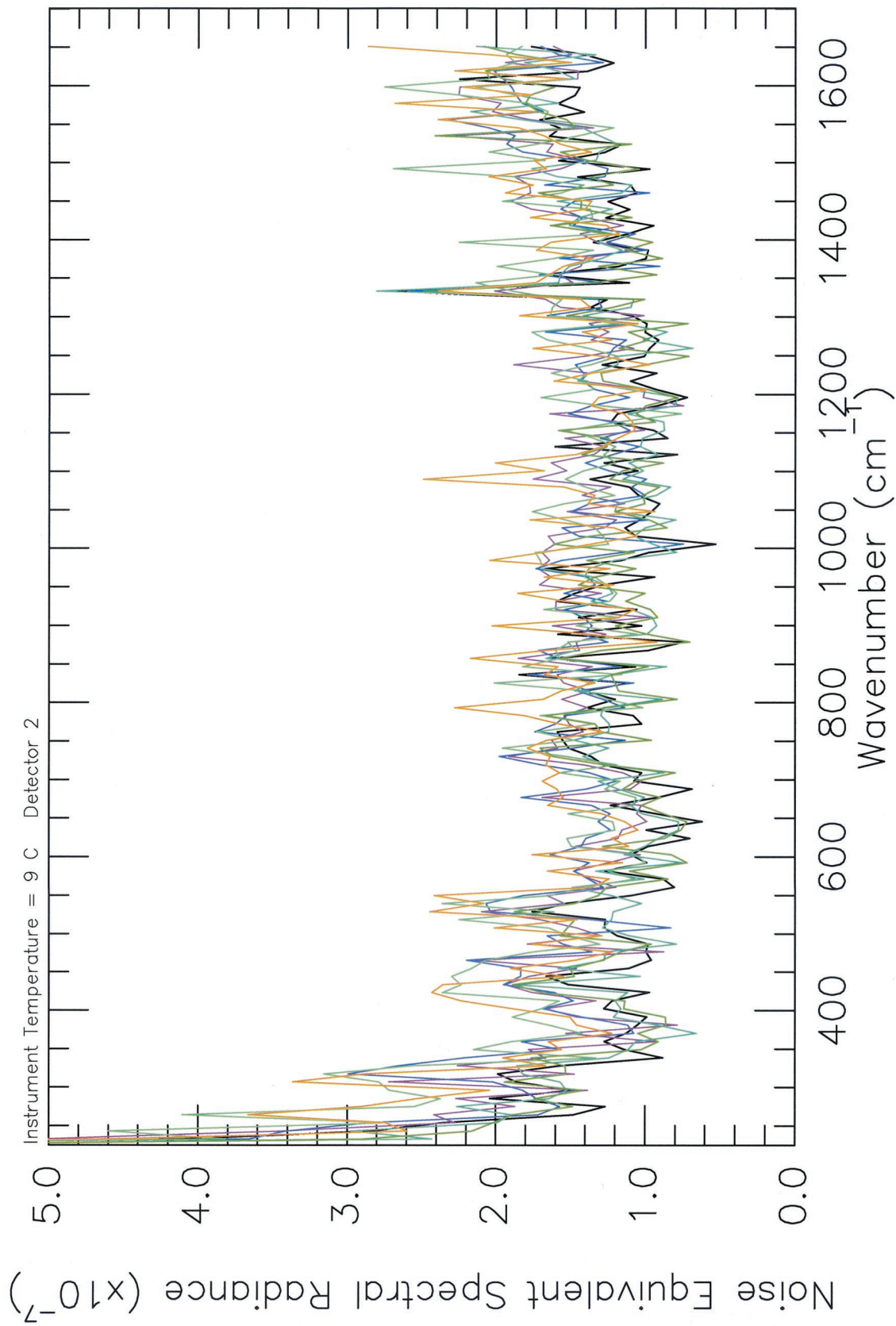


Plate 16. Noise-equivalent spectral radiance. Data were acquired viewing the internal reference surface in single-scan mode. Data were acquired during SBRS thermal vacuum testing with the instrument at +9°C at seven different planet temperatures. Data are shown for detector 1. Radiance units are $\text{W cm}^{-2} \text{sr}^{-1} \text{cm}^{-1}$.

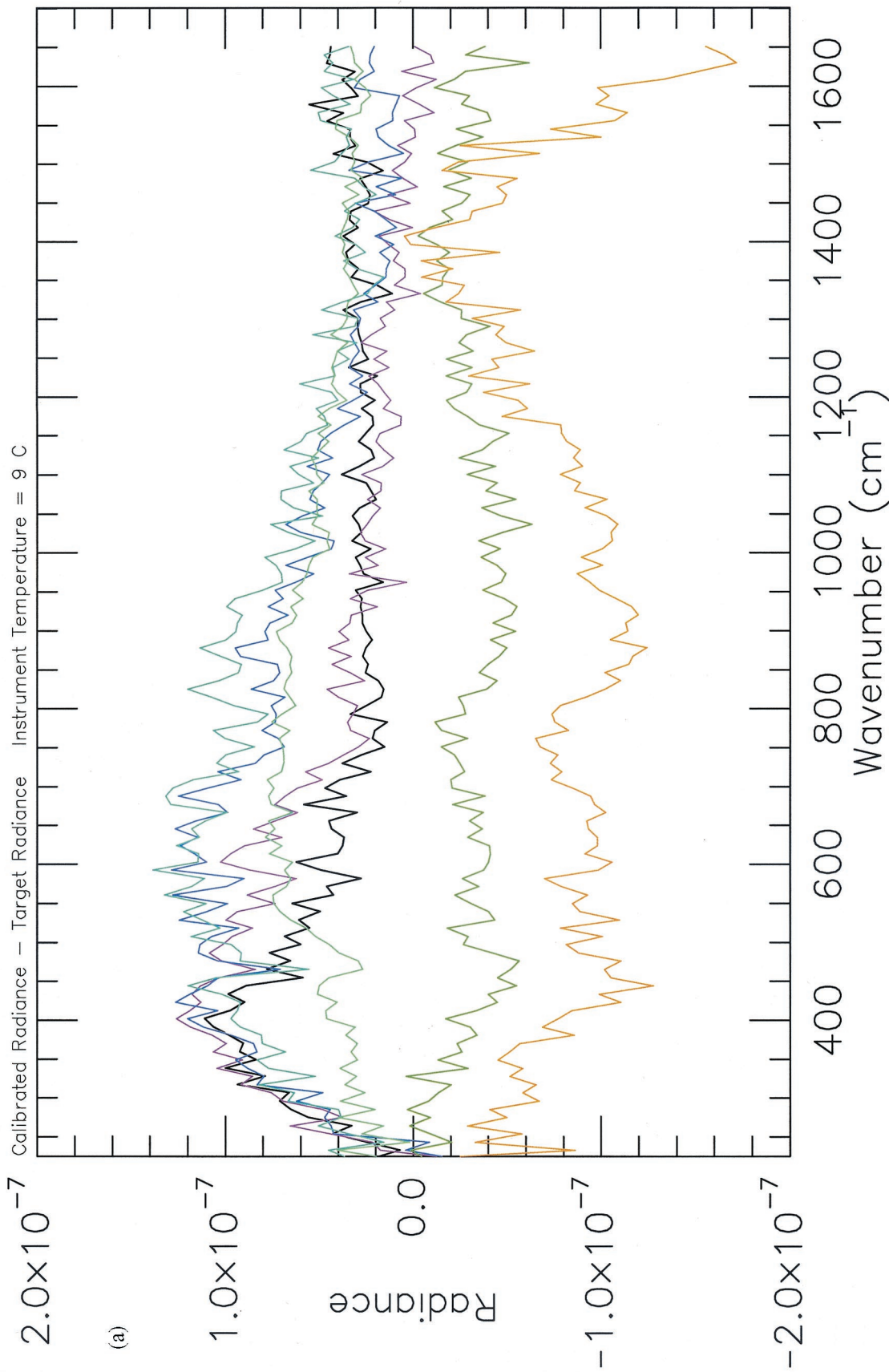


Plate 17. The difference between the TES-derived radiance and the radiance of the “planet” target blackbody. Representative values for detector 2, instrument temperature of +9°C. Radiance units of $\text{W cm}^{-2} \text{sr}^{-1} \text{cm}^{-1}$. (a) Radiance difference using the measured temperature of the external blackbody target. (b) Radiance difference using the temperature derived from a Planck function fit to the TES-derived radiance.

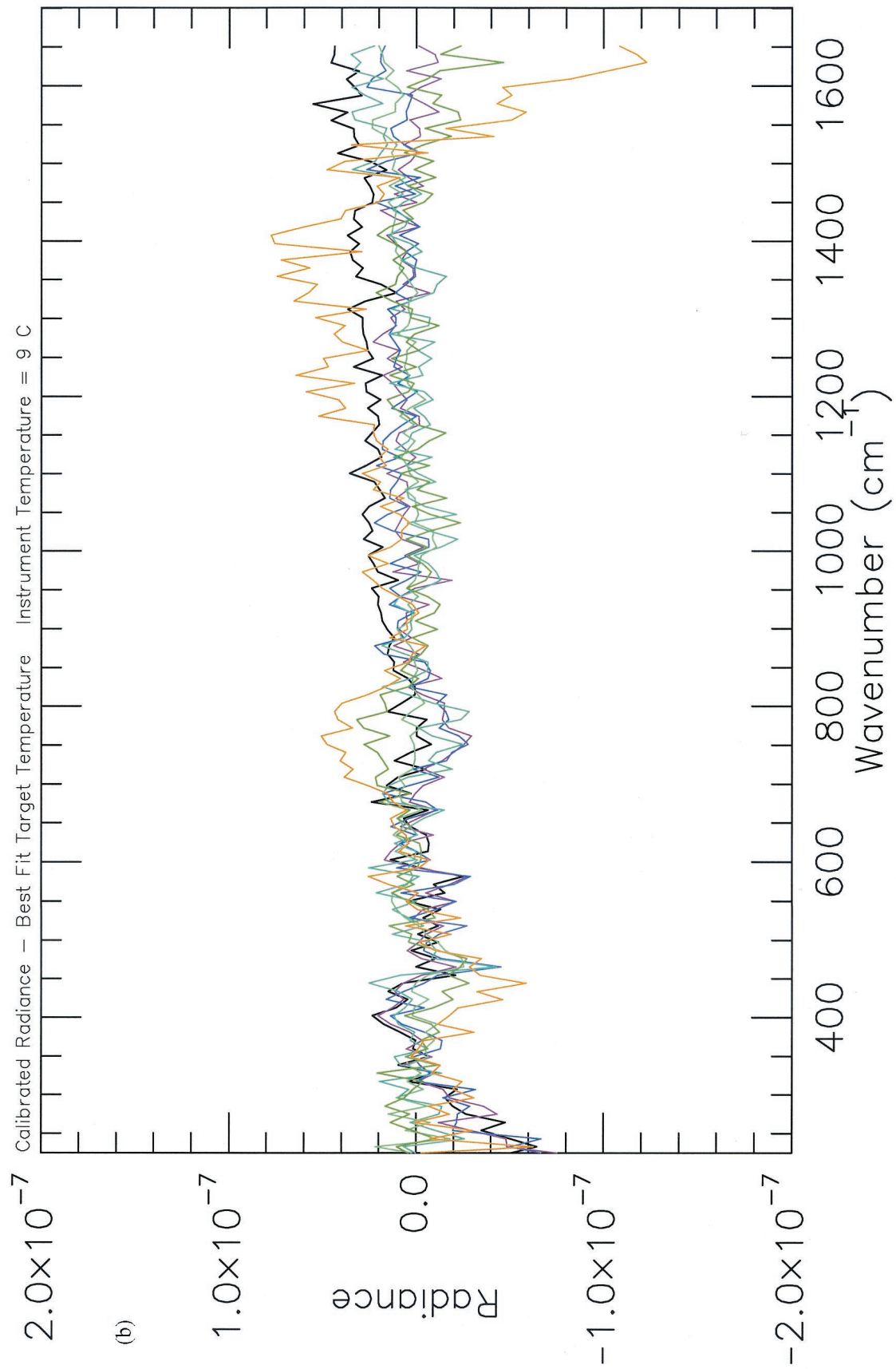


Plate 17. (continued)

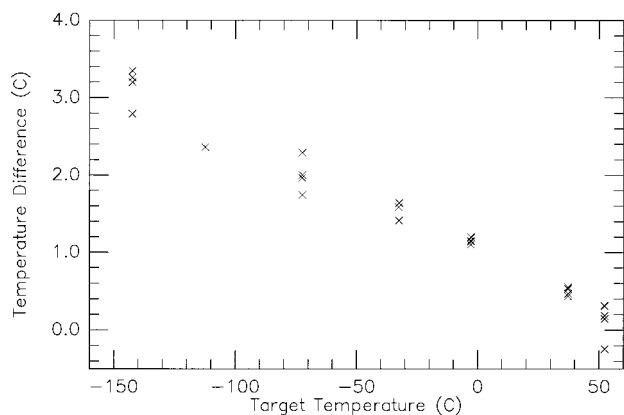


Figure B5. The difference between the TES-derived planet target temperature and the measured thermistor temperature versus planet temperature ($^{\circ}\text{C}$). Data from all tests at each instrument set-point temperature are shown for detector 2.

ducing “self-apodization,” or widening of the instrument line shape. In addition, the path length of the rays traveling to the off-axis portion of each detector is decreased relative to the optical axis rays by a factor of $\cos \theta$, where θ is the angle of the off-axis ray. As a result, the mirror must move farther to produce interference of the off-axis rays, producing a shift of the center frequency of each spectral sample to a higher apparent wavelength (lower wave number) than its true spectral position. All six detectors are offset from the optical axis, producing separate shifts in the spectral line position, shape, and modulation efficiency of each detector.

The TES flight software processes the interferogram data with prime factor FFTs that use a different number of points for the center and edge detectors, respectively. These FFTs were selected to produce a slightly different spacing that partially compensates for the different spectral offsets due to self-apodization between the edge and center detectors. The

number of points and the ideal sample spacing and position from these FFTs are given in Table B6.

A numerical model has been developed to model the self-apodization effects and to determine the true spectral position, FWHM, and spectral line shape of each sample. Because the focal plane is symmetric in the cross-track direction (e.g., detectors 1 and 3 are symmetrically located relative to the optical axis), the position and FWHM are identical for detector pairs 1 and 3 and detector pairs 4 and 6. The true sample position was calculated for each detector, taking into account the actual prime factor FFT used for each detector. Interferogram data were collected immediately after Mars orbit insertion, and the atmospheric CO_2 band positions were used to verify the spectral position model to $\sim 2 \text{ cm}^{-1}$. Examples of the true sample center wave number position, position offset relative to the ideal FFT sample position, and FWHM for the double-scan samples 1, 148, and 296 are given in Table B7; the single-scan values are exactly doubled. The full set of sample positions, offsets, and full width at half maximum values are given by Christensen [1999].

B3.8. In-flight calibrated radiance algorithm. The following sequence of operations is carried out for spectral calibration:

1. Find all of the single- and double-scan space/reference (SR) pairs and space observations (S) in the given set of observations.
2. At each SR pair, compute the radiance of the instrument (R_i), the instrument response function f , and the temperature of the instrument (T_i) (for reference only) for each detector using (B4a) and (B4b).
3. Replicate the first and last SR pairs at the beginning and end of the given set of observations, respectively.
4. At each space observation, compute R_i for each detector using (B4b); f is determined by interpolating over time between bounding SR pairs.
5. At each planet observation, determine f and R_i by in-

Table B6. Ideal Sample Position from the Fourier Transform

	Edge Detectors (1, 3, 4, and 6)		Center Detectors (2 and 5)	
	Single Scan	Double Scan	Single Scan	Double Scan
N_{pts} in FFT	1350	2700	1344	2688
Sample spacing, cm^{-1}	10.53	5.267	10.58	5.290
Sample 1 position, cm^{-1}	147.47	147.47	148.13	148.13
Sample 148 (single; 296 double) position, cm^{-1}	1695.95	1701.22	1703.52	1708.81

Table B7. Self-Apodization: Double Scan

	Edge Detectors (1 and 3), cm^{-1}	Center Detector (2), cm^{-1}
Sample 1 self-apodization position	148.66	148.57
Sample 1 offset	1.19	0.44
Sample 1 FWHM	6.33	6.24
Sample 148 self-apodization position	929.29	928.81
Sample 148 offset	7.56	3.06
Sample 148 FWHM	7.95	6.66
Sample 296 self-apodization position	1715.22	1714.26
Sample 296 offset	14.00	5.45
Sample 296 FWHM	13.63	7.83

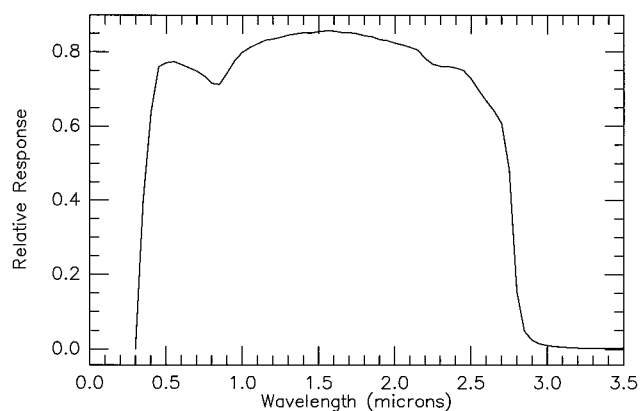


Figure B6. Visible/near-IR bolometer relative spectral response.

terpolating over time between the bounding SR pair or S observations and compute R_p for each detector using

$$R_p = (V_p/f) + R_i.$$

B4. Visible/Near-IR Bolometer Radiometric Calibration

The TES visible/near-IR bolometer uses periodic views of two redundant internal lamps and more frequent views of space to provide a two-point calibration. The system linearity, gain, relative spectral response, absolute lamp radiance, lamp variation with temperature, and detector response variation with temperature were determined prior to launch [Christensen, 1999].

The system was determined to be linear to within <1% and is assumed to be linear in the TES calibration algorithms. The visible/near-IR bolometer has two gain states with the high gain nominally set to a factor of 2 higher than the low-gain state. The high-gain state was determined to be 2.00 ± 0.001 and is assumed to be precisely 2.0 in the TES calibration algorithms. The relative spectral response was determined by measuring the TES visible/near-IR filter and detector response prior to installation [Christensen, 1999] and is shown in Figure B6.

The absolute internal lamp radiances were determined with TES in a vacuum chamber viewing an external calibrated light source (lamp temperature of 28.2°C) reflected off of a calibrated halon target (Table B8). The mirror transmission was removed at ambient conditions viewing the calibrated source with and without the window in the path. The variation in lamp radiance with temperature is given in Table B9. The detector

response with temperature was fit with a second-order polynomial that is discussed in detail by Christensen [1999].

B5. Thermal Bolometer Radiometric Calibration

The thermal bolometer relative spectral response was determined at the piece-part level. The response of the pyroelectric DTGS detector was assumed to be constant, and the aluminum mirrors were assumed to have a flat spectral reflectance across the thermal bolometer band. The relative spectral response of the filter used in the thermal bolometers is shown in Figure B7. This response is taken to be equal to the overall relative spectral response of the thermal bolometers and is used to calculate the integrated radiance observed by the thermal bolometer detectors in the radiance calibration.

The thermal bolometer has two gain states with the high gain nominally set to a factor of 2 higher than the low-gain state. The high-gain state was determined to be 2.00 ± 0.01 and is assumed to be precisely 2.0 in the TES calibration algorithms.

Appendix C: TES Standard Data Product Fields

The raw data fields are as follows: (all).DETECTOR_NUMBER, (all).SPACECRAFT_CLOCK_START_COUNT, BOL.BOLOMETRIC_BRIGHTNESS_TEMP, BOL.RAW_THERMAL_BOLOMETER, BOL.RAW_VISUAL_BOLOMETER, BOL.TEMPORAL_INTEGRATION_SCAN_NUMBER, CMP.FFT_COMPLEX_DATA, IFG.INTERFEROGRAM_DATA, OBS.DATA_PACKET_TYPE, OBS.DETECTOR_MASK, OBS.FFT_START_INDEX, OBS.IMC_COUNT, OBS.INSTRUMENT_TIME_COUNT, OBS.MIRROR_POINTING_ANGLE, OBS.OBSERVATION_TYPE, OBS.ORBIT_COUNTER_KEEPER, OBS.ORBIT_NUMBER, OBS.PREPROCESSOR_DETECTOR_NUMBER, OBS.PRIMARY_DIAGNOSTIC_TEMPERATURES, OBS.SCAN_LENGTH, OBS.SCHEDULE_TYPE, OBS.SPECTROMETER_GAIN, OBS.THERMAL_BOLOMETER_GAIN, OBS.VISUAL_BOLOMETER_GAIN, OBS.TEMPORAL_AVERAGE_COUNT, RAD.COMPRESSION_MODE, RAD.RAW_RADIANCE, RAD.SPECTRAL_MASK, TLM.AUXILIARY_DIAGNOSTIC_TEMPS, TLM.DIAGNOSTIC_TELEMETRY_(1:20), TLM.INTERFEROGRAM_END, TLM.INTERFEROGRAM_MAXIMUM, TLM.INTERFEROGRAM_MINIMUM, TLM.INTERFEROGRAM_ZPD, TLM.NEON_AMPLITUDE, TLM.NEON_GAIN, TLM.NEON_LAMP, TLM.NEON_ZPD, and TLM.ONBOARD_PROCESSING_EVENT_LOG.

The SPICE kernel fields are as follows: GEO.EMISSION_

Table B8. Absolute Integrated Radiance of the TES Internal Lamps at 28.2°C^a

	Lamp 1 ($\times 10^{-3} \text{ W cm}^{-2} \text{ str}^{-1}$)		Lamp 2 ($\times 10^{-3} \text{ W cm}^{-2} \text{ str}^{-1}$)	
	Mean	Sigma	Mean	Sigma
Detector 1	5.0035	0.0019	3.8218	0.0019
Detector 2	4.8693	0.0011	3.7159	0.0000
Detector 3	4.3790	0.0004	3.4456	0.0011
Detector 4	4.1508	0.0048	4.0489	0.0019
Detector 5	4.4117	0.0059	3.8620	0.0015
Detector 6	3.8553	0.0037	3.5075	0.0015

^aThe absolute integrated radiance is measured at 0.3–3.5 μm . The 28.2°C temperature of the internal lamps is the ambient temperature.

Table B9. Variation in Integrated Lamp Radiance With Temperature: $\partial(RL)/\partial TL$

Detector	Lamp 1 ($\times 10^{-6}$)	Lamp 2 ($\times 10^{-6}$)
1	-4.3310	-3.1797
2	-6.0982	-4.7713
3	-4.7611	-3.5958
4	-6.0439	-4.0096
5	-6.1965	-3.7917
6	-7.6986	-5.3154

ANGLE, GEO.INCIDENCE_ANGLE, GEO.LATITUDE, GEO.LOCAL_TIME, GEO.LONGITUDE, GEO.PHASE_ANGLE, GEO.PLANETARY_PHASE_ANGLE, GEO.SOLAR_DISTANCE, GEO.SOLAR_LONGITUDE, GEO.SPACECRAFT_ALTITUDE, GEO.SUB_SOLAR_LATITUDE, GEO.SUB_SOLAR_LONGITUDE, GEO.SUB_SPACECRAFT_LATITUDE, GEO.SUB_SPACECRAFT_LONGITUDE, GEO.TARGET_ALTITUDE, GEO.TARGET_DISTANCE, POS.EPHEMERIS_TIME, POS.MARS_QUATERNION, POS.POSITION_SOURCE_ID, POS.SPACECRAFT_POSITION, POS.SPACECRAFT_QUATERNION, and POS.SUN_POSITION.

The calibrated data fields are as follows: BOL.CALIBRATED_VISUAL_BOLOMETER, BOL.BOLOMETER_CALIBRATION_ID, GEO.GEOMETRY_CALIBRATION_ID, RAD.CALIBRATED_RADIANCE, and RAD.RADIANCE_CALIBRATION_ID.

The derived fields are as follows: BOL.LAMBERT_ALBEDO, BOL.BOLOMETRIC_THERMAL_INERTIA, GEO.PLANETARY_ANGULAR_RADIUS, OBS.OBSERVATION_CLASSIFICATION, OBS.OBSERVATION_CLASSIFICATION:CLASSIFICATION_VALUE, OBS.OBSERVATION_CLASSIFICATION:INTENDED_TARGET, OBS.OBSERVATION_CLASSIFICATION:MISSION_PHASE, OBS.OBSERVATION_CLASSIFICATION:NEON_LAMP_STATUS, OBS.OBSERVATION_CLASSIFICATION:SPARE, OBS.OBSERVATION_CLASSIFICATION:TES_SEQUENCE, OBS.OBSERVATION_CLASSIFICATION:TIMING_ACCURACY, OBS.QUALITY, OBS.QUALITY:ALGOR_PATCH, OBS.QUALITY:EQUALIZATION_TABLE, OBS.QUALI-

TY:HGA_MOTION, OBS.QUALITY:IMC_PATCH, OBS.QUALITY:MOMENTUM_DESATURATION, OBS.QUALITY:SOLAR_PANEL_MOTION, RAD.DETECTOR_TEMPERATURE, RAD.TARGET_TEMPERATURE, RAD.QUALITY, RAD.QUALITY:ALGOR_RISK, RAD.QUALITY:CALIBRATION_QUALITY, RAD.QUALITY:MAJOR_PHASE_INVERSION, and RAD.QUALITY:SPECTROMETER_NOISE.

The preliminary derived fields (to be rereleased) are as follows: LMB.AEROSOL_OPACITY_PROFILE_LIMB, LMB.AEROSOL_OPACITY_SPECTRUM_LIMB, LMB.AEROSOL_SNG_SCAT_ALB_SPECTRUM, LMB.LIMB_PARAMETERS_QUALITY, LMB.LIMB_TEMPERATURE_PROFILE, LMB.SURFACE_RAD_SPECTRUM_UNCERTAINTY, LMB.AEROSOL_SNG_SCAT_PRESSURE_LEVEL_IND, SRF.AEROSOL_OPACITY_NADIR, SRF.DOWN_WELLING_FLUX, SRF.NADIR_TEMPERATURE_PROFILE, SRF.SPECTRAL_SURFACE_TEMPERATURE, SRF.SPECTRAL_THERMAL_INERTIA, SRF.SURFACE_CALIBRATION_ID, SRF.SURFACE_PARAMETERS_QUALITY, SRF.SURFACE_PRESSURE, and SRF.SURFACE_RADIANCE.

Acknowledgments. We wish to thank the entire TES Engineering Team at Raytheon Santa Barbara Remote Sensing for their care and dedication in the design, fabrication, and calibration of the TES instrument that produced the high-quality data discussed here. Ken Edgett, Scott Nowicki, Laura Aben, Laurel Cherednik, Kevin Mullins, and Todd Hoefen participated in stimulating discussions on the topics discussed here. Raymond Arvidson and Frank Palluconi provided very helpful reviews. We thank Kamran Qazi, Saadat Anwar, Michael Weiss-Malik, Kim Homan, and Tara Fisher for their dedicated efforts in the planning, acquisition, and processing of the TES data at ASU. M. Kaelberer, K. Horrocks, C. Martin, and E. Winter contributed significantly to the development of the atmosphere analysis software. Finally, we wish to acknowledge our appreciation of the outstanding efforts of the MGS Spacecraft Teams at Lockheed Martin and NASA's Jet Propulsion Laboratory that have led to the success of the MGS mission. This work was supported by the NASA Mars Global Surveyor Project Office and the NASA Planetary Geology and Geophysics Program.

References

- Adams, J. B., M. O. Smith, and P. E. Johnson, Spectral mixture modeling: A new analysis of rock and soil types at the Viking Lander 1 site, *J. Geophys. Res.*, *91*, 8098–8112, 1986.
- Albee, A. L., R. E. Arvidson, F. D. Palluconi, and T. E. Thorpe, Overview of the Mars Global Surveyor mission, *J. Geophys. Res.*, this issue.
- Arvidson, R., E. Guinness, S. Slavney, and R. J. Springer, MGS archive generation, validation, and transfer plan, *MGS Doc. 542-312*, Jet Propul. Lab., Pasadena, Calif., 1998.
- Bandfield, J. L., V. E. Hamilton, and P. R. Christensen, A global view of Martian volcanic compositions, *Science*, *287*, 1626–1630, 2000a.
- Bandfield, J. L., M. D. Smith, and P. R. Christensen, Spectral data set factor analysis and end-member recovery: Application to analysis of Martian atmospheric particulates, *J. Geophys. Res.*, *105*, 9573–9588, 2000b.
- Basaltic Volcanism Study Project, *Basaltic Volcanism on the Terrestrial Planets*, 1286 pp., Pergamon, New York, 1981.
- Bell, J. F., III, Iron, sulfate, carbonate, and hydrated minerals on Mars, in *Mineral Spectroscopy: A Tribute of Roger G. Burns*, edited by M. D. Dyar, C. McCammon, and M. W. Schaefer, *Spec. Publ. Geochem. Soc.*, *5*, 359–380, 1996.
- Bell, J. F., III, and R. V. Morris, Identification of hematite on Mars from HST, *Lunar Planet. Sci.*, *XXX*, abstract 1751, 1999.
- Bell, J. F., III, M. J. Wolff, P. B. James, R. T. Clancy, S. W. Lee, and L. J. Martin, Mars surface mineralogy from Hubble Space Telescope

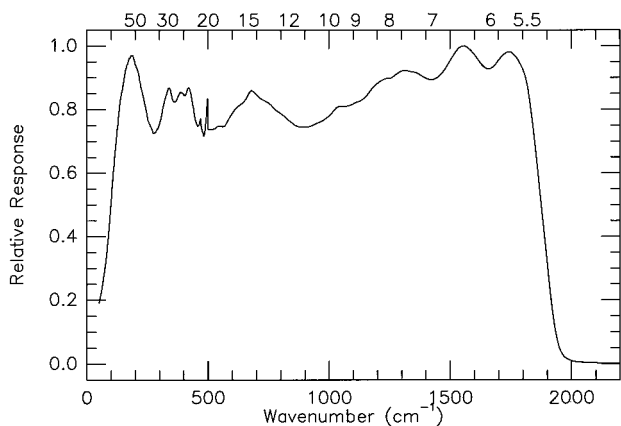


Figure B7. Thermal bolometer relative spectral response. The relative spectral response of the bolometer filter is assumed to be the overall relative spectral response of the bolometer. Upper scale is wavelength in μm .

- imaging during 1994–1995: Observations, calibration, and initial results, *J. Geophys. Res.*, *102*, 9109–9123, 1997.
- Bell, J. F., III, et al., Mineralogic and compositional properties of Martian soil and dust: Results from Mars Pathfinder, *J. Geophys. Res.*, *105*, 1721–1755, 2000.
- Blaney, D. L., and T. B. McCord, Indications of sulfate minerals in the Martian soil from Earth-based spectroscopy, *J. Geophys. Res.*, *100*, 14,433–14,441, 1995.
- Booth, M. C., and H. H. Kieffer, Carbonate formation in Marslike environments, *J. Geophys. Res.*, *83*, 1809–1815, 1978.
- Brain, D. A., and B. M. Jakosky, Atmospheric loss since the onset of the Martian geologic record: Combined role of impact erosion and sputtering, *J. Geophys. Res.*, *103*, 22,689–22,694, 1998.
- Chase, S. C., Jr., J. L. Engel, H. W. Eyerly, H. H. Kieffer, F. D. Palluconi, and D. Schofield, Viking infrared thermal mapper, *Appl. Opt.*, *17*, 1243–1251, 1978.
- Christensen, P. R., Global albedo variations on Mars: Implications for active aeolian transport, deposition, and erosion, *J. Geophys. Res.*, *93*, 7611–7624, 1988.
- Christensen, P. R., The Martian surface layer, paper presented at Fourth International Conference on Mars, Jet Propul. Lab., Tucson, Ariz., 1989.
- Christensen, P. R., Calibration report for the Thermal Emission Spectrometer (TES) for the Mars Global Surveyor mission, Mars Global Surveyor Project, Jet Propul. Lab., Pasadena, Calif., 1999.
- Christensen, P. R., and S. T. Harrison, Thermal infrared emission spectroscopy of natural surfaces: Application to desert varnish coatings on rocks, *J. Geophys. Res.*, *98*(B11), 19,819–19,834, 1993.
- Christensen, P. R., and H. H. Kieffer, Moderate resolution thermal mapping of Mars: The channel terrain around the Chryse Basin, *J. Geophys. Res.*, *84*(B14), 8233–8238, 1979.
- Christensen, P. R., and H. J. Moore, The Martian surface layer, in *Mars*, edited by H. H. Kieffer et al., pp. 686–729, Univ. of Ariz. Press, Tucson, 1992.
- Christensen, P. R., et al., Thermal Emission Spectrometer experiment: The Mars Observer mission, *J. Geophys. Res.*, *97*, 7719–7734, 1992.
- Christensen, P. R., B. M. Jakosky, H. H. Kieffer, M. C. Malin, J. H. Y. McSween, K. Nealon, G. Mehall, S. Silverman, and S. Ferry, The Thermal Emission Imaging System (THEMIS) Instrument for the Mars 2001 Orbiter, *Lunar Planet. Sci.* [CD-ROM], XXX, abstract 1470, 1999.
- Christensen, P. R., J. L. Bandfield, V. E. Hamilton, D. A. Howard, M. D. Lane, J. L. Piatek, S. W. Ruff, and W. L. Stefanov, A thermal emission spectral library of rock-forming minerals, *J. Geophys. Res.*, *105*, 9735–9738, 2000a.
- Christensen, P. R., J. L. Bandfield, M. D. Smith, V. E. Hamilton, and R. N. Clark, Identification of a basaltic component on the Martian surface from Thermal Emission Spectrometer data, *J. Geophys. Res.*, *105*, 9609–9622, 2000b.
- Christensen, P. R., et al., Detection of crystalline hematite mineralization on Mars by the Thermal Emission Spectrometer: Evidence for near-surface water, *J. Geophys. Res.*, *105*, 9623–9642, 2000c.
- Christensen, P. R., M. C. Malin, R. V. Morris, J. L. Bandfield, and M. D. Lane, Global mapping of Martian hematite mineral deposits: Remnants of water-driven processes on early Mars, *J. Geophys. Res.*, in press, 2001.
- Clark, B. C., and A. K. Baird, Is the Martian lithosphere sulphur rich?, *J. Geophys. Res.*, *84*(B14), 8395–8403, 1979.
- Clark, R. N., and T. M. Hoefen, Spectral feature mapping with Mars Global Surveyor Thermal Emission Spectra: Mineral implications (abstract), *Bull. Am. Astron. Soc.*, *32*(3), 1118, 2000.
- Conel, J. E., Infrared emissivities of silicates: Experimental results and a cloudy atmosphere model of spectral emission from condensed particulate mediums, *J. Geophys. Res.*, *74*, 1614–1634, 1969.
- Conrath, B. J., Thermal structure of the Martian atmosphere during the dissipation of the dust storm of 1971, *Icarus*, *24*, 36–46, 1975.
- Conrath, B., R. Curran, R. Hanel, V. Kunde, W. Maguire, J. Pearl, J. Pirraglia, and J. Walker, Atmospheric and surface properties of Mars obtained by infrared spectroscopy on Mariner 9, *J. Geophys. Res.*, *78*, 4267–4278, 1973.
- Curran, R. J., B. J. Conrath, R. A. Hanel, V. G. Kunde, and J. C. Pearl, Mars: Mariner 9 spectroscopic evidence for H₂O ice clouds, *Science*, *182*, 381–383, 1973.
- Davies, D. W., C. B. Farmer, and D. D. LaPorte, Behavior of volatiles in Mars' polar areas: A model incorporating new experimental data, *J. Geophys. Res.*, *82*, 3815–3822, 1977.
- Edgett, K. S., and P. R. Christensen, The particle size of Martian aeolian dunes, *J. Geophys. Res.*, *96*, 22,765–22,776, 1991.
- Edgett, K. S., and T. J. Parker, Water on early Mars: Possible subaqueous sedimentary deposits covering ancient cratered terrain in western Arabia and Sinus Meridiani, *Geophys. Res. Lett.*, *24*, 2897–2900, 1997.
- Edgett, K. S., R. B. Singer, and P. E. Geissler, Opportunity to sample something different: The dark, unweathered, mafic sands of Cerberus and the Pathfinder 1997 Mars landing, in *Mars Pathfinder Landing Site Workshop*, p. 25, Lunar and Planet. Inst., Houston, Tex., 1994.
- Erard, S., J.-P. Bibring, and Y. Langevin, Determination of spectral units in the Syrtis Major-Isidis Planitia region from Phobos/ISM observations, *Lunar Planet. Sci.*, *XX*, 327, 1990.
- Fanale, F. P., and B. M. Jakosky, Regolith-atmosphere exchange of water and carbon dioxide on Mars: Effects on atmospheric history and climate change, *Planet. Space Sci.*, *30*, 819–831, 1982.
- Fanale, F. P., S. E. Postawko, J. B. Pollack, M. H. Carr, and R. O. Pepin, Epochal climate change and volatile history, in *Mars*, edited by H. H. Kieffer et al., pp. 1135–1179, Univ. of Ariz. Press, Tucson, 1992.
- Farmer, V. C., *The Infrared Spectra of Minerals*, 539 pp., Mineral. Soc., London, 1974.
- Feely, K. C., and P. R. Christensen, Quantitative compositional analysis using thermal emission spectroscopy: Application to igneous and metamorphic rocks, *J. Geophys. Res.*, *104*, 24,195–24,210, 1999.
- Gillespie, A. R., A. B. Kahle, and F. D. Palluconi, Mapping alluvial fans in Death Valley, CA, using multichannel thermal infrared images, *Geophys. Res. Lett.*, *11*(11), 1153–1156, 1984.
- Guinness, E. A., R. E. Arvidson, M. A. Dale-Bannister, R. B. Singer, and E. A. Bruchenthal, On the spectral reflectance properties of materials exposed at the Viking landing sites, *Proc. Lunar. Planet. Sci. Conf. 17th*, Part 2, *J. Geophys. Res.*, *92*, suppl., E575–E587, 1987.
- Guinness, E. A., R. E. Arvidson, I. H. D. Clark, and M. K. Shepard, Optical scattering properties of terrestrial varnished basalts compared with rocks and soils at the Viking landing sites, *J. Geophys. Res.*, *102*, 28,687–28,703, 1997.
- Haberle, R. M., and B. M. Jakosky, Sublimation and transport of water from the north residual polar cap on Mars, *J. Geophys. Res.*, *95*(B2), 1423–1437, 1990.
- Haberle, R. M., and B. M. Jakosky, Atmospheric effects on the remote determination of thermal inertia on Mars, *Icarus*, *90*, 187–204, 1991.
- Hamilton, V. E., Thermal infrared emission spectroscopy of the pyroxene mineral series, *J. Geophys. Res.*, *105*, 9701–9716, 2000.
- Hamilton, V. E., and P. R. Christensen, Determination of modal mineralogy in mafic and ultramafic igneous rocks using thermal emission spectroscopy, *J. Geophys. Res.*, *105*, 9717–9734, 2000.
- Hamilton, V. E., P. R. Christensen, and H. Y. McSween Jr., Determination of Martian meteorite lithologies and mineralogies using vibrational spectroscopy, *J. Geophys. Res.*, *102*, 25,593–25,603, 1997.
- Hanel, R. A., B. Schlachman, F. D. Clark, C. H. Prokesh, J. B. Taylor, W. M. Wilson, and L. Chaney, The Nimbus III Michelson interferometer, *Appl. Opt.*, *9*(8), 1767–1774, 1970.
- Hanel, R., et al., Investigation of the Martian environment by infrared spectroscopy on Mariner 9, *Icarus*, *17*, 423–442, 1972a.
- Hanel, R., B. Schlachman, E. Breihar, R. Bywaters, F. Chapman, M. Rhodes, D. Rogers, and D. Vanous, Mariner 9 Michelson interferometer, *Appl. Opt.*, *11*(11), 2625–2634, 1972b.
- Hanel, R., D. Crosby, L. Herath, D. Vanous, D. Collins, H. Creswick, C. Harris, and M. Rhodes, Infrared spectrometer for Voyager, *Appl. Opt.*, *19*, 1391–1400, 1980.
- Hoefen, T. M., R. N. Clark, J. C. Pearl, and M. D. Smith, Unique spectral features in Mars Global Surveyor thermal emission spectra: Implications for surface mineralogy in Nili Fossae (abstract), *Bull. Am. Astron. Soc.*, *32*(3), 1118, 2000.
- Hook, S. J., K. E. Karlstrom, C. F. Miller, and K. J. W. McCaffrey, Mapping the Piute Mountains, California, with thermal infrared multispectral scanner (TIMS) images, *J. Geophys. Res.*, *99*, 15,605–15,622, 1994.
- Hunt, G. R., and J. W. Salisbury, Mid-infrared spectral behavior of metamorphic rocks, *Environ. Res. Pap.*, *543-AFCRL-TR-76-0003*, 67 pp., Air Force Cambridge Res. Lab., Hanscom Air Force Base, Mass., 1976.
- Jakosky, B. M., and P. R. Christensen, Global duricrust on Mars: Analysis of remote sensing data, *J. Geophys. Res.*, *91*(B3), 3547–3560, 1986.

- Jakosky, B. M., and M. T. Mellon, High-resolution thermal inertia mapping of Mars: Sites of exobiological interest, *J. Geophys. Res.*, this issue.
- Jakosky, B. M., M. T. Mellon, H. H. Kieffer, P. R. Christensen, E. S. Varnes, and S. W. Lee, The thermal inertia of Mars from the Mars Global Surveyor Thermal Emission Spectrometer, *J. Geophys. Res.*, *105*, 9643–9652, 2000.
- James, P. B., and G. R. North, The seasonal CO₂ cycle on Mars: An application of an energy balance climate model, *J. Geophys. Res.*, *87*, 10,271–10,284, 1982.
- Kahle, A., F. D. Palluconi, and P. R. Christensen, Thermal emission spectroscopy: Application to Earth and Mars, in *Remote Geochemical Analysis: Elemental and Mineralogical Composition*, edited by C. M. Pieters and P. A. J. Englert, pp. 99–120, Cambridge Univ. Press, New York, 1993.
- Kahn, R., The evolution of CO₂ on Mars, *Icarus*, *62*, 175–190, 1985.
- Kass, D. M., and Y. L. Yung, Loss of atmosphere from Mars due to solar wind-induced sputtering, *Science*, *268*, 697–699, 1995.
- Kieffer, H. H., Mars south polar spring and summer temperatures: A residual CO₂ frost, *J. Geophys. Res.*, *84*, 8263–8289, 1979.
- Kieffer, H. H., H₂O grain size and the amount of dust in Mars' residual north polar cap, *J. Geophys. Res.*, *95*, 1481–1494, 1990.
- Kieffer, H. H., and A. P. Zent, Quasi-periodic climatic change on Mars, in *Mars*, edited by H. H. Kieffer et al., pp. 1180–1218, Univ. of Ariz. Press, Tucson, 1992.
- Kieffer, H. H., J. S. C. Chase, E. Miner, G. Munch, and G. Neugebauer, Preliminary report on infrared radiometric measurements from Mariner 9 spacecraft, *J. Geophys. Res.*, *78*, 4291–4312, 1973.
- Kieffer, H. H., J. S. C. Chase, E. D. Miner, F. D. Palluconi, G. Munch, G. Neugebauer, and T. Z. Martin, Infrared thermal mapping of the Martian surface and atmosphere: First results, *Science*, *193*, 780–786, 1976.
- Kieffer, H. H., T. Z. Martin, A. R. Peterfreund, B. M. Jakosky, E. D. Miner, and F. D. Palluconi, Thermal and albedo mapping of Mars during the Viking primary mission, *J. Geophys. Res.*, *82*, 4249–4292, 1977.
- Kieffer, H. H., T. Titus, K. Mullins, and P. R. Christensen, Mars south polar cap as observed by the Mars Global Surveyor Thermal Emission Spectrometer, *J. Geophys. Res.*, *105*, 9653–9700, 2000.
- Lane, M. D., Infrared optical constants of calcite and their relationship to particle size effects in thermal emission spectra of granular calcite, *J. Geophys. Res.*, *104*, 14,099–14,108, 1999.
- Lane, M. D., and P. R. Christensen, Thermal infrared emission spectroscopy of anhydrous carbonates, *J. Geophys. Res.*, *102*, 25,581–25,592, 1997.
- Lazerev, A. N., *Vibrational Spectra and Structure of Silicates*, 302 pp., Consult. Bur., New York, 1972.
- Lucchitta, B. K., Lakes or playas in Valles Marineris, in *Reports of Planetary Geology Program, NASA Tech. Memo., TM-85127*, 233–234, 1982.
- Lyon, R. J. P., Evaluation of infrared spectroscopy for compositional analysis of lunar and planetary soils, in *Stanford Research Institute Final Report Under Contract NASr*, 139 pp., Stanford Res. Inst., Menlo Park, Calif., 1962.
- Maguire, W. C., Martian isotopic ratios and upper limits for possible minor constituents as derived from Mariner 9 infrared spectrometer data, *Icarus*, *32*, 85–97, 1977.
- Martin, T. Z., Thermal infrared opacity of the Mars atmosphere, *Icarus*, *66*, 2–21, 1986.
- Martin, T. Z., A. R. Peterfreund, E. D. Miner, H. H. Kieffer, and G. E. Hunt, Thermal infrared properties of the Martian atmosphere, 1, Global behavior at 7, 9, 11, and 20 μm , *J. Geophys. Res.*, *84*, 2830–2842, 1979.
- McCauley, J. F., Geologic map of the Coprates Quadrangle of Mars, *U.S. Geol. Surv. Misc. Invest. Ser., Map I-897*, scale 1:5,000,000, 1978.
- McCord, T. B., R. Clark, and R. L. Huguenin, Mars: Near-infrared reflectance and spectra of surface regions and compositional implications, *J. Geophys. Res.*, *87*, 3021–3032, 1978.
- McSween, H. Y., Jr., et al., Chemical, multispectral, and textural constraints on the composition and origin of rocks at the Mars Pathfinder landing site, *J. Geophys. Res.*, *104*, 8679–8716, 1999.
- Mellon, M. T., B. M. Jakosky, H. H. Kieffer, and P. R. Christensen, High resolution thermal inertia mapping from the Mars Global Surveyor Thermal Emission Spectrometer, *Icarus*, *148*, 437–455, 2000.
- Melosh, H. J., and A. M. Vickery, Impact erosion of the primordial atmosphere of Mars, *Nature*, *338*, 487–489, 1989.
- Moersch, J. E., and P. R. Christensen, Thermal emission from particulate surfaces: A comparison of scattering models with measured spectra, *J. Geophys. Res.*, *100*, 7465–7477, 1995.
- Morris, R. V., D. C. Golden, and J. F. Bell III, Low-temperature reflectivity spectra of red hematite and the color of Mars, *J. Geophys. Res.*, *102*, 9125–9133, 1997.
- Morris, R. V., et al., Mineralogy, composition, and alteration of Mars Pathfinder rocks and soils: Evidence from multispectral, elemental, and magnetic data on terrestrial analogue, SNC meteorite, and Pathfinder samples, *J. Geophys. Res.*, *105*, 1757–1817, 2000.
- Mukhin, L. M., A. P. Koscheev, Y. P. Dikov, J. Huth, and H. Wanke, Experimental simulations of the photodecomposition of carbonates and sulphates on Mars, *Nature*, *379*, 141–143, 1996.
- Mustard, J. F., and J. E. Hays, Effects of hyperfine particles on reflectance spectra from 0.3 to 25 μm , *Icarus*, *125*, 145–163, 1997.
- Mustard, J. F., and J. M. Sunshine, Seeing through the dust: Martian crustal heterogeneity and links to the SNC meteorites, *Science*, *267*, 1623–1626, 1995.
- Mustard, J. F., J.-P. Bibring, S. Erard, E. M. Fischer, J. W. Head, S. Hartz, Y. Langevin, C. M. Pieters, and C. J. Sotin, Interpretation of spectral units of Isidis-Syrtis Major from ISM-Phobos 2 observations, *Lunar Planet. Sci.*, *XXI*, 835–836, 1990.
- Mustard, J. F., S. Erard, J.-P. Bibring, J. W. Head, S. Hartz, Y. Langevin, C. M. Pieters, and C. J. Sotin, The surface of Syrtis Major: Composition of the volcanic substrate and mixing with altered dust and soil, *J. Geophys. Res.*, *98*, 3387–3400, 1993.
- Mustard, J. F., S. Murchie, S. Erard, and J. M. Sunshine, In situ compositions of Martian volcanics: Implications for the mantle, *J. Geophys. Res.*, *102*, 25,605–25,615, 1997.
- Nedell, S. S., S. W. Squyres, and D. W. Anderson, Origin and evolution of the layered deposits in the Valles Marineris, Mars, *Icarus*, *70*, 409–441, 1987.
- Neugebauer, G., G. Munch, H. Kieffer, J. S. C. Chase, and E. Miner, Mariner 1969 infrared radiometer results: Temperatures and thermal properties of the Martian surface, *Astron. J.*, *76*, 719–728, 1971.
- Paige, D. A., and A. P. Ingersoll, Annual heat balance of Martian polar caps: Viking observations, *Science*, *228*, 1160–1168, 1985.
- Palluconi, F. D., and H. H. Kieffer, Thermal inertia mapping of Mars from 60°S to 60°N, *Icarus*, *45*, 415–426, 1981.
- Pimentel, G. C., P. B. Forney, and K. C. Herr, Evidence about hydrate and solid water in the Martian surface from the 1969 Mariner infrared spectrometer, *J. Geophys. Res.*, *79*(11), 1623–1634, 1974.
- Planetary Data System, *Planetary Data System Standards, Version 3.2, Doc. JPL D-7669, Part 1*, Jet Propul. Lab., Pasadena, Calif., 1995a.
- Planetary Data System, *Planetary Data System Standards, Version 3.2, Doc. JPL D-7669, Part 2*, Jet Propul. Lab., Pasadena, Calif., 1995b.
- Pleskot, L. K., and E. D. Miner, Time variability of Martian bolometric albedo, *Icarus*, *45*, 179–201, 1981.
- Presley, M. A., and R. E. Arvidson, Nature and origin of materials exposed in the Oxia Palus-Western Arabia-Sinus Meridiani region, Mars, *Icarus*, *75*, 499–517, 1988.
- Presley, M. A., and P. R. Christensen, Thermal conductivity measurements of particulate materials, 2, Results, *J. Geophys. Res.*, *102*, 6651–6666, 1997.
- Ramsey, M. S., and P. R. Christensen, Mineral abundance determination: Quantitative deconvolution of thermal emission spectra, *J. Geophys. Res.*, *103*, 577–596, 1998.
- Ramsey, M. S., P. R. Christensen, N. Lancaster, and D. A. Howard, Identification of sand sources and transport pathways at Kelso Dunes, California using thermal infrared remote sensing, *Geol. Soc. Am. Bull.*, *111*, 636–662, 1999.
- Reider, R., T. Economou, H. Wanke, A. Turkevich, J. Crisp, J. Bruckner, G. Drebus, and J. H. Y. McSween, The chemical composition of Martian soil and rocks returned by the mobile alpha proton X-ray spectrometer: Preliminary results from the X-ray mode, *Science*, *278*, 1771–1774, 1997.
- Rice, R. F., Some practical universal noiseless coding techniques, *JPL Publ. 79-22*, Jet Propul. Lab., Pasadena, Calif., 1979.
- Ruff, S. W., and P. R. Christensen, Thermal-infrared spectral characteristics of Martian albedo features: Clues to composition, in *The Fifth International Conference on Mars [CD-ROM]*, *LPI Contrib. 972*, abstract 6230, Lunar and Planet. Inst., Houston, Tex., 1999.
- Ruff, S. W., P. R. Christensen, R. N. Clark, H. H. Kieffer, M. C. Malin, J. L. Bandfield, B. M. Jakosky, M. D. Lane, M. T. Mellon, and M. A.

- Presley, Mars' "White Rock" feature lacks evidence of an aqueous origin: Results from Mars Global Surveyor, *J. Geophys. Res.*, this issue.
- Salisbury, J. W., Mid-infrared spectroscopy: Laboratory data, in *Remote Geochemical Analysis: Elemental and Mineralogical Composition*, edited by C. Pieters and P. Englert, chap. 4, pp. 79–82, Cambridge Univ. Press, New York, 1993.
- Salisbury, J. W., and J. W. Eastes, The effect of particle size and porosity on spectral contrast in the mid-infrared, *Icarus*, *64*, 586–588, 1985.
- Salisbury, J. W., and A. Wald, The role of volume scattering in reducing spectral contrast of reststrahlen bands in spectra of powdered minerals, *Icarus*, *96*, 121–128, 1992.
- Salisbury, J. W., L. S. Walter, and N. Vergo, Mid-infrared (2.1–25 μm) spectra of minerals: First edition, in *U.S. Geol. Surv. Open File Rep.*, 87–263, 1987.
- Salisbury, J. W., L. S. Walter, N. Vergo, and D. M. D'Aria, *Infrared (2.1–25 μm) Spectra of Minerals*, 267 pp., Johns Hopkins Univ. Press, Baltimore, Md., 1991.
- Singer, R. B., The dark materials on Mars, I, New information from reflectance spectroscopy on the extent and mode of oxidation, *Lunar Planet. Sci.*, *XI*, 1045–1047, 1980.
- Singer, R. B., Spectral evidence for the mineralogy of high-albedo soils and dust on Mars, *J. Geophys. Res.*, *87*, 10,159–10,168, 1982.
- Singer, R. B., T. B. McCord, R. N. Clark, J. B. Adams, and R. L. Huguenin, Mars surface composition from reflectance spectroscopy: A summary, *J. Geophys. Res.*, *84*, 8415–8426, 1979.
- Smith, M. D., J. L. Bandfield, and P. R. Christensen, Separation of atmospheric and surface spectral features in Mars Global Surveyor Thermal Emission Spectrometer (TES) spectra: Models and atmospheric properties, *J. Geophys. Res.*, *105*, 9589–9608, 2000a.
- Smith, M. D., B. J. Conrath, J. C. Pearl, and P. R. Christensen, Observations of dust opacity during aerobraking and science phasing, *J. Geophys. Res.*, *105*, 9539–9552, 2000b.
- Smith, M. D., J. C. Pearl, B. J. Conrath, and P. R. Christensen, Thermal Emission Spectrometer results: Atmospheric thermal structure and aerosol distribution, *J. Geophys. Res.*, this issue.
- Thomas, P., Martian intracrater splotches: Occurrence, morphology, and colors, *Icarus*, *57*, 205–227, 1984.
- Titus, T. N., H. H. Kieffer, K. F. Mullins, and P. R. Christensen, TES premapping data: A look at slab ice and snow flurries in the Martian north polar night, *J. Geophys. Res.*, in press, 2001.
- Toon, O. B., J. B. Pollack, and C. Sagan, Physical properties of the particles comprising the Martian dust storm of 1971–1972, *Icarus*, *30*, 663–696, 1977.
- Walter, L. S., and J. W. Salisbury, Spectral characterization of igneous rocks in the 8–12 μm region, *J. Geophys. Res.*, *94*(B7), 9203–9213, 1989.
- Warren, S. G., Optical constants of ice from the ultraviolet to the microwave, *Appl. Opt.*, *23*, 1206–1225, 1984.
- Wilson, E. B., Jr., J. C. Decius, and P. C. Cross, *Molecular Vibrations: The Theory of Infrared and Raman Vibrational Spectra*, McGraw-Hill, New York, 1955.
- Zimbelman, J. R., and H. H. Kieffer, Thermal mapping of the northern equatorial and temperate latitudes of Mars, *J. Geophys. Res.*, *84*, 8239–8251, 1979.
-
- J. L. Bandfield, K. Bender, P. R. Christensen, N. Gorelick, V. E. Hamilton, G. L. Mehall, K. Murray, and S. W. Ruff, Department of Geology, Arizona State University, Campus Box 871404, Tempe, AZ 85287-1404. (phil.christensen@asu.edu)
- R. L. Clark, U.S. Geological Survey, Denver, CO.
- B. J. Conrath, S. Dason, E. Greene, J. C. Pearl, and M. D. Smith, Goddard Space Flight Center, Mail Code 693, Greenbelt, MD 20771.
- R. T. Clancy, Space Science Institute, Boulder, CO.
- M. Greenfield and S. Silverman, Raytheon Santa Barbara Remote Sensing, Goleta, CA.
- B. M. Jakosky and M. T. Mellon, Laboratory for Atmospheric and Space Physics, University of Colorado, Boulder, CO 80309-0392.
- H. H. Kieffer and T. N. Titus, U.S. Geological Survey, Flagstaff, AZ 86001.
- R. O. Kuzmin, Vernadsky Institute, Moscow, Russia.
- M. D. Lane and R. V. Morris, NASA Johnson Space Center, Houston, TX 77058.
- M. C. Malin, Malin Space Science Systems, San Diego, CA 92191-0148.
- T. Roush, Ames Research Center, Moffett Field, CA 94035-1000.

(Received August 31, 2000; revised February 12, 2001; accepted February 19, 2001.)

